AN INVESTIGATION OF LASER SPECKLE

USING A LINEAR, CHARGE-COUPLED, PHOTODIODE ARRAY

A thesis presented in partial fulfilment of
the requirements for the degree of
Master of Science
in Physics at
Massey University

by

Craig David Eccles

1982

ABSTRACT

This thesis describes the use of a linear, charge-coupled, photodiode array, and microprocessor in the measurement of various laser speckle statistics.

Contrast and probability densities for fully and partially developed speckle patterns are derived theoretically as a function of scattering angle and surface roughness.

The experimental apparatus incorporating the photodiode array and microprocessor is described in detail, along with various experiments to check expected specifications. Using this apparatus, measurements are made of the probability density and contrast, as a function of scattering angle, for the speckle patterns produced by three different surfaces. From these results and the theoretical predictions the roughness parameters for these surfaces are determined.

In-plane surface displacement is measured using a cross-correlation technique and is found to produce accurate results over a wide range of displacements (from 1μm to 0.5mm).

A short section on speckle size is also included to verify theoretical predictions made in an earlier chapter.

ACKNOWLEDGEMENTS

I would like to acknowledge the advice and assistance provided by my project supervisor Dr Geoffrey Barnes, and the staff of the Physics Department.

My thanks also to Massey University for providing the opportunity and facilities for carrying out this project, and to Mrs Joan Mathews for the typing and copying of this manuscript.

TABLE OF CONTENTS

LIST OF FIGURES

LIST OF TABLES

Symbol	Meaning	Page where first mentioned
r	Surface roughness	2
w	Waviness	2
σ	Standard deviation of subscript	3
$<>$	Mean value of symbol within brackets ...	3
T	Correlation length	3
ϕ_i	Phase of ith elementary phasor	7
θ	Angle of incidence	7
ω	Angle of scatter	7
A_i	The ith elementary phasor	7
A	The resultant amplitude phasor	7
ψ	The resultant phase	7
λ	Wavelength of light source	8
$p()$	Probability density of symbol(s) within brackets	8
C	Speckle contrast	9
I	Speckle intensity (also relative intensity)	9
x,y	Real and imaginary components of the resultant amplitude phasor	10
n	The number of scattering centres	13
a	Amplitude of generalised phasor A_i	13
ξ	Smallest distance on a surface which produces a resolvable image in the speckle pattern ..	17
n'	Refractive index of air	17
d	Diameter of illuminated area on a surface	17
A_x, A_y	Amplitudes of the orthogonal components of partially polarized light	25
I_x, I_y	Intensities of the orthogonal components of partially polarized light	25
β	Angle between the net polarization vector ($\underset{\sim}{A}_T$) and $\underset{\sim}{A}_x$	27
α	Semi-angular subtense of the object at the speckle being observed	33
δ	Characteristic speckle size	33

L	Distance from the object to the speckle being observed	34
X,Y,Z,Q	Computer stack registers	77
M()	Signifies contents of memory locations within brackets	77
Mx	Particular memory space on computer (see Appendix B)	82
c	Compensated video data	84
f(I)	Frequency of occurrence for a particular intensity I	98
Δx	Speckle displacement	127
D	Object displacement	130
b	Light source to object distance	130
M	Micrometer displacement	130
r_c	A constant amplitude vector added to the random walk resultant amplitude	158

1 Introduction

When direct sunlight is observed after having been scattered from a slightly roughened surface, small multi-coloured points of light, which appear to scintillate as the head or the surface is moved, will be seen. This phenomenon is an example of a speckle pattern caused by the scattered light forming a complex interference pattern in the space in front of the object.

Most sources of light do not product an obvious speckle pattern due to their lack of temporal and spatial coherence. An incandescent lamp for example produces a speckle pattern which changes continuously with time, at such a rate that the eye perceives only a uniform illumination. The coherence of sunlight however, is sufficient to form speckles when scattered from very smooth surfaces having a roughness of similar order to the coherence length.

Before going any further it would be a good idea to clarify exactly what is meant by a rough surface, and to define a number of terms which will be used throughout the text. With reference to figure 1.1 it can be seen that for a two dimensional cross-section of a rough surface there are two components of surface texture.

(i) Roughness (or primary texture). These are the irregularities in the surface texture which result from the inherent action of the production process. (e.g. lapping, grinding, honing etc.)

(ii) Waviness (or secondary texture). The component of surface texture upon which the roughness is superimposed. Waviness may result from such factors as gross surface shape, (the object could be a cylinder for example), or from unintentional errors produced by faulty or imperfect manufacturing techniques.

Figure 1.1 Cross-section of a rough surface

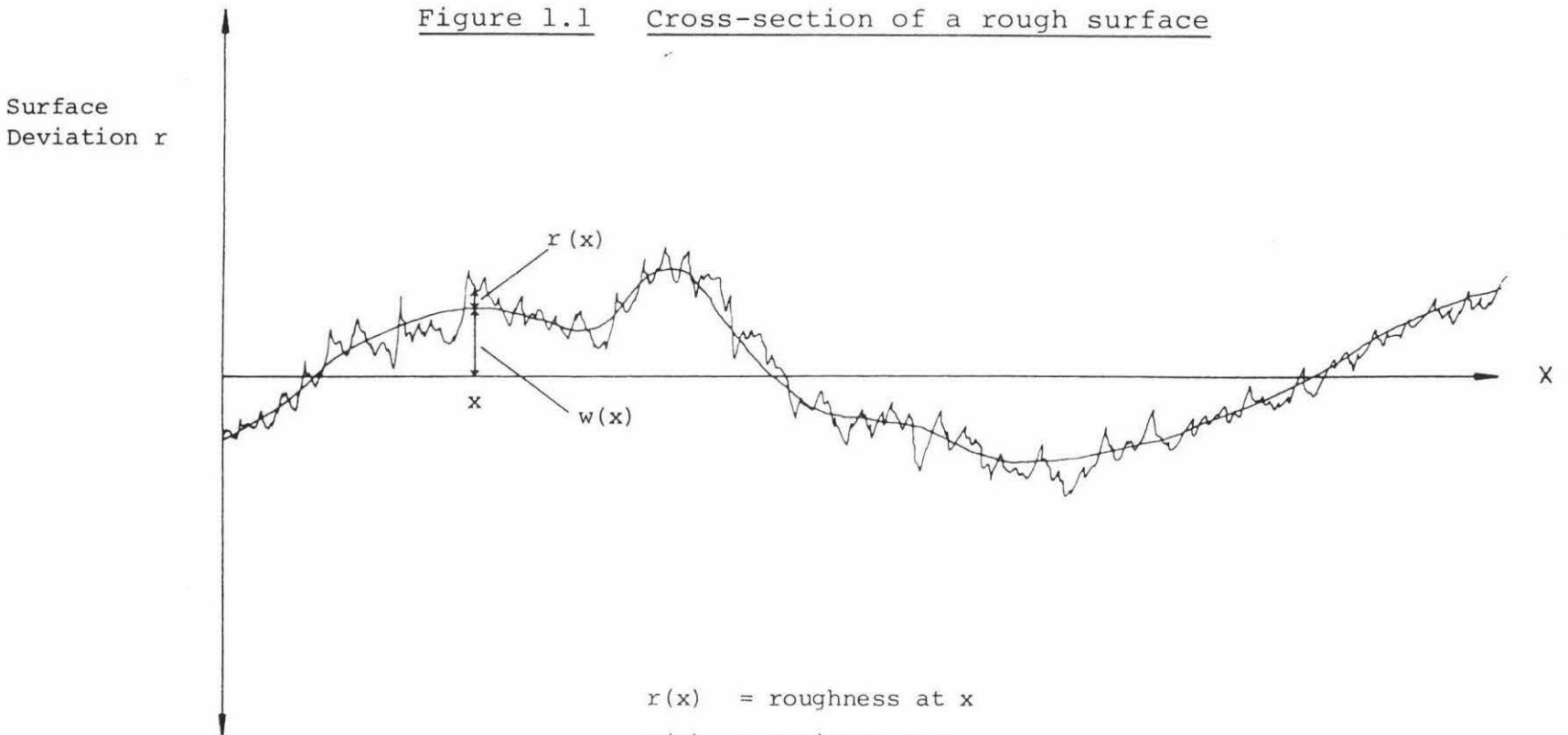

r(x) = roughness at x

w(x) = waviness at x

Roughness and waviness may both be statistically defined in terms of their root mean square values. Because we can arbitrarily set their mean values to zero we have, using the relationship

$$\sigma_r^2 = \langle r^2 \rangle - \langle r \rangle^2, \tag{1.1}$$

that

$$\sigma_r^2 = \langle r^2 \rangle, \tag{1.2}$$

where $\langle r \rangle$ is the mean value, $\langle r^2 \rangle$ the mean square value, and σ_r^2 the variance of surface roughness. The root mean square value of roughness is therefore simply equal to its standard deviation. In a similar manner we can also define waviness in terms of its standard deviation σ_w.

For most of this thesis it will be assumed for simplicity that $\sigma_w << \sigma_r$ although, for many real objects, this may not be the case.

In addition to these parameters we can also define a pseudo wavelength for such a surface in terms of its autocorrelation function. In the absence of any large scale waviness the autocorrelation function for a rough surface with a Gaussian probability density (a reasonable assumption for most randomly produced surfaces) will also be Gaussian in form, dropping from a maximum value at lag zero at a rate dependent on the adjacent peak-to-peak distance. We can numerically specify this rate by defining the correlation length T as the distance one must travel on the surface before the correlation coefficient has dropped by a factor of e^{-2}. The physical significance of this parameter can be seen more clearly in figures 1.2 and 1.3 which show two rough surfaces with the same surface roughness but quite different values of T.

Having defined the various aspects of a rough surface we will now move on to consider speckle patterns produced

Figure 1.2 Rough surface with small value of T

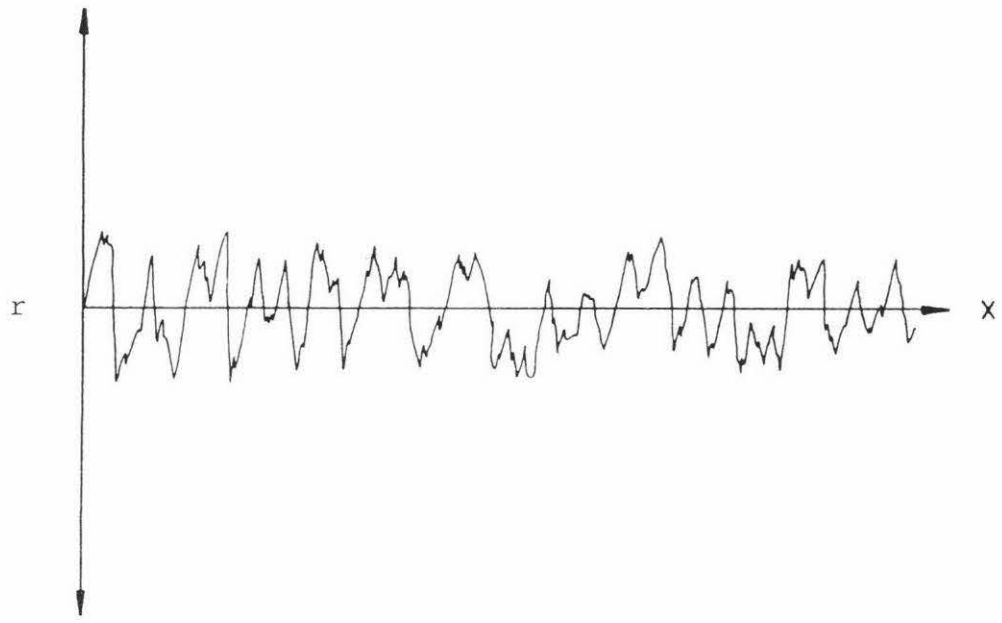

Figure 1.3 Rough surface with large value of T

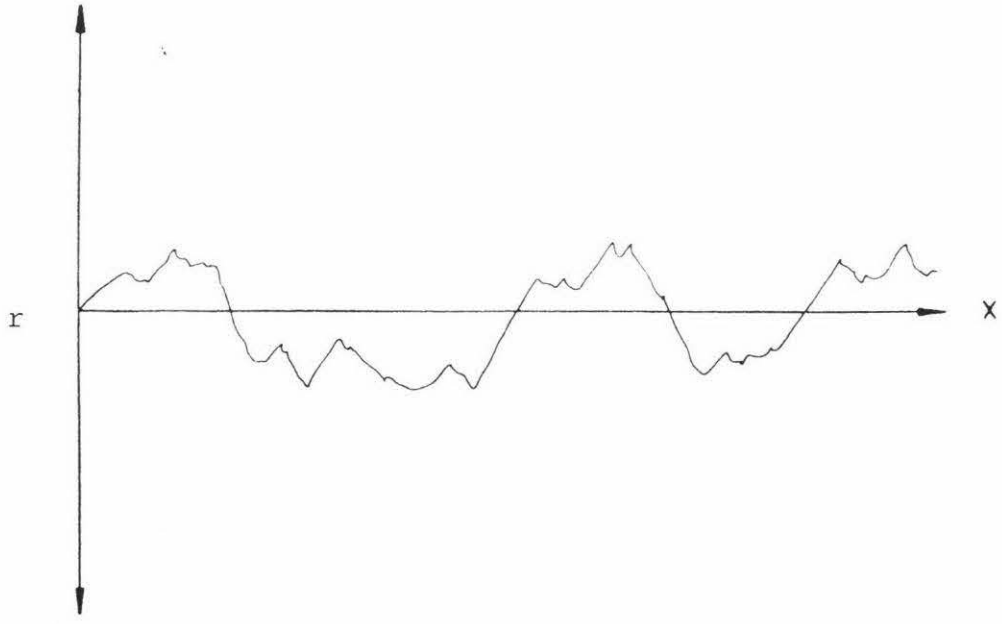

using laser light. Because of its far greater temporal and spatial coherence the laser is an ideal light source with which to produce speckle. Practically any stationary object will produce a readily visible pattern, although surfaces such as milk or human skin will, because of their continuous movement (Brownian motion in the case of milk), tend to blur the speckles.

Surfaces with a roughness much less than the wavelength of light tend to produce a speckle pattern having reduced contrast and this fact will be used in this thesis to obtain a numerical estimate of σ_r, for various surfaces.

Another phenomenon which is immediately obvious when observing speckle is that for small displacements of an object (up to about a millimetre) the speckle pattern suffers little change other than a shift in the direction of the object's displacement. By measuring this shift, a non-contact means of measuring surface displacement can thus be obtained.

Most conventional work done with speckle has used photographic techniques which are often slow, or video processing which is usually complex and expensive. This thesis will present a new approach to the measurement of surface roughness and displacement by the statistical analysis of the speckle pattern as detected by a linear, charge-coupled, photodiode array.

While suffering from a number of statistical short comings (chiefly the limited number of sample points available) the array is quite sensitive and does allow rapid acquisition of data. In conjunction with a microprocessor and low powered laser it provides a reasonably compact system which, when perfected, could conceivably find its way into an industrial application.

2 Statistical Properties of Laser Speckle Patterns

The amplitude of the light at any point in a speckle pattern is determined by the coherent superposition of all field vectors scattered from the surface which converge on that point. The surface may be considered to consist of a large number of independent scattering centres displaced about the mean level of the surface in a random fashion. These scattering centres are regions over which the surface deviation is considerably less than one wavelength of the illuminating light. They may therefore be considered to be regions which scatter light of constant phase. Numerically, the area of the scattering centre is of the order of T^2 where T is the correlation length as previously defined. Due to the variable path differences introduced by the surface, and the position of the observation point, the field amplitudes at any point in space due to each of the scattering centres, will, in general, be random in both phase and amplitude. With reference to figure 2.1 it can be seen that such a sum of random phasors is identical to the random or 'drunkards' walk problem encountered in many fields of physics. The techniques already developed in the solution of these problems can thus be applied to speckle.

2.1 Probability Density of Phase Difference

Information about surface roughness and the nature of the illuminating light source may be gained by studying the probability density of the speckle intensity. To derive a general expression for this function requires knowledge of a number of statistical parameters, including the probability density of the phase difference ϕ as defined in figure 2.1.

Figure 2.2 depicts a generalised scattering situation for a

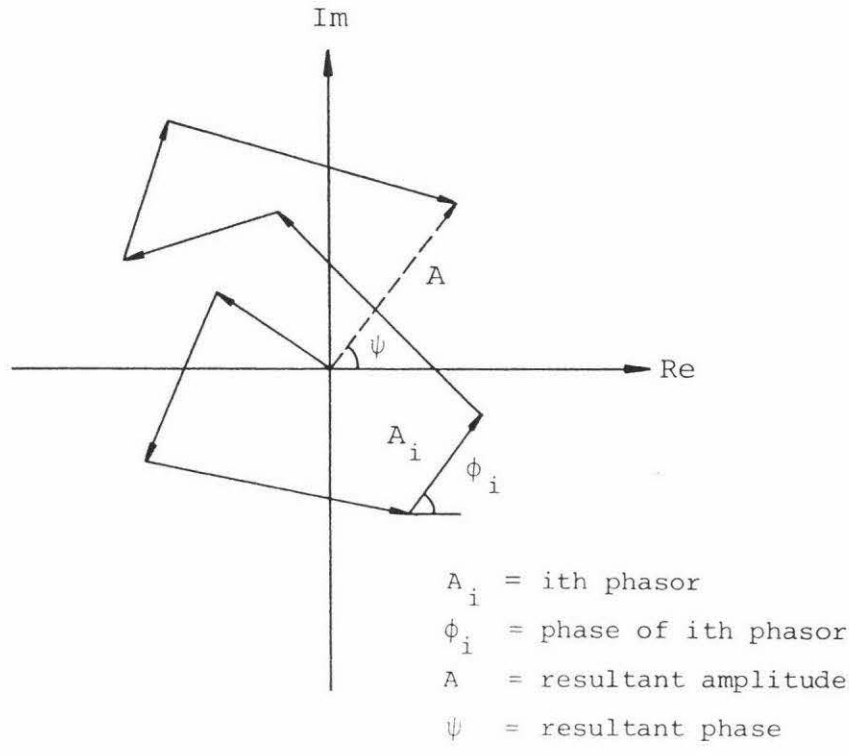

Figure 2.1 Random walk in the complex plane

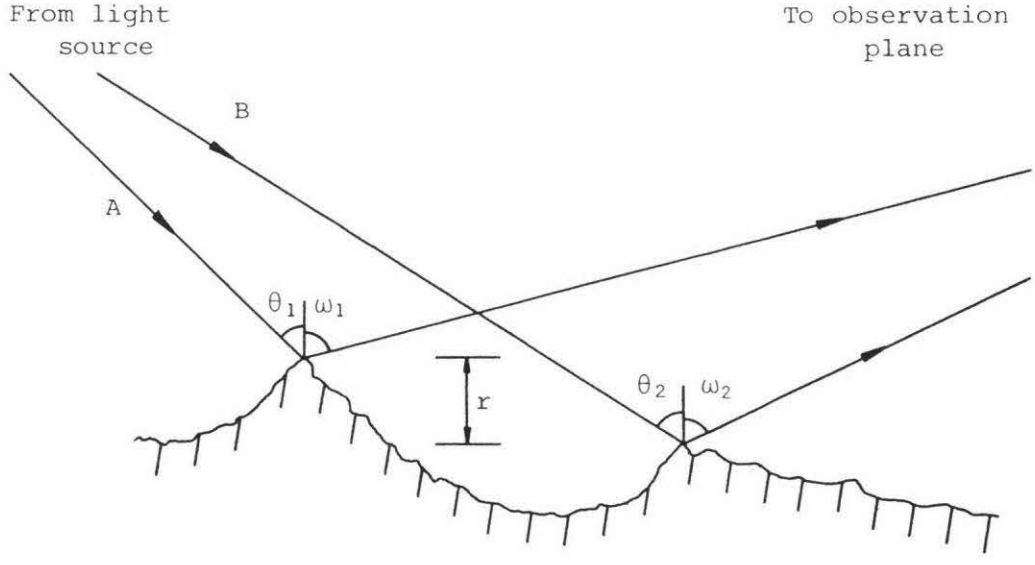

Figure 2.2 Light scatter from a rough surface

rough surface. Light travelling path B is taken as the reference beam with no phase shift. All other rays (represented by path A) will suffer a phase shift ϕ_i where the subscript i indicates the light has been scattered by the ith scattering centre. For distant source and observation points this will take the value (see appendix F for derivation)

$$\phi_i = \frac{2\pi r}{\lambda}(\cos\theta+\cos\omega). \tag{2.1}$$

If we assume, as previously mentioned, that the surface roughness r follows a Gaussian distribution we will have

$$p(r) = \frac{1}{\sigma_r\sqrt{2\pi}} \exp\left(\frac{-r^2}{2\sigma_r^2}\right). \tag{2.2}$$

If we take the mean square value of equation 2.1 and then apply the relationship found in equation 1.2, we can substitute for σ_r in equation 2.2 with the expression

$$\sigma_r = \frac{\lambda\sigma_\phi}{2\pi(\cos\theta+\cos\omega)}, \tag{2.3}$$

where σ_ϕ is the standard deviation of phase difference at the point of observation. Since phase difference is directly proportional to roughness for a constant incidence angle θ the probability density for phase difference will also be Gaussian. By substituting equation 2.3 into 2.2 and normalising we obtain

$$p(\phi) = \frac{1}{\sigma_\phi\sqrt{2\pi}} \exp\left(\frac{-\phi^2}{2\sigma_\phi^2}\right). \tag{2.4}$$

For values of phase difference greater than π total destructive interference can take place producing regions of complete darkness in the speckle pattern. Such a pattern is termed 'fully developed' and the surface which produces it as optically rough. On the other hand, surfaces which

produce phase shifts considerably less than π will reflect light specularly and are considered optically smooth. If σ_ϕ is taken as a representative value of phase difference for the whole speckle pattern we see from equation 2.3 that for zero angles of incidence and scatter, and a Helium-Neon light source, that surfaces rougher than $\simeq 0.2\mu m$ may be considered optically rough. For angles greater than zero this value will rise until, at glancing angles (i.e. $\theta \simeq \omega \rightarrow 90$), all surfaces will reflect light specularly. Thus even the rough surface of a road can act as a specular reflector if the sun and observer lie near a line tangential to the road surface.

This ability to adjust the visual roughness of an object by changing its angle to the illuminating beam, and the effect this has on the speckle pattern, allows estimates to be made of surface roughness parameters for a wide range of objects.

2.2 Speckle Contrast

The loss of speckle visibility which occurs as σ_ϕ decreases can be expressed in terms of speckle contrast which is defined by the ratio

$$C = \frac{\sigma_I}{\langle I \rangle}, \qquad (2.5)$$

where σ_I and $\langle I \rangle$ are the standard deviation and mean values of speckle intensity.

Contrast is not difficult to obtain experimentally, but to be of any practical use its relationship to the surface parameters roughness and coherence length must be determined.

The following rather lengthy derivation of speckle contrast, is modelled after the work of Beckmann {ref 2.1} and Goodman {ref 2.2}. Where pertinent, detailed references to their works are given.

Consider again the random walk situation pictured in figure 2.1. From this diagram we see that the resultant light intensity at the point considered is

$$I = |A|^2 = |x^2+y^2| = x^2+y^2 = (A\cos\psi)^2+(A\sin\psi)^2, \quad (2.6)$$

where x and y are the real and imaginary components of A, the resultant amplitude phasor.

From this expression the mean light intensity over the whole speckle pattern can be found, since as x and y are independent (see below), we have

$$\langle I\rangle = \langle x^2+y^2\rangle = \langle x^2\rangle+\langle y^2\rangle. \quad (2.7)$$

The variances of x and y are defined by the expressions

$$\sigma_x^2 = \langle x^2\rangle-\langle x\rangle^2 \text{ and } \sigma_y^2 = \langle y^2\rangle-\langle y\rangle^2, \quad (2.8)$$

so 2.7 becomes

$$\langle I\rangle = \sigma_x^2+\langle x\rangle^2+\sigma_y^2+\langle y\rangle^2. \quad (2.9)$$

Using (2.8) we can determine σ_I since for similar reasons

$$\sigma_I^2 = \langle I^2\rangle-\langle I\rangle^2. \quad (2.10)$$

We already know $\langle I\rangle$ from equation (2.9) but $\langle I^2\rangle$ is somewhat more complicated and may be expanded as follows

$$\langle I^2\rangle = \langle |A|^4\rangle = \langle (x^2+y^2)^2\rangle$$

$$= \langle x^4\rangle+2\langle x^2y^2\rangle+\langle y^4\rangle. \quad (2.11)$$

To express this result in terms of the more easily obtained parameters used in equation 2.9 requires knowledge of the probability distributions of x and y over the whole speckle pattern. Since the number of scattering centres contributing to the intensity at any point will be very large and

because we have assumed that each scattering centre is essentially independent from its neighbours we can therefore infer that x and y will satisfy the central limit theorem and thus be normally distributed {ref 2.1 p 191}. Hence we have the expressions

$$p(x) = \frac{1}{\sigma_x\sqrt{2\pi}} \exp\left(-\frac{(x-\langle x\rangle)^2}{2\sigma_x^2}\right),$$

and

$$p(y) = \frac{1}{\sigma_y\sqrt{2\pi}} \exp\left(-\frac{(y-\langle y\rangle)^2}{2\sigma_y^2}\right). \qquad (2.12)$$

And because

$$\langle x^4\rangle = \int_{-\infty}^{\infty} p(x)\,x^4\,dx, \qquad (2.13)$$

we have

$$\langle x^4\rangle = \frac{1}{\sigma_x\sqrt{2\pi}} \int_{-\infty}^{\infty} \exp\left(-\frac{(x-\langle x\rangle)^2}{2\sigma_x^2}\right) x^4\,dx, \qquad (2.14)$$

which after some rearrangement becomes

$$\langle x^4\rangle = \frac{\exp(-q^2/p)}{\sigma_x\sqrt{2\pi}} \int_{-\infty}^{\infty} \exp(2qx-px^2)\,x^4\,dx, \qquad (2.15)$$

where $p = \frac{1}{2\sigma_x^2}$ and $q = \frac{\langle x\rangle}{2\sigma_x^2}$.

This is a standard integral {ref 2.3 p 337} with the following solution

$$\langle x^4\rangle = \frac{\exp(-q^2/p)}{\sigma_x\sqrt{2\pi}} \cdot \left(\frac{\sigma_x^2}{4}\right) \cdot \left(\frac{\pi}{p}\right)^{\frac{1}{2}} \cdot \frac{d^3}{dq^3}\left(q \cdot \exp\left(\frac{q^2}{p}\right)\right). \qquad (2.16)$$

After carrying out the differentiation and substituting for p and q we obtain

$$\langle x^4 \rangle = 3\sigma_x^4 + 6\langle x \rangle^2 \sigma_x^2 + \langle x \rangle^4 , \tag{2.17}$$

and similarly

$$\langle y^4 \rangle = 3\sigma_y^4 + 6\langle y \rangle^2 \sigma_y^2 + \langle y \rangle^4 . \tag{2.18}$$

To solve $\langle x^2 y^2 \rangle$ we first note that the correlation coefficient

$$C(x,y) = \frac{\langle xy \rangle - \langle x \rangle \langle y \rangle}{\sigma_x \sigma_y} = 0 , \tag{2.19}$$

since by using the information in equation 2.6 we see that

$$\langle xy \rangle = \langle A^2 \cos\psi \sin\psi \rangle = 0 , \tag{2.20}$$

for a symmetrical distribution of ψ, and that rotation of the mean amplitude phasor in the complex plane allows us to set $\langle y \rangle = 0$ without affecting any observable parameters.

Since x and y are uncorrelated (and independent since both are Gaussian variables) we have from statistical theory {ref 2.1 p 188} that

$$\langle x^2 y^2 \rangle = \int_{-\infty}^{\infty} p(x,y) x^2 y^2 dx dy = \int_{-\infty}^{\infty} p(x) x^2 dx \int_{-\infty}^{\infty} p(y) y^2 dy , \tag{2.21}$$

which from equation 2.8 is simply

$$\begin{aligned} \langle x^2 y^2 \rangle &= (\sigma_x^2 + \langle x \rangle^2)(\sigma_y^2 + \langle y \rangle^2) \\ &= \sigma_x^2 \sigma_y^2 + \langle x \rangle^2 \sigma_y^2 , \end{aligned} \tag{2.22}$$

since $\langle y \rangle = 0$.

Using the results obtained in equations 2.5 and 2.10 we obtain the following expression for contrast

$$C = \frac{\sigma_I}{\langle I \rangle} = \frac{(\langle I^2 \rangle - \langle I \rangle^2)^{\frac{1}{2}}}{\langle I \rangle}. \qquad (2.23)$$

By substituting for $\langle I \rangle$ and $\langle I^2 \rangle$ using equations 2.9 and 2.11 and for $\langle x^4 \rangle$, $\langle y^4 \rangle$ and $\langle x^2 y^2 \rangle$ using equations 2.17, 2.18 and 2.22 this equation then becomes †

$$C = \frac{(2(\sigma_x^4 + \sigma_y^4) + 4\langle x \rangle^2 \sigma_x^2)^{\frac{1}{2}}}{\sigma_x^2 + \sigma_y^2 + \langle x \rangle^2}. \qquad (2.24)$$

Identical to the result obtained by Goodman {ref 2.2 p.72}.

Now we need to determine a relationship between the various parameters in this equation and the surface roughness of the object responsible for the speckle pattern. From figure 2.1 we saw that

$$A = \sum_i (A_i \exp(j\phi_i)) = \sum_i (A_i \cos\phi_i + jA_i \sin\phi_i), \qquad (2.25)$$

where the summation ranges over all n scattering centres contributing to the resultant amplitude.
Comparison of equations 2.6 and 2.25 shows that

$$x = \sum_i x_i = \sum_i A_i \cos\phi_i \quad \text{and} \quad y = \sum_i y_i = \sum_i A_i \sin\phi_i, \qquad (2.26)$$

where x_i and y_i are the real and imaginary components of phasor A_i.

For the moment it will be assumed that all scattering centres scatter equal amounts of light. This means that A_i will become a constant which shall be designated 'a'. The mean value of x is thus

$$\langle x \rangle = \langle \sum_i x_i \rangle = \sum_i \langle x_i \rangle = \sum_i \langle a \cos\phi_i \rangle$$

† For an alternative derivation of this equation see appendix G.

$$= a\sum_i \langle\cos\phi_i\rangle, \tag{2.27}$$

since all scattering centres are assumed independent. $\langle\cos\phi_i\rangle$ is the ensemble average of $\cos\phi_i$ over the whole speckle pattern for a particular value of i. That is

$$\langle\cos\phi_i\rangle = \int_{-\infty}^{\infty} p(\phi_i)\cos\phi_i \, d\phi_i. \tag{2.28}$$

For the case where all $p(\phi_i)$ are equal, (a reasonable assumption if the number of sampling points is large) (2.27) becomes

$$\begin{aligned}\langle x\rangle &= a\sum_i \int_{-\infty}^{\infty} p(\phi_i)\cos\phi_i \, d\phi_i \\ &= a\sum_i \int_{-\infty}^{\infty} p(\phi)\cos\phi_i \, d\phi_i \\ &= na \int_{-\infty}^{\infty} p(\phi)\cos\phi \, d\phi.\end{aligned} \tag{2.29}$$

Repeating the above process for $\langle y\rangle$ gives

$$\langle y\rangle = na \int_{-\infty}^{\infty} p(\phi)\sin\phi \, d\phi. \tag{2.30}$$

From equation 2.8 we saw that

$$\sigma_x^2 = \langle x^2\rangle - \langle x\rangle^2.$$

After substituting for x in terms of x_i this becomes

$$\sigma_x^2 = \langle(\Sigma_i x_i)^2\rangle - \langle\Sigma_i x_i\rangle^2. \tag{2.32}$$

But since we have assumed that all scattering centres are independent, this simplifies to give

$$\begin{aligned}\sigma_x^2 &= \sum_i \langle x_i^2\rangle - \sum_i \langle x_i\rangle^2 \\ &= \sum_i \langle a^2\cos^2\phi_i\rangle - \sum_i \langle a\cos\phi_i\rangle^2\end{aligned}$$

$$= a^2 \sum_{i} \int_{-\infty}^{\infty} p(\phi_i)\cos^2\phi_i d\phi_i - a^2 \sum_{i} \left(\int_{-\infty}^{\infty} p(\phi_i)\cos\phi_i d\phi_i \right)^2 . \qquad (2.33)$$

If all $p(\phi_i)$ are the same, as previously assumed, (2.33) becomes

$$\sigma_x^2 = a^2 n \int_{-\infty}^{\infty} p(\phi)\cos^2\phi d\phi - a^2 n \left(\int_{-\infty}^{\infty} p(\phi)\cos\phi d\phi \right)^2 . \qquad (2.34)$$

Now

$$\int_{-\infty}^{\infty} p(\phi)\cos\phi d\phi = \frac{1}{\sqrt{2\pi}\sigma_\phi} \int_{-\infty}^{\infty} \exp\left(\frac{-\phi^2}{2\sigma_\phi^2}\right)\cos\phi d\phi = \exp(-\tfrac{1}{2}\sigma_\phi^2), \qquad (2.35)$$

and

$$\int_{-\infty}^{\infty} p(\phi)\cos^2\phi d\phi = \frac{1}{\sqrt{2\pi}\sigma_\phi} \int_{-\infty}^{\infty} \exp\left(\frac{-\phi^2}{2\sigma_\phi^2}\right)\cos^2\phi d\phi$$

$$= \tfrac{1}{2}(1+\exp(-2\sigma_\phi^2)), \qquad (2.36)$$

using equation 2.4 and Gradshteyn's table of standard integrals {ref 2.3 p 480}. With these results equation 2.34 simplifies to give

$$\sigma_x^2 = \tfrac{1}{2}a^2 n(1+\exp(-2\sigma_\phi^2)) - a^2 n\exp(-\sigma_\phi^2), \qquad (2.37)$$

which is equivalent to

$$\sigma_x^2 = \tfrac{1}{2}a^2 n(1-\exp(-\sigma_\phi^2))^2 . \qquad (2.38)$$

Using the result from (2.35) and substituting into equation 2.29 we obtain

$$\langle x \rangle = na\exp(-\tfrac{1}{2}\sigma_\phi^2) . \qquad (2.39)$$

In a similar manner we find for σ_y that

$$\sigma_y^2 = a^2 n \int_{-\infty}^{\infty} p(\phi)\sin^2\phi d\phi - a^2 n \left(\int_{-\infty}^{\infty} p(\phi)\sin\phi d\phi \right)^2 . \qquad (2.40)$$

Now

$$\int_{-\infty}^{\infty} p(\phi)\sin\phi d\phi = \frac{1}{\sqrt{2\pi}\sigma_\phi}\int_{-\infty}^{\infty}\exp\left(\frac{-\phi^2}{2\sigma_\phi^2}\right)\sin\phi d\phi = 0, \qquad (2.41)$$

since we are integrating over an odd function, and

$$\int_{-\infty}^{\infty} p(\phi)\sin^2\phi d\phi = \frac{1}{\sqrt{2\pi}\sigma_\phi}\int_{-\infty}^{\infty}\exp\left(\frac{-\phi^2}{2\sigma_\phi^2}\right)\sin^2\phi d\phi$$

$$= \tfrac{1}{2}(1-\exp(-2\sigma_\phi^2)), \qquad (2.42)$$

see Gradshteyn {ref 2.3 p 480}. Equation 2.40 then becomes

$$\sigma_y^2 = \tfrac{1}{2}na^2(1-\exp(-2\sigma_\phi^2)), \qquad (2.43)$$

and $\langle y \rangle$ (from equations 2.30 and 2.41) is zero, as expected.

As indicated by Beckmann {ref 2.1 p 128} these results will also be correct if 'a' is replaced by $\langle A_i \rangle$ when the values of A_i can no longer be assumed equal.

On substituting equations 2.38, 2.39 & 2.43 into (2.24) we obtain

$$C = \frac{\sqrt{2}(\tfrac{1}{4}a^4n^2((1-B)^4+(1-B^2)^2)+n^3a^4B(1-B)^2)^{\frac{1}{2}}}{\tfrac{1}{2}na^2((1-B)^2+(1-B^2)+2nB)}, \qquad (2.44)$$

where $B = \exp(-\sigma_\phi^2)$ and $\sigma_\phi = \frac{4\pi}{\lambda}\sigma_r\cos\theta$ (see equation F.3).

This may be simplified to give

$$C = \frac{\sqrt{2}((1-B)^4+(1-B^2)^2+4nB(1-B)^2)^{\frac{1}{2}}}{(1-B)^2+(1-B^2)+2nB}. \qquad (2.45)$$

Contrast therefore depends on only three factors: the standard deviation of surface roughness, σ_r, the angle of incidence θ, and the number of scattering centres n.

While θ can be easily measured, n depends on a number of factors including the surface correlation length T. For speckle patterns produced in the image plane of a lens (as depicted in figure 2.3) the area on the surface contributing to the intensity at a point in the image plane is determined by the diffraction limiting effect of the lens. The smallest distance on the object which produces a resolvable image is given by the well know formula

$$\xi = \frac{1.22\lambda}{2n'\sin\gamma}, \tag{2.46}$$

where γ is half the angle subtended by the lens at the surface, and n' the refractive index of air. If T is taken as the diameter of the scattering centre, n may be defined by

$$n = \xi^2/T^2, \tag{2.47}$$

which after substituting for ξ, becomes

$$n = \frac{0.37\lambda^2}{T^2 n'^2 \sin^2\gamma}. \tag{2.48}$$

For the more general situation depicted in figure 2.4, where the lens is defocussed, n becomes

$$n = d^2/T^2, \tag{2.49}$$

where d is the diameter of the illuminated area contributing to the intensity at the detector. This formula also applies to the lensless situation in figure 2.5 (the pattern produced with this arrangement is termed objective speckle).

With n defined we can now consider what happens to speckle contrast for various surface conditions. Figures 2.6 and 2.7 plot contrast as a function of θ for various values of σ_r and n. From figure 2.6 we see that (as expected) contrast is reduced for decreasing surface roughness with a

Figure 2.3 Speckle formed in the image plane of a lens ('subjective' speckle)

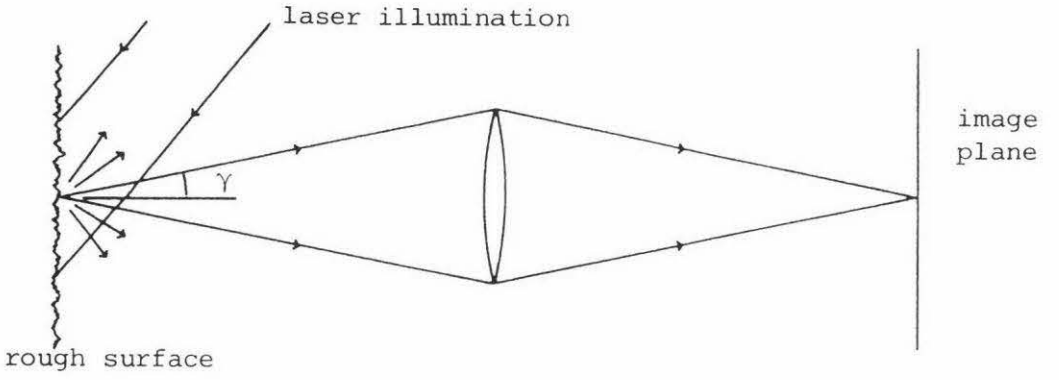

Figure 2.4 Speckle formed in the defocus plane of a lens

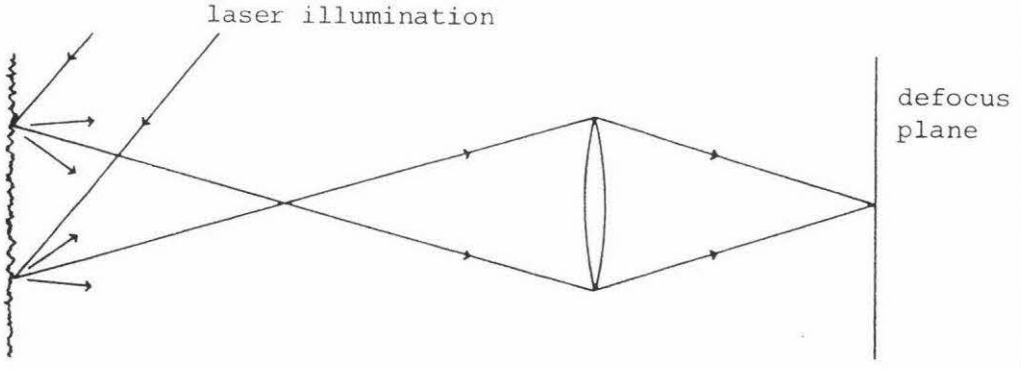

Figure 2.5 Speckle formed without a lens ('objective' speckle)

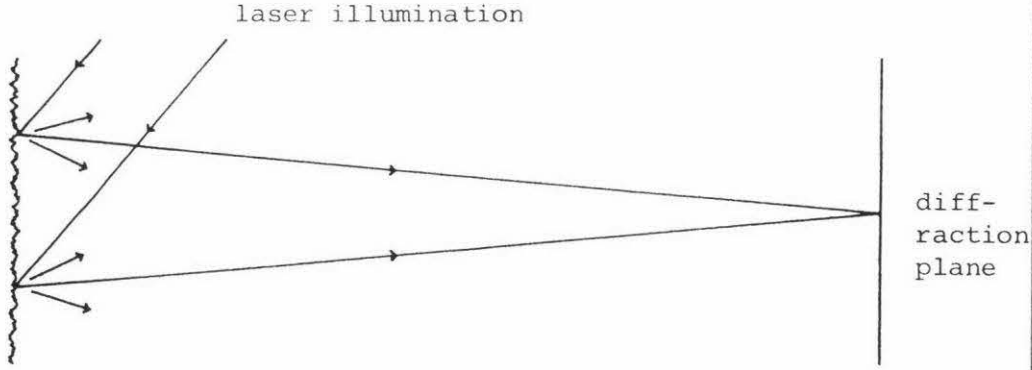

Figure 2.6 Contrast as a function of σ_r and θ for constant n

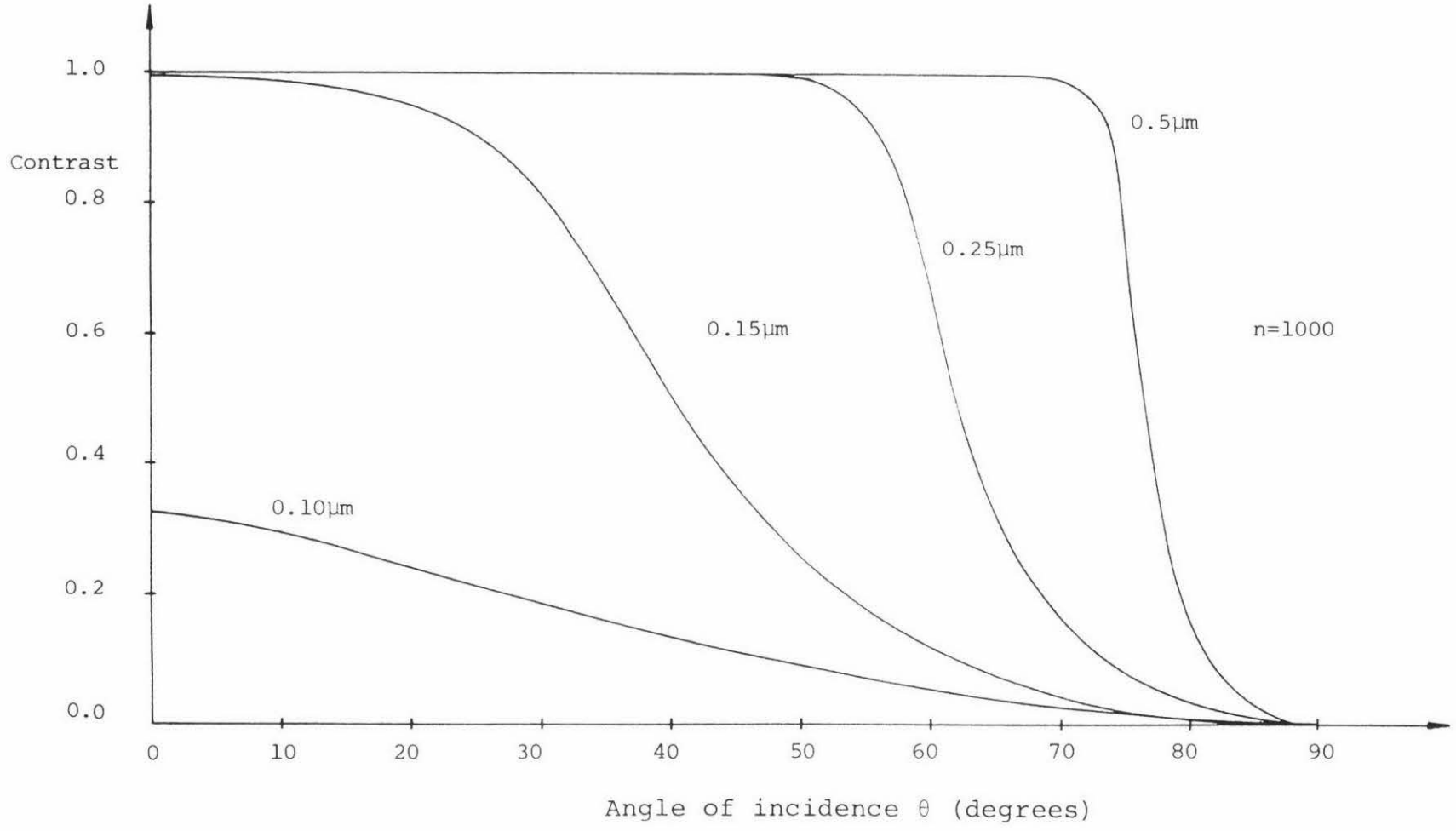

particularly large drop for $\sigma_r \lesssim 0.15\mu m$. This confirms the result obtained in section 2.1 concerning the transition point between a rough and smooth object.

Figure 2.7 shows that contrast is also reduced for increasing values of n, larger numbers of scattering centres tending to 'smooth out' the speckle pattern. In addition, both figures show that for small angles of incidence (and optically rough objects) speckle contrast is unity, while for glancing angles of incidence uniform illumination results, with contrast tending toward zero.

2.3 Probability Density of Intensity

Although the intensity contrast of a speckle pattern has many applications the probability density function (from which the contrast can be derived) can, if presented in graphic form, provide additional information which may not be evident from the contrast.

In equation 2.12 we obtained expressions for p(x) and p(y) and by using the fact that $p(x,y) = p(x)p(y)$ we have the result

$$p(x,y) = \frac{1}{2\pi\sigma_x\sigma_y} \exp\left(- \frac{(x-\langle x\rangle)^2}{2\sigma_x^2} - \frac{y^2}{2\sigma_y^2} \right), \qquad (2.50)$$

where we have again assumed that $\langle y\rangle = 0$. Since x and y are not directly measurable we need to change to a set of variables which are. The most straightforward conversion is to polar coordinates where

$$x = A\cos\psi \text{ and } y = A\sin\psi. \qquad (2.51)$$

Substituting into (2.50) gives

$$p(A\cos\psi, A\sin\psi) = \frac{1}{2\pi\sigma_x\sigma_y} \exp\left(- \frac{(A\cos\psi-\langle x\rangle)^2}{2\sigma_x^2} - \frac{(A\sin\psi)^2}{2\sigma_y^2} \right). \qquad (2.52)$$

Figure 2.7 Contrast as a function of n and θ for constant σ_r

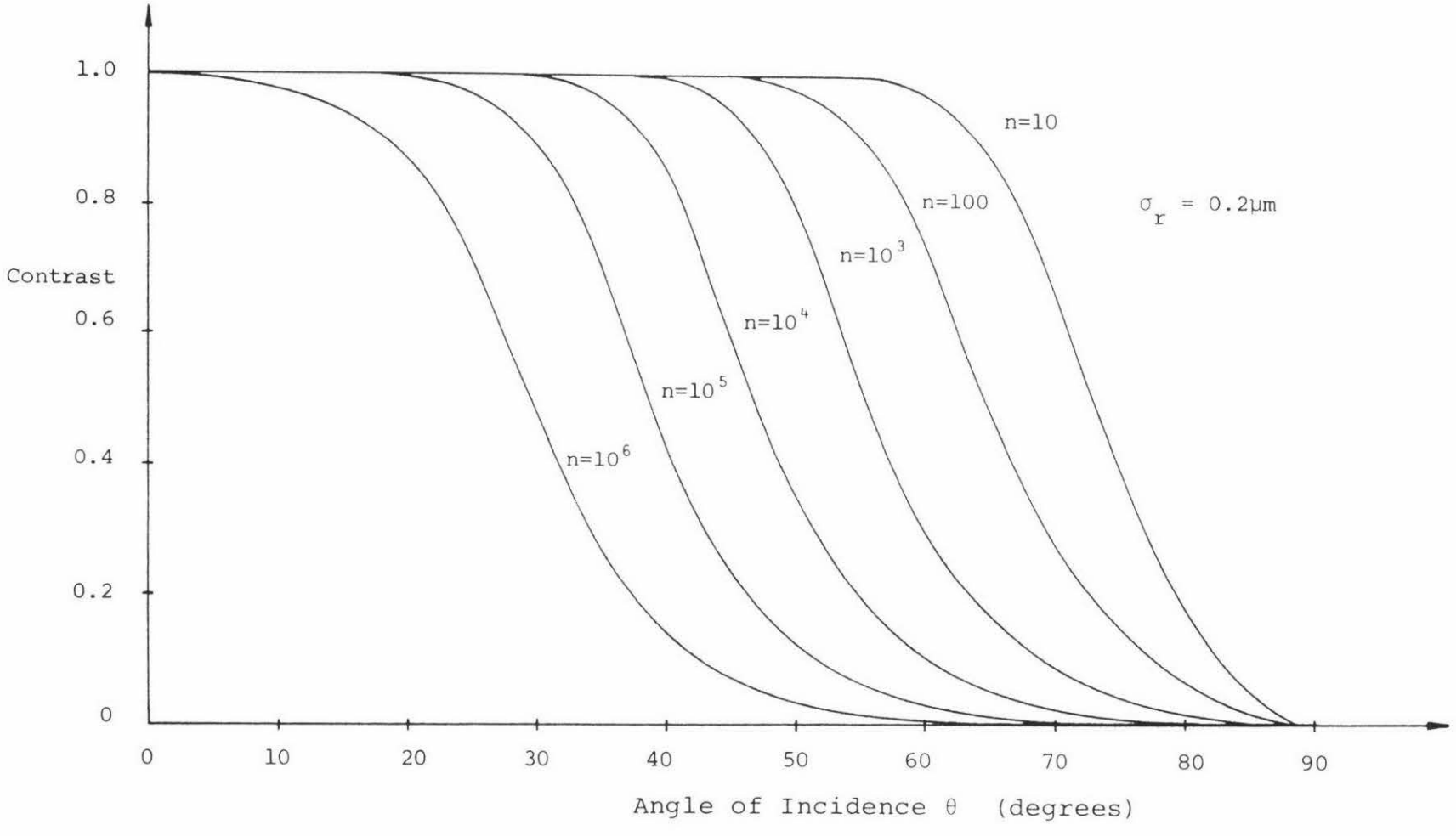

Now

$$\int_{-\infty}^{\infty}\int p(x,y)\,dxdy = \int_{-\pi}^{\pi}\int_{-\infty}^{\infty} p(A,\psi)\,dAd\psi = 1, \tag{2.53}$$

and since $dxdy = AdAd\psi$ the left hand side of this expression becomes

$$\int_{-\pi}^{\pi}\int_{-\infty}^{\infty} p(A\cos\psi, A\sin\psi)\,AdAd\psi = 1. \tag{2.54}$$

Comparison of (2.53) and (2.54) shows that $p(A,\psi) = Ap(x,y)$ so (2.52) becomes

$$p(A,\psi) = \frac{A}{2\pi\sigma_x\sigma_y}\exp\left(-\frac{(A\cos\psi-\langle x\rangle)^2}{2\sigma_x^2} - \frac{(A\sin\psi)^2}{2\sigma_y^2}\right). \tag{2.55}$$

From probability theory we know that

$$p(A) = \int_{-\pi}^{\pi} p(A,\psi)\,d\psi. \tag{2.56}$$

This integral is rather complex and rather than reproduce the solution here the interested reader is referred to Beckmann {ref 2.1 p 124} who produces the result

$$p(A) = \frac{A}{\sigma_x\sigma_y}\exp\left(-\frac{\langle x\rangle^2}{2\sigma_x^2} - \frac{(\sigma_x^2+\sigma_y^2)A^2}{4\sigma_x^2\sigma_y^2}\right)\times$$

$$\times \sum_{m=0}^{\infty}(-1)^m \varepsilon_m I_m\left(\frac{\sigma_x^2-\sigma_y^2}{4\sigma_x^2\sigma_y^2}.A^2\right) I_{2m}\left(\frac{\langle x\rangle A}{\sigma_x^2}\right), \tag{2.57}$$

where $\varepsilon_m = \begin{cases}1 & \text{for } m=0\\ 2 & \text{for } m\neq 0\end{cases}$ and $I_m(z)$ is the modified Bessel function of order m.

With this result obtained we will now consider a number of physical situations which will be covered in the experimental part of this thesis.

2.4 Probability Density Function for a Fully Developed Speckle Pattern

First consider a normally illuminated surface with a roughness such that $\sigma_\phi >> \pi$. From considerations in section 2.2 we know that the resultant speckle will be fully developed i.e. it will have a contrast of one. Since these conditions will apply for the majority of natural surfaces, it is interesting to consider what form the probability density of the speckle intensity will take.

If $\sigma_\phi >> \pi$, $p(\phi)$ will be practically flat over the primary interval $(-\pi \rightarrow \pi)$ and we can simplify equation 2.4 to give

$$\begin{aligned} p(\phi) &= \frac{1}{2\pi} \text{ for } |\phi| \leq \pi \\ &= 0 \text{ for } |\phi| > \pi, \end{aligned} \tag{2.58}$$

since all phase shifts outside the primary interval will have an equivalent phase shift ν less than π, i.e. for $|\phi| > \pi, \phi = q\pi + \nu$ where q is an integer.

This being the case, equations 2.38, 2.39 & 2.43 simplify to give

$$\langle x \rangle = 0 \text{ and} \tag{2.59}$$

$$\sigma_x^2 = \sigma_y^2 = \tfrac{1}{2} n a^2 \tag{2.60}$$

p(A) then becomes, after substitution and simplification

$$p(A) = \frac{2A}{na^2} \exp\left(-\frac{A^2}{na^2}\right) \sum_m (-1)^m \varepsilon_m I_m(0) I_{2m}(0), \tag{2.61}$$

and since

$$I_m(0) = \begin{cases} 1 \text{ for } m = 0 \\ 0 \text{ for } m \neq 0 \end{cases},$$

the only non-zero solution occurs when m=0. p(A) is then

$$p(A) = \frac{2A}{na^2} \exp\left(-\frac{A^2}{na^2}\right). \tag{2.62}$$

To find p(I) we note that

$$\int_0^\infty p(A)\,dA = \int_0^\infty p(I)\,dI = 1, \tag{2.63}$$

as p(A) is not normalized i.e. $\int_{-\infty}^{\infty} p(A)\,dA = 2$.

In addition

$$I = |A|^2 \rightarrow dI = 2AdA,$$

therefore

$$p(I) = \frac{1}{2A}p(A) = \frac{1}{na^2}\exp\left(-\frac{A^2}{na^2}\right) = \frac{1}{2\sigma_x^2}\exp\left(-\frac{I}{2\sigma_x^2}\right), \tag{2.64}$$

since $\sigma_x^2 = \sigma_y^2 = \frac{1}{2}na^2$.

Now <I> from equation 2.9 is just

$$\langle I\rangle = \sigma_x^2+\sigma_y^2+\langle x\rangle^2+\langle y\rangle^2 = 2\sigma_x^2, \tag{2.65}$$

therefore

$$p(I) = \frac{1}{\langle I\rangle}\exp\left(\frac{-I}{\langle I\rangle}\right). \tag{2.66}$$

An additional function which can also be easily obtained is the probability that the intensity exceeds I since

$$P(I) = \int_I^\infty p(I)\,dI = \frac{1}{\langle I\rangle}\int_I^\infty \exp\left(\frac{-I}{\langle I\rangle}\right)dI$$

$$= \exp\left(\frac{-I}{\langle I\rangle}\right), \tag{2.67}$$

which is directly proportional to p(I). These two functions are plotted in figure 2.8 where it can be seen that the most probable intensity in a fully developed speckle pattern is zero.

2.5 Probability Density of a Partially Polarized Speckle Pattern

The results obtained in equations 2.66 and 2.67 were derived by assuming that all the light amplitudes were scalars. This assumption is only correct if the light producing the speckle pattern is plane polarized. In many situations this is not the case and to produce probability densities for such speckle patterns requires a somewhat different approach. The particular situation to be considered in this thesis is the speckle pattern produced by a partially polarized laser. As will be explained in chapter three such a laser divides its power between two orthogonal planes of polarization. Each of these components will produce a separate speckle pattern so that the resultant amplitude will, from figure 2.9, be

$$\underset{\sim}{A}_T = A_x\underset{\sim}{i}+A_y\underset{\sim}{j}, \tag{2.68}$$

where $\underset{\sim}{i}$ and $\underset{\sim}{j}$ are orthogonal unit vectors. With this result the net intensity will be

$$I_T = |\underset{\sim}{A}_T|^2 = A_x^2+A_y^2 = I_x+I_y. \tag{2.69}$$

The total observed intensity is therefore equal to the sum of the intensities of the two orthogonal components. If the two speckle patterns are not fully correlated (i.e. if they are not identical in form and position) then the probability of a zero intensity in the pattern will be reduced because of the overlapping of speckle. The probability density and contrast for such a situation are derived in Appendix A and plotted in figures 2.10 and 2.11.

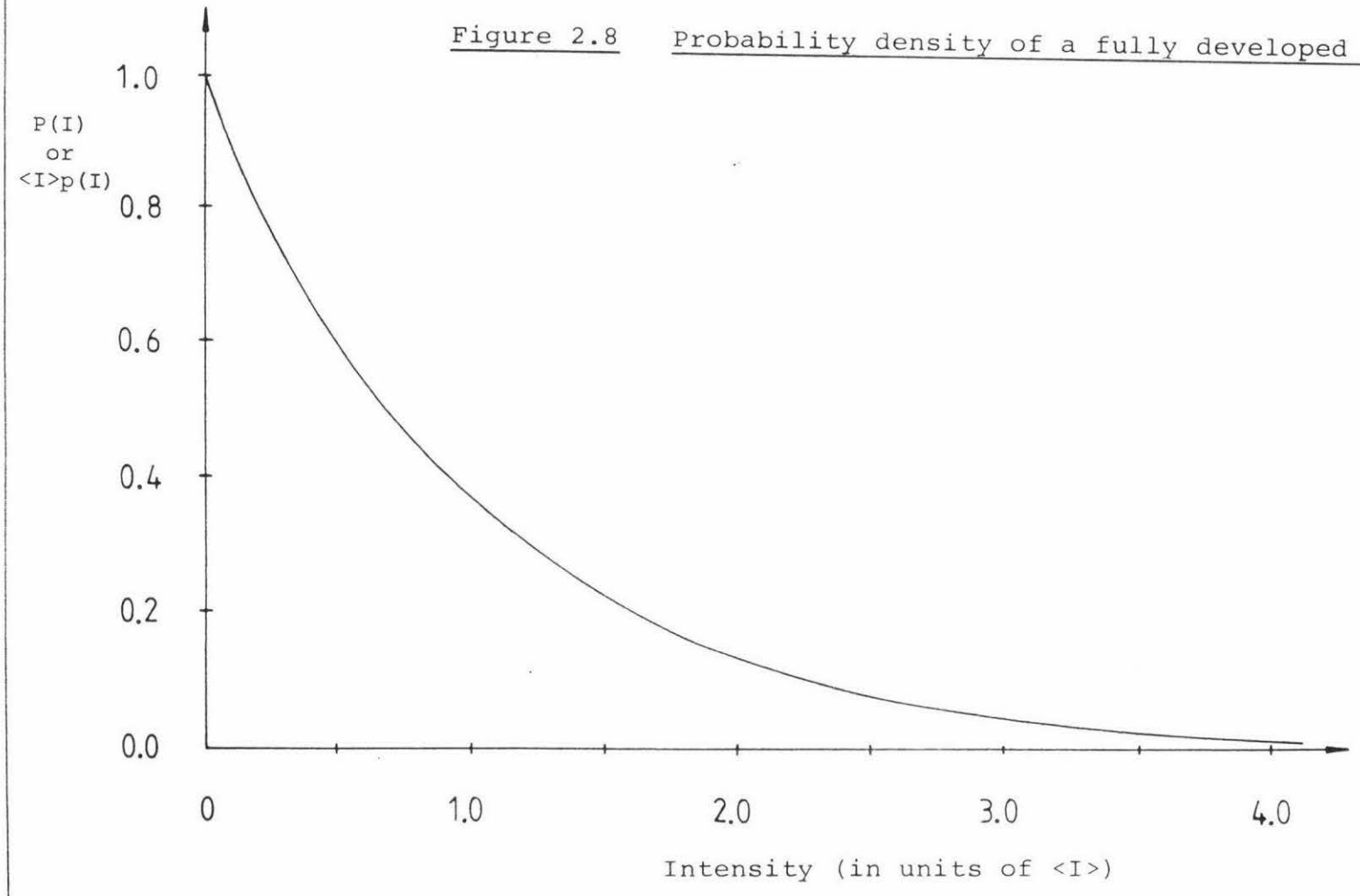

Figure 2.8 Probability density of a fully developed speckle pattern

Figure 2.9 Amplitude composition for a partially polarized speckle pattern

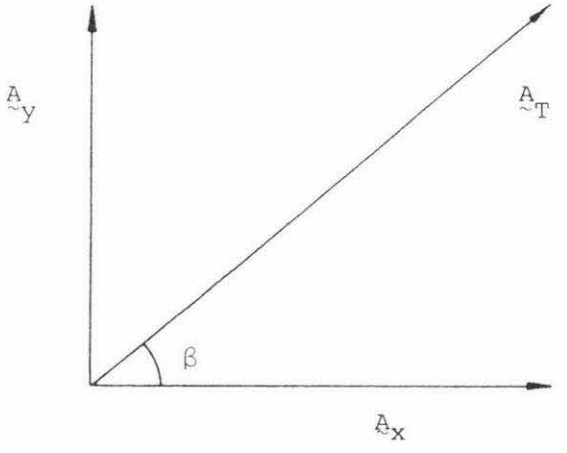

Figure 2.10 Probability density function for the sum of two speckle patterns as a function of $I_x:I_y$

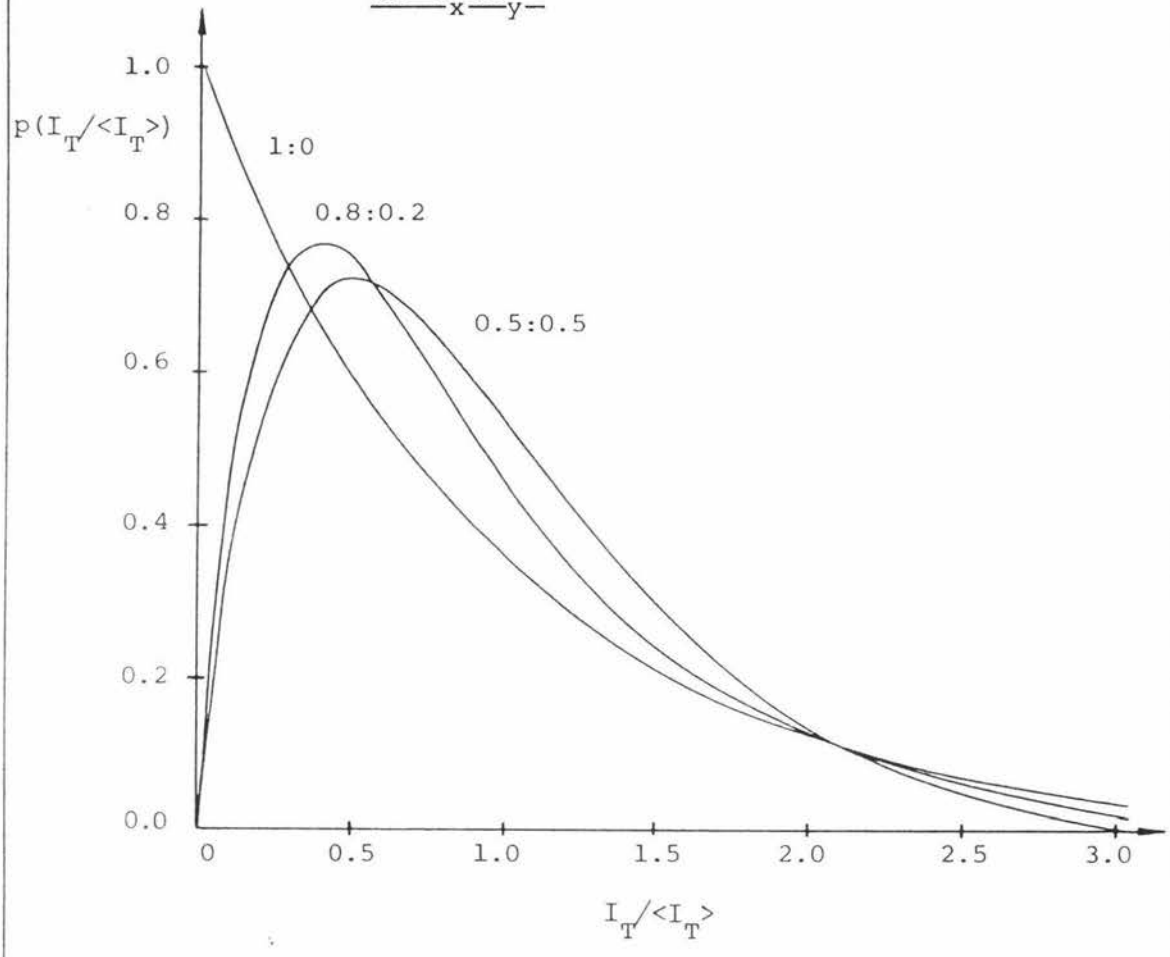

Figure 2.11 Contrast for the sum of two speckle patterns with $\langle I_T \rangle = 1$

These results show that the probability of a low intensity is reduced as the amplitudes of the components become more similar, reaching a minimum when $\langle I_x \rangle = \langle I_y \rangle$.

Results obtained in chapter six indicate that when partially polarized light is scattered from a metallic surface little decorrelation of the two components results. This means that the speckle pattern will still have a probability density function given by equation 2.66. It is probable that if such light were scattered from a non-metallic surface decorrelation of the pattern would result. Figure 2.12, reproduced from Goodman's work {ref 2.2 p 25}, shows this situation for $\langle I_x \rangle = \langle I_y \rangle$, and for various values of correlation coefficient C_{12}.

2.6 Probability Density of a Speckle Pattern Produced by a Surface with a Low Value of σ_ϕ

For smooth surfaces, or objects illuminated at glancing angles of incidence, we can no longer assume that σ_ϕ is large and so must use equation 2.57 as it stands. From equation 2.64 we know that

$$p(I) = \frac{1}{2A} p(A)$$

(2.57) therefore becomes

$$p(I) = \frac{1}{2\sigma_x \sigma_y} \exp\left(\frac{-\langle x \rangle^2}{2\sigma_x^2} - \frac{I(\sigma_x^2+\sigma_y^2)}{4\sigma_x^2\sigma_y^2} \right) \times$$

$$\times \sum_m (-1)^m \varepsilon_m I_m\left(\frac{\sigma_x^2-\sigma_y^2}{4\sigma_x^2\sigma_y^2} \cdot I \right) I_{2m}\left(\frac{\langle x \rangle I^{\frac{1}{2}}}{\sigma_x^2} \right). \qquad (2.70)$$

Numerically this equation is not easily solved since $I_m(x)$ is given by the series {ref 2.1 p 183}

$$I_m(x) = \sum_{s=0}^{\infty} \frac{1}{s!(m+s)!} \left(\frac{x}{2}\right)^{m+2s}, \qquad (2.71)$$

Figure 2.12 Probability density functions of intensity for the sum of two speckle patterns with $\langle I_x \rangle = \langle I_y \rangle$ and correlation coefficients C_{12}

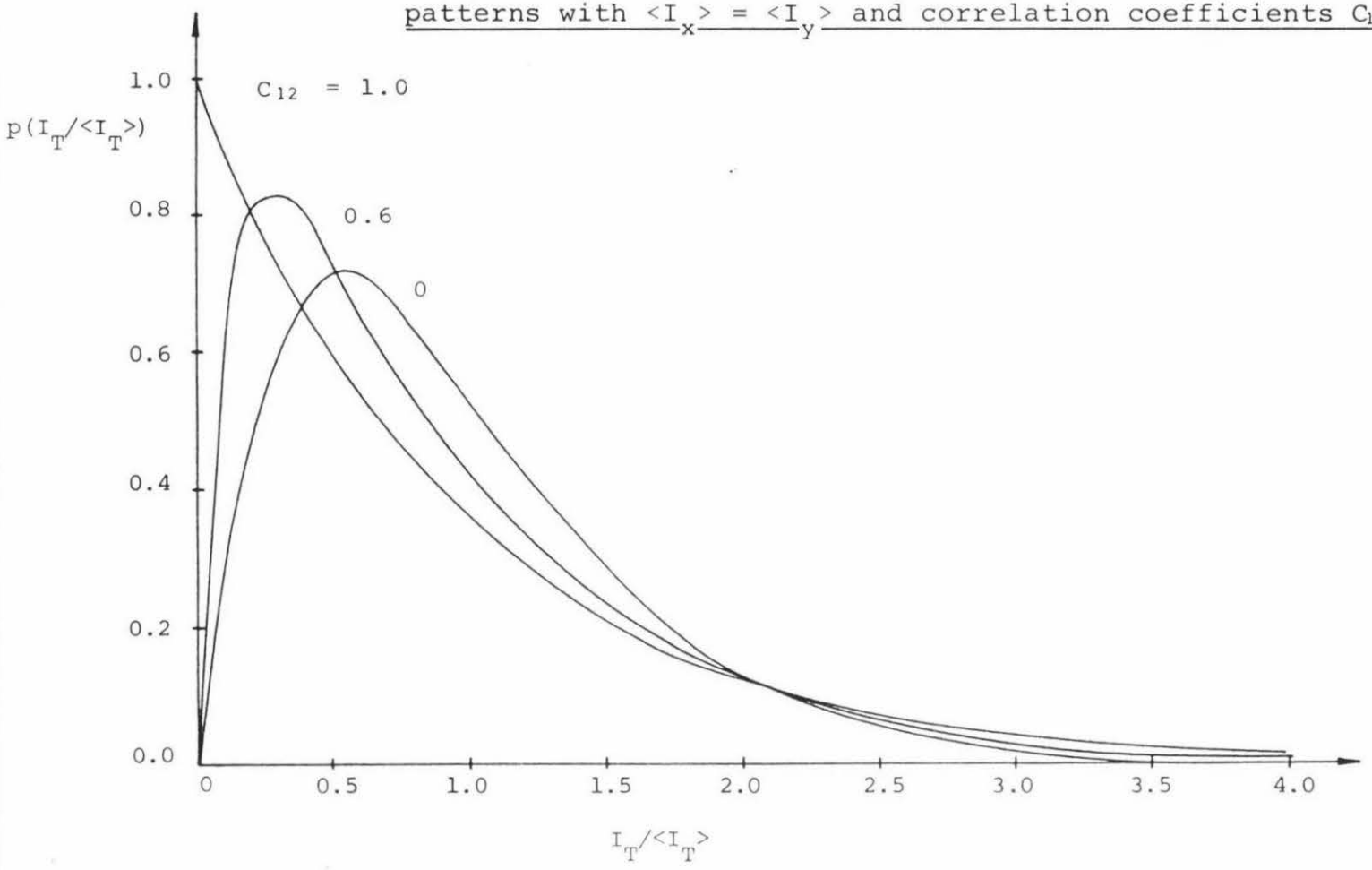

and for m = 0 values of x = 40 and s = 15 will set $\left(\frac{x}{2}\right)^{m+2s} \simeq 1x10^{39}$, a number larger than the computer used to perform the calculations in this thesis could manipulate. Because of this problem direct comparisons could not be made between experimental and theoretical probability density curves, but some idea of the form expected can be obtained from figure 2.13 which reproduces a series of curves drawn by Asakura {ref 2.4 p 23} for a variety of rough surfaces. If we assume that these results were obtained using normal illumination of the object we can calculate, using equation F.3, σ_ϕ for each of these curves. The results are listed below (for λ = 632.8nm).

Surface	σ_r (μm)	σ_ϕ (radians)
A	0.140	2.78
B	0.070	1.39
C	0.047	0.93
D	0.040	0.79

2.7 Speckle Size and Displacement

So far we have considered speckle statistics in terms of the contrast and probability density functions. These results can be used to obtain information about the scattering surface and illuminating light source. However they cannot give information about the average size of the speckle or the effect that a change in the position of the object would have. Such information can be found by determining the auto and cross-correlation functions for the speckle pattern.

Speckle Size

In many experiments involving speckle patterns it is important that the detector used is smaller than the smallest speckle produced, otherwise information can be lost. For this reason knowledge of the characteristic

Figure 2.13 Probability density function of speckle intensity in the diffraction plane as a function of surface roughness

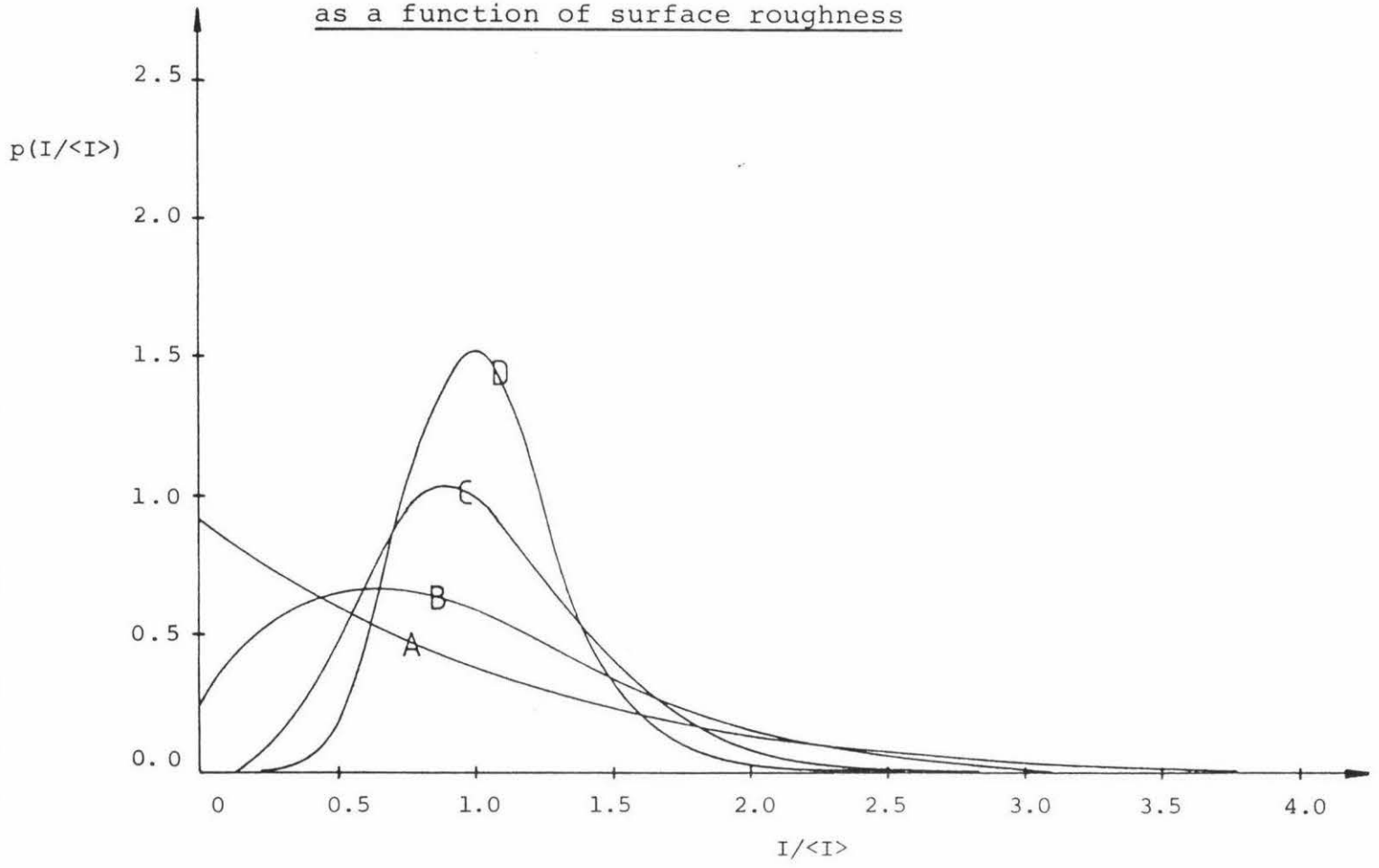

A,B,C,D : see text

size of speckles for a particular optical arrangement is necessary. Rigorous derivation of this size is possible by determining the width of the autocorrelation function for the speckle pattern, but does involve fairly complex mathematics (for details see ref 2.2 section 2.5.1). The following, rather simplistic, model produces identical results with considerably less effort.

Consider figure 2.14 which shows a circular beam of collimated light illuminating a sheet of ground glass. Each scattering centre on the surface may be considered to be a tiny imperfect converging or diverging lens, at some arbitrary inclination to the normal. If the surface is rough enough scattering centres over the whole object with a common focal point will contribute light to produce a speckle at that point. If we replace this particular group of 'pseudo lenses' by a lens having an identical focal point but a diameter >d the speckle will have a characteristic size given by the radius of the Airy disc produced by this lens, i.e.

$$\delta = \frac{0.61\lambda}{n'\sin\alpha}, \tag{2.72}$$

which, for small angles α, becomes

$$\delta = \frac{0.61\lambda}{\frac{1}{2}n'd/L} = \frac{1.22\lambda L}{n'd}. \tag{2.73}$$

Therefore the diameter of the average speckle (i.e. the distance from minimum to minimum) will be

$$2\delta = \frac{2.44\lambda L}{n'd}. \tag{2.74}$$

In situations where image or subjective speckle is being studied the limiting aperture in the system is now a real lens (see figure 2.15) so that only light from a small area on the surface will contribute to the intensity of each speckle. This arrangement will also have a speckle size given by the diameter of the Airy disc produced by the lens,

Figure 2.14 Formation of objective speckle

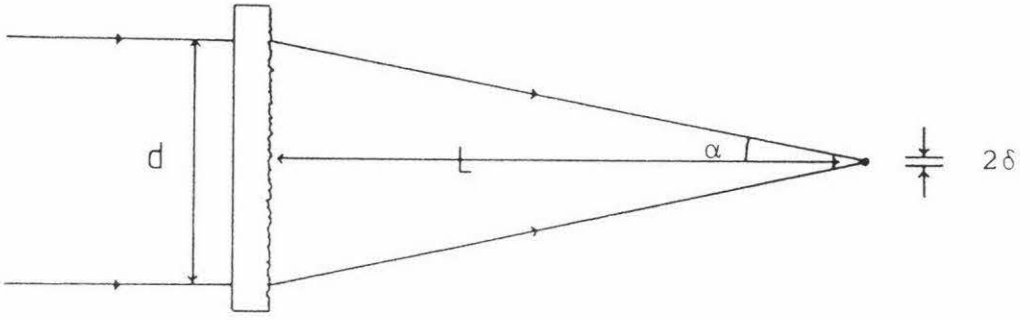

Figure 2.15 Formation of subjective speckle

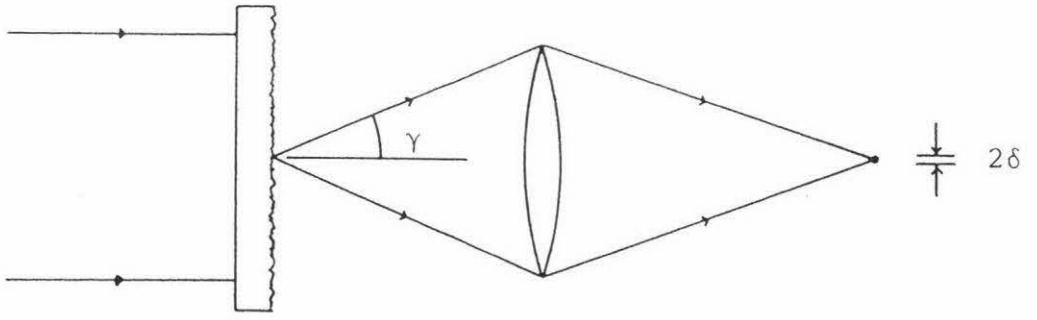

i.e.

$$2\delta = \frac{1.22\lambda}{N.A.}, \qquad (2.75)$$

where N.A. = n'sinγ, the numerical aperture of the lens. Note that both these results are twice as large as the values obtained by other writers {ref 2.2 p 207} who used the radius, rather than the diameter of the Airy disc as a measure of speckle size.

To indicate the wide range of speckle sizes that can be produced consider the following results obtained using λ = 632.8nm and L = 20cm for objective speckle. If

d = 10cm then 2δ = 3μm

d = 100μm then 2δ = 3mm

The optical arrangement must therefore be carefully selected so that the speckle size produces optimum results from the available detector.

Speckle Displacement

As we have seen in previous sections speckle is produced by the complex interference of light scattered from a rough surface. If the surface were to be displaced by a small amount one would therefore expect that the speckle pattern would be displaced by an equal amount, and that as long as the displacement did not introduce too many new scattering centres into the illuminating beam little decorrelation of the speckle would occur. Observation of real speckle patterns shows that this is indeed the case. There is thus the possibility of producing a non-contact method for the measurement of in-plane displacement of an object by cross-correlating the speckle patterns before and after the displacement. Movement can then be deter-

mined by finding the lag at which maximum correlation occurs between the two patterns. Experiments along these lines will be discussed in more detail in chapter six.

3 Description of the Experimental Apparatus

In this chapter the experimental apparatus and arrangements used to test the results obtained mathematically in the last chapter will be described.

Five main experiments were carried out and are listed below.

i) Measurement of the probability density function and contrast of a fully developed speckle pattern using a linearly polarized laser.

ii) Measurement of the probability density function and contrast of a partially polarized speckle pattern.

iii) Measurement of the probability density function and contrast as a function of incidence angle and surface roughness.

iv) Displacement measurements of translating and rotating objects.

v) Measurement of speckle size.

In addition a number of tests were made on the various pieces of apparatus used, to check their suitability for performing the above experiments. These will be described in chapter 6.

What follows is a brief description of the apparatus used.

3.1 Apparatus Summary

All experiments (apart from (i) above) were carried out on a heavy steel plate (approximate size 90 x 70 x 4cm) mounted at each corner on a pile of newspapers. The resultant system was therefore reasonably well isolated

from external movement (although this was not a critical factor in most experiments as exposures were made in $\sim$ 65ms) and ideally suited for magnetically mounting optical apparatus.

The light source used was a Spectra Physics helium-neon laser with a rated output power of 4mW. This laser was only partially polarized and so experiments requiring linear polarization (such as (i) above) were carried out using an 80mW polarized laser.

To allow for a variety of possible apparatus positions the 4mW laser was mounted on an adjustable lamp jack which in turn was bolted to the steel table. All lenses, filters, and apertures were mounted on plastic holders which could be attached to magnetic stands. These proved to be very stable and allowed easy adjustment of component positions.

Two devices were built which allowed a selected object to be moved a small measured distance. The first was a translating stage which caused a block of aluminium (to which the test object was attached) to move in a vertical direction as a micrometer was adjusted, while the second rotated the test object about a fixed axis. Both pieces of apparatus were attached to the steel table with strip magnets for stability.

The final component in the system was the detector. This was mounted in a perspex case and placed on another lamp jack.

An overall plan view of the experimental apparatus arranged for measuring surface displacement is pictured in figure 3.1. Included in this diagram are the microprocessor and oscilloscope used to record and analyse the optical data.

We will now consider each component of the optical system in more detail.

Figure 3.1

Experimental Apparatus

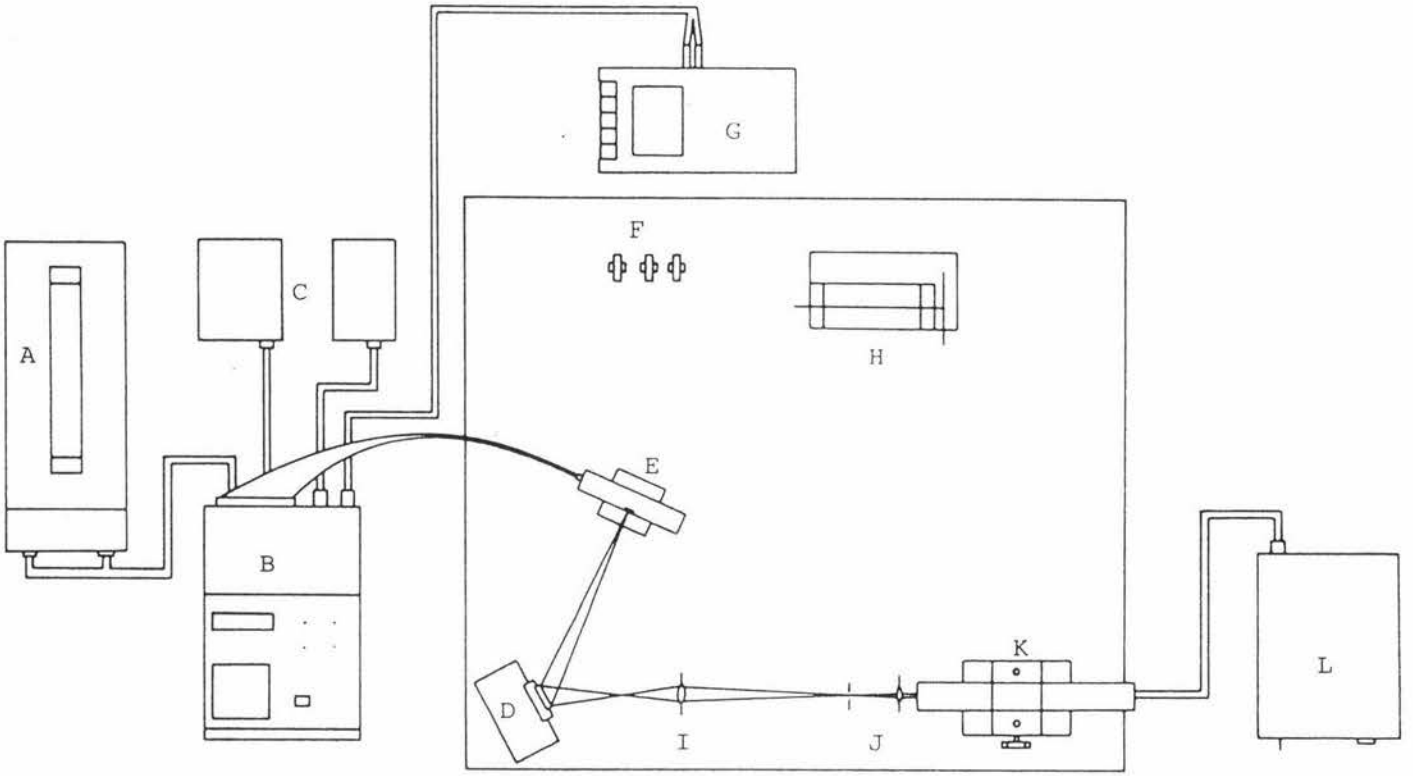

Scale 1:10

3.2 The Laser

The laser used in most of the above mentioned experiments was a 4mW helium-neon laser operating in the TEM_{00} mode with a measured beam divergence of 1.2mrad. This laser was found to have adequate brightness for most of the experiments although some of the rougher objects used did produce fairly weak speckle patterns. Its chief shortcoming stemmed from the fact that it was not linearly polarized and for one set of measurements it was necessary to use an 80mW linearly polarized laser. Unfortunately this laser was fairly large and so could not be used in conjunction with the steel table for some of the more difficult experiments . To clarify this polarization problem the following excerpt (from ref 3.1 section 2) is given.

Partially Polarized Lasers

All lasers produce an output which, depending on the design of the laser, will be either a single linearly polarized beam or a beam comprised of two orthogonal, linearly polarized components. Lasers having an unspecified orthogonal polarization (often incorrectly referred to as unpolarized or randomly polarized) have an output comprised of two collinear beams of linearly polarized light of slightly differing wavelengths, separated in frequency by c/2L where L = optical path length of the laser cavity. The planes of polarization of these beams are orthogonal to each other. The physical orientation of these planes does not shift randomly over time, but is permanently fixed in relation to the physical structure of the laser - the particular orientation being dependent on the various asymmetries of the plasma tube.

While the power output in plane A plus plane B is always 100% of total power, mode sweeping (illustrated in figure 3.2) causes the component values of A and B to shift

Figure 3.2 Laser power shifts caused by mode sweeping

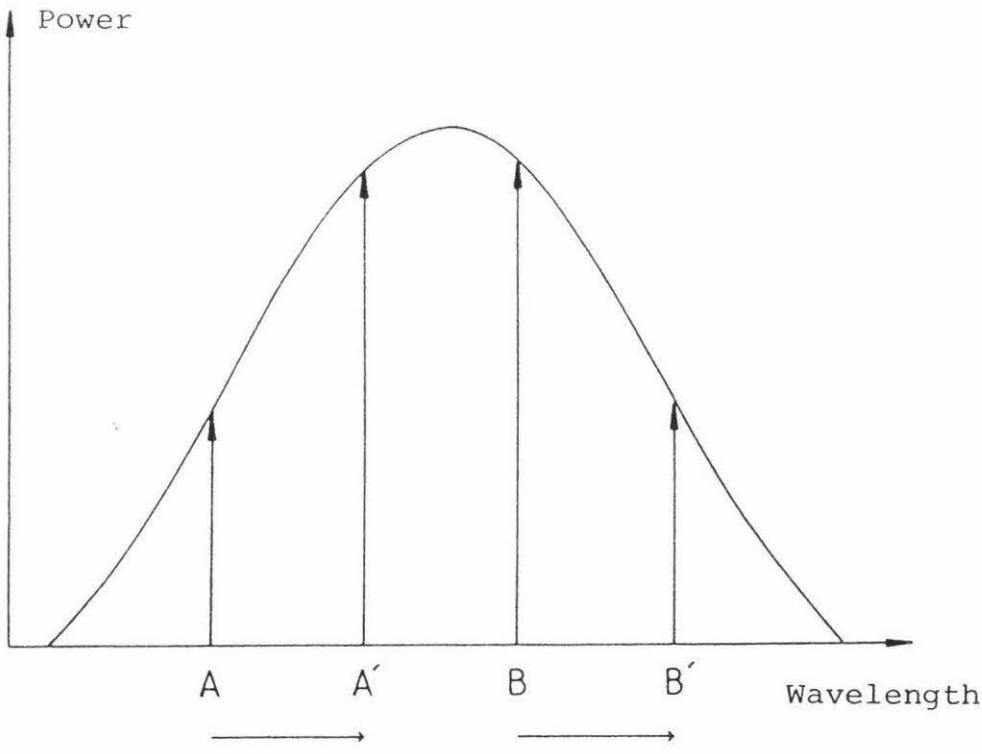

randomly and approximately inversely with respect to each other over time.

3.3 Lenses, filters, and apertures

Only four lenses were used in the experiments. They had the following characteristics:

i) 2 convex lenses with 72mm focal lengths and diameters of 1cm.

ii) 2 microscope objectives with focal lengths of 16 and 10mm and diameters of 5mm. (All focal lengths ± 1mm).

The two larger lenses were used as part of the spatial filter and to adjust the spot size on the object. They were mounted in holes drilled in squares of perspex and held in place with a drop of glue. The smaller microscope objectives were used to expand the beam up to a large enough size (3→4cm) so that the detector was uniformly illuminated. They were also used to adjust the sensitivity of the displacement measurements. Because of their small size and thin edges these lenses were mounted between plastic slide holders which clipped together.

Thus mounted, all lenses could be clipped onto a stand which was then fastened to the steel table by a strong magnet. (See figure 3.3 for diagrams).

For many of the experiments (in particular, measurements of surface roughness at glancing angles of incidence) the beam intensity was too high, so a number of attenuators were made by mounting partially exposed sections of film on a magnetic stand. Because they were often scratched the films were placed within the spatial filter (to be discussed in section 3.6) to remove the speckle that would otherwise have been produced.

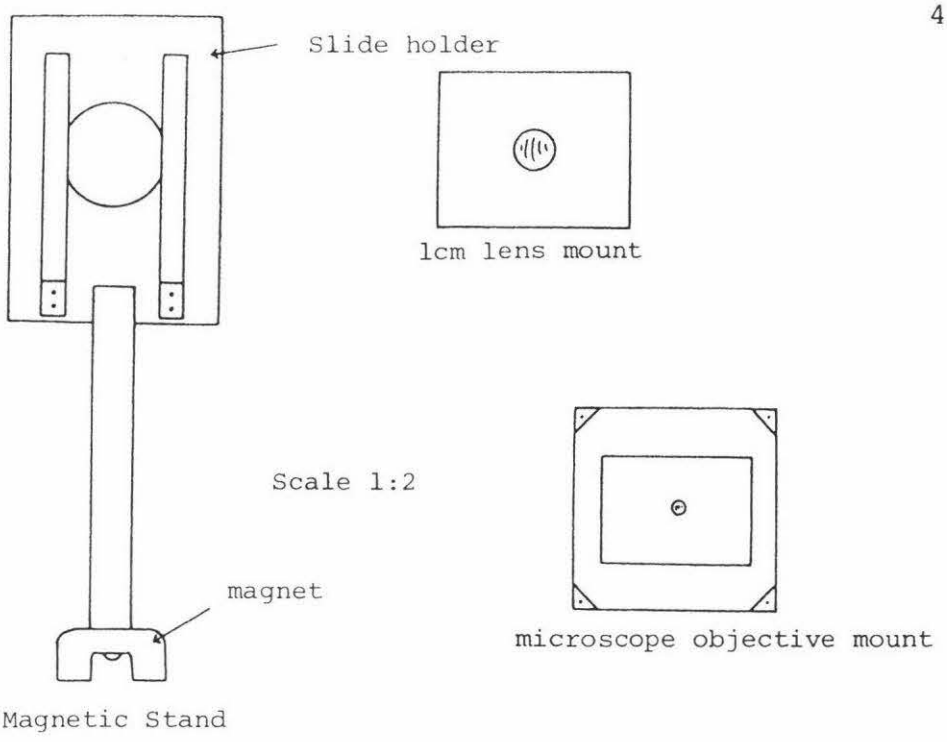

Figure 3.3 Magnetic stands and lens holders

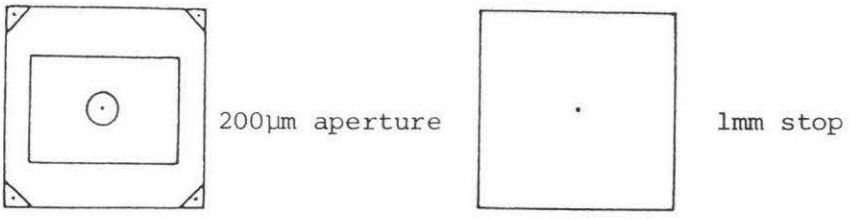

Figure 3.4
Apertures

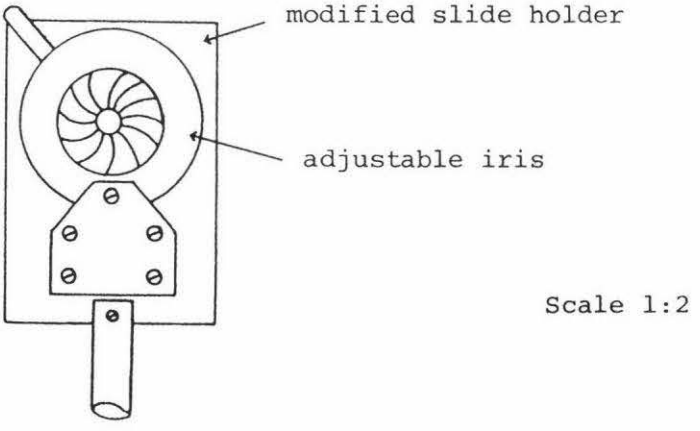

To adjust the beam size & block off unwanted light three apertures were used with the following characteristics:

i) A 200μm pinhole for use in the spatial filter (mounted between slide holders).

ii) A 1mm hole drilled in a sheet of aluminium to block off unwanted light. (This clipped directly onto a magnetic stand).

iii) An adjustable iris (from 0.5→30mm) for varying speckle size. (Since from equations 2.72 and 2.75 we saw that speckle size is dependent on the angles α and β which can both be varied by introducing an aperture into the system.)

To test the effect polarizing the beam had on probability density and contrast, a slide of polaroid was also used. This clipped directly onto a magnetic stand.

Diagrams of the above mentioned components may be seen in figure 3.4.

3.4 The Translating and Rotary Stages

These two pieces of apparatus were most important as they allowed a test object to be mounted and moved over very small distances - a necessary requirement for both displacement and surface roughness measurements.

The first device to be considered is the translating stage which is drawn in elevation and plan view in figure 3.5. A block of aluminium, so shaped that it can slide freely up and down in a set of grooves, sits on the barrel of a micrometer which is bolted to a thick perspex and wood stand. By adjusting the micrometer the object could be moved up or down over the required distance.

Figure 3.5 The translating stage

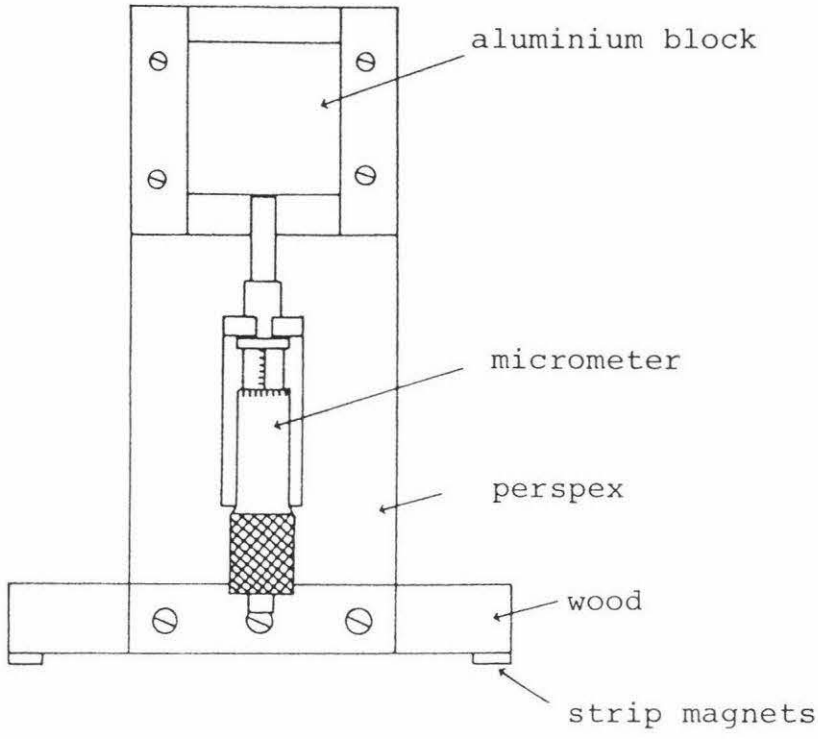

Scale 1:2 Elevation

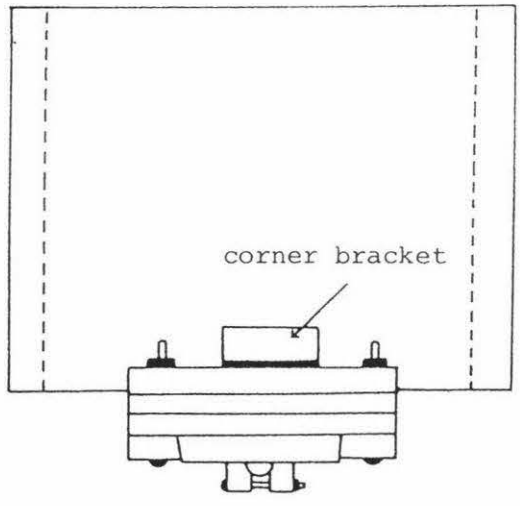

Plan View

The second device is the rotary stage pictured in figure 3.6. The micrometer is now mounted horizontally and pushes (or pulls with the aid of a button magnet) a lever arm attached to an axle. This axle has an aluminium disc screwed to it to which various objects can be attached. Both stages have magnetic strips bonded to their bases to ensure stability, yet allowing positioning on any part of the table.

The rotary stage was found to be the more suitable device for displacement measurements because of its smoother action and greater sensitivity. (By placing objects close to the centre of the disc displacements of less than 1μm could be obtained).

3.5 Test Objects

For measurements of fully developed speckle statistics or speckle displacement, the form of the surface texture is not particularly important as long as it is optically rough and reasonably reflective (to obtain adequate light for detection). However for surface roughness measurements, the surface should have as little waviness as possible and an even degree of roughness over the whole object. To achieve this pieces of aluminium and glass (approx 2 × 3cm) were ground with various grades of carborundum grit, on plate glass, until the desired surface texture was obtained. Due to the differing hardness of these two materials it was not expected that identical surface roughness would result.

When carrying out an experiment the appropriate test object was mounted on either the translating or rotary stage with double sided adhesive tape. This was found to produce a surprisingly rigid bond.

Transmission speckle patterns (as in figures 2.14 and 2.15) were obtained by shining the laser onto one of the glass

Figure 3.6 The rotary stage

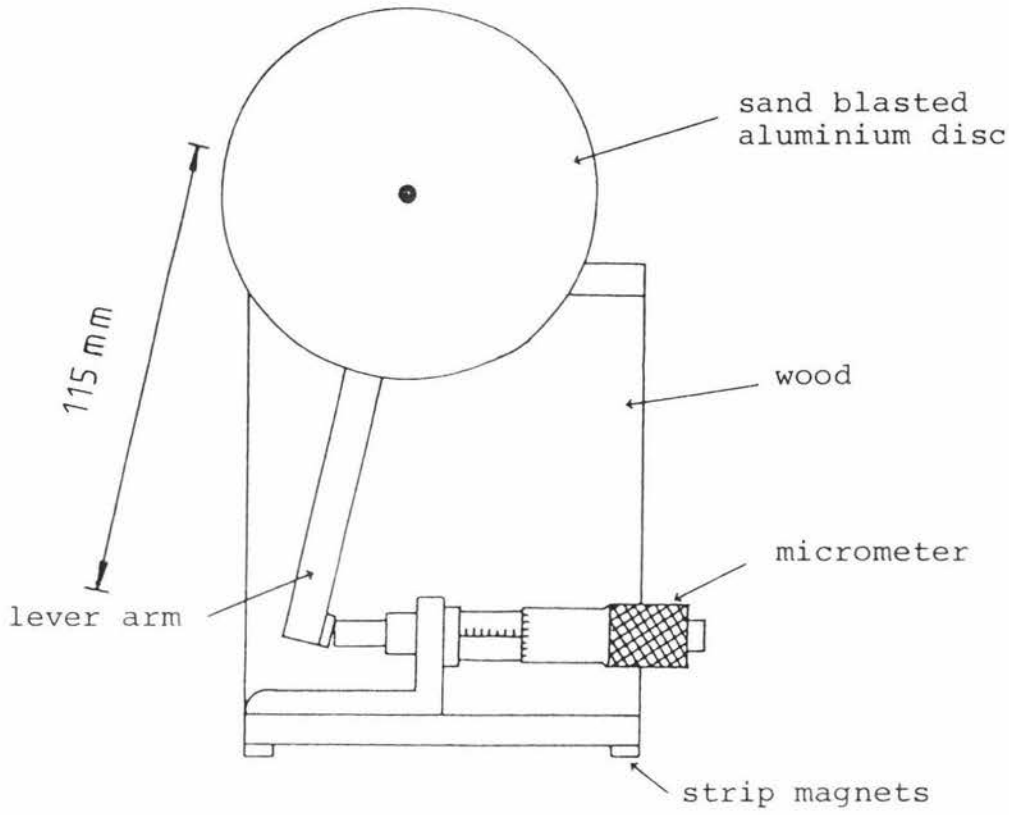

Scale 1:2

Elevation

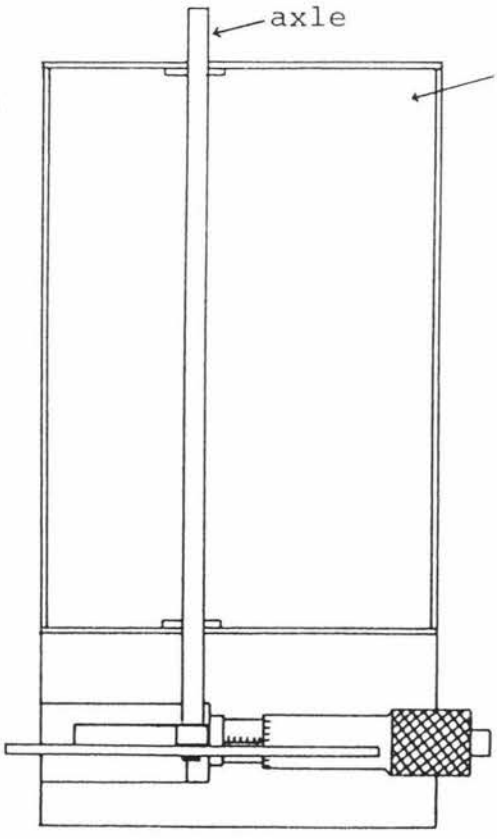

Plan view

objects which was fixed to the edge of the rotary stage.

3.6 The Spatial Filter

One item of optical apparatus which deserves special mention and which was used in many of the experiments is the spatial filter. If light from a laser is expanded using a microscope objective it is seen to contain diffraction rings and other imperfections. These result from the interference effects of light scattered by dust particles, and from mirror defects within the laser. The ideal profile for a TEM_{00} laser has a Gaussian shape. The addition of the above mentioned imperfections will lead to unwanted intensity fluctuations superimposed upon this profile (see figure 3.7) i.e.

$$I_{actual} = I_{ideal} + I_{noise}$$

I_{noise} usually varies rapidly over distances smaller than ε where ε is the distance from the central axis at which I has dropped by a factor of e^{-2}. The average spatial wavelength of the noise is therefore much less than that of the ideal beam.

If the light from the laser is observed in the focal plane of a converging lens the resultant intensity distribution will represent the optical power spectrum of the light (see figure 3.8). Because of its higher spatial frequency the noise component will be separated from the ideal curve, and may be selectively removed from the beam by introducing an aperture of the appropriate size. This selective removal of a particular band of spatial frequencies corresponds directly to the low pass filter used in electronics and so may be termed low pass spatial filtering. The optical arrangement used to achieve this is illustrated in figure 3.9.

In situations where the light intensity is too high the

Figure 3.7 Laser beam intensity profile

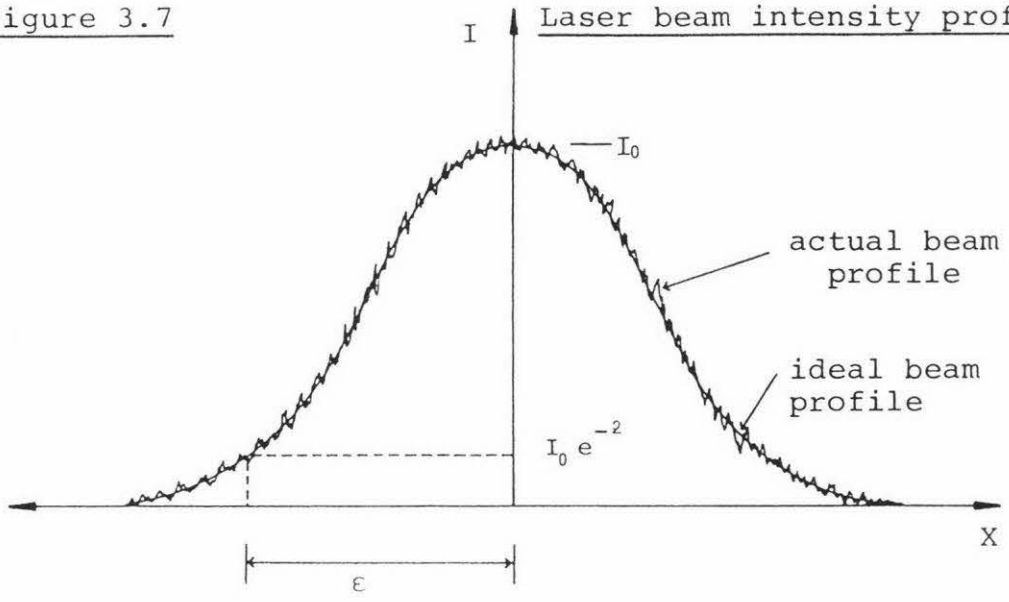

Figure 3.8 Optical power spectrum of laser beam

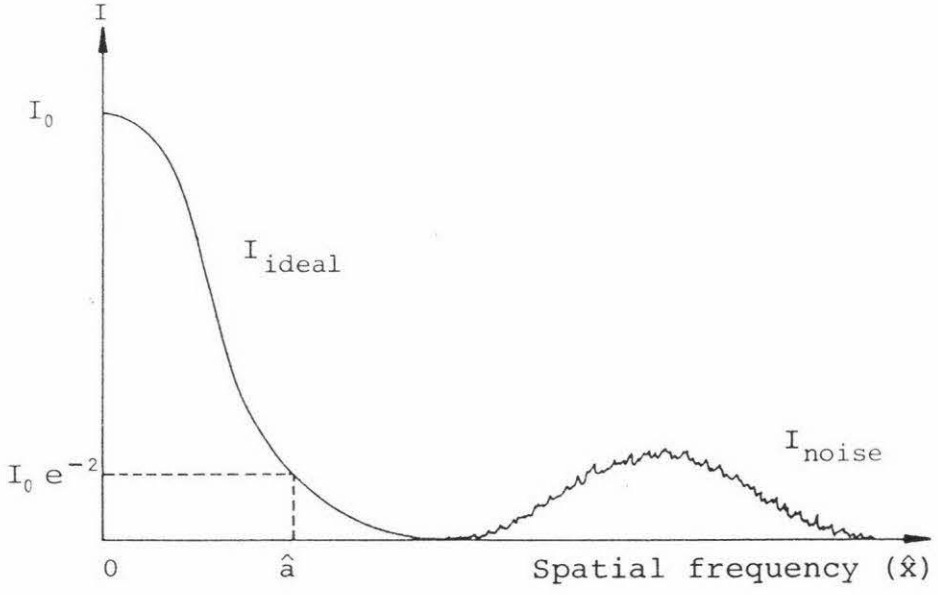

Figure 3.9 Spatial filter

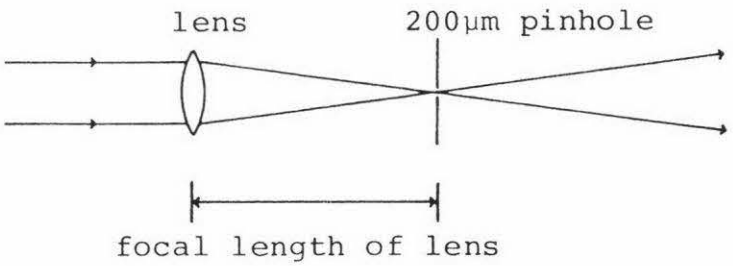

spatial filter may be used as an attenuator. If a section of partially exposed film is placed between the lens and aperture, speckle produced by imperfections in the film will be blocked because of its high spatial frequency, leaving a (reasonably) clean, attenuated beam.

3.7 The Photodiode Array and Microprocessor

These are the two most complicated components used in the experiments and so will be considered separately in the next two chapters.

3.8 The Optical Arrangements Used During the Experiments

Rather than reproduce a large number of similar diagrams for the various optical arrangements used, this section will contain all the important diagrams. These will be referred to when required. More detailed diagrams will be presented where necessary.

The three major optical arrangements used in the experimental section of this thesis are for:

i) Surface roughness measurements. This setup is pictured in figure 3.10. Light from the laser is filtered and then adjusted to give the correct spot size on the object by L_2. The light scattered in the specular direction ($\theta_{inc} = \theta_{ref} = \theta$) is collected by L_3 and expanded to evenly illuminate the array.

ii) Surface displacement measurements. In this experiment (pictured in figure 3.11) light from the laser is not filtered but falls directly onto lens L_1 which is used to adjust the apparent source of the light as seen by the object. As will be explained in chapter 6 this has the effect of varying the sensitivity of the apparatus to displacements - hence the reason for not using the spatial filter which would complicate

Figure 3.10 Surface roughness measurement

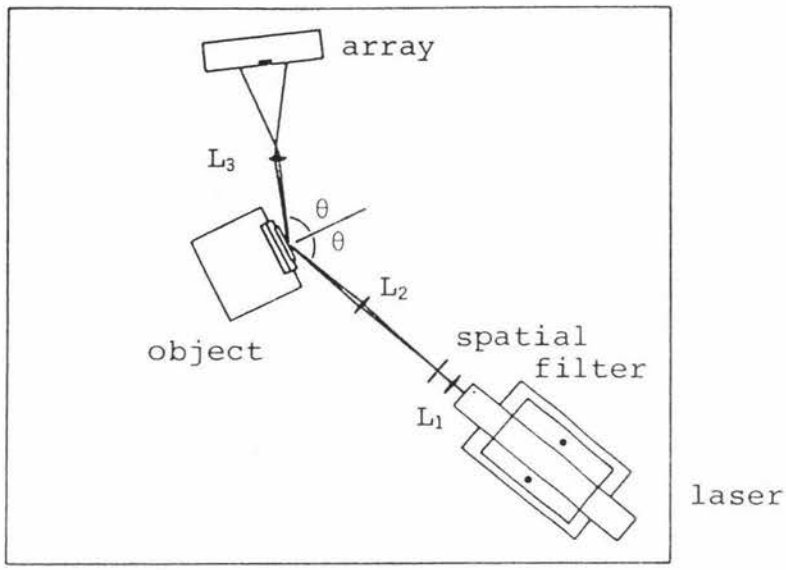

Figure 3.11 Displacement measurement using the translating stage

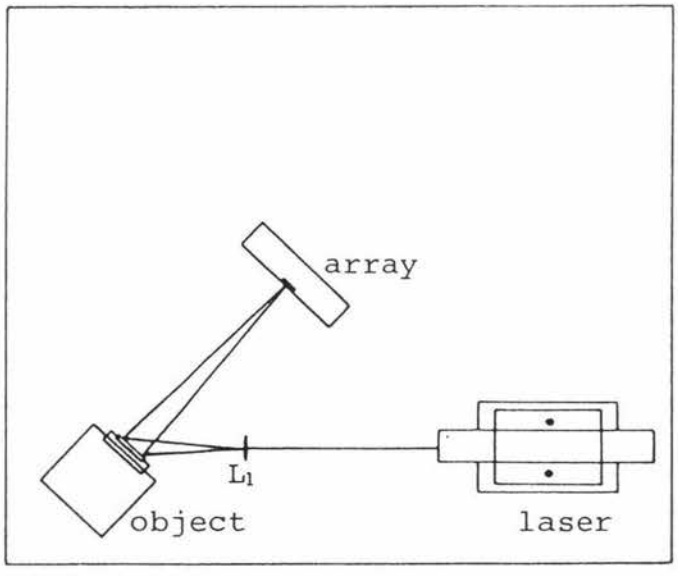

matters. The light scattered by the object is then intercepted by the array. The angle the array makes with the object normal is not critical.

iii) Surface displacement measurements using the rotary stage. In experiments where transmission speckle patterns are to be viewed this arrangement (pictured in figure 3.12) is used. Light from the laser, again unfiltered (for the reasons given above) is expanded by lens L_1 so as to fall on a glass object attached to the edge of the rotary stage. The array side of this object is roughened and so produces a speckle pattern which is then detected by the array. It has been found that the array should be kept parallel to the object, since adjustment of this angle produces undesirable variations in sensitivity.

Figure 3.12 Displacement measurement using the rotary stage

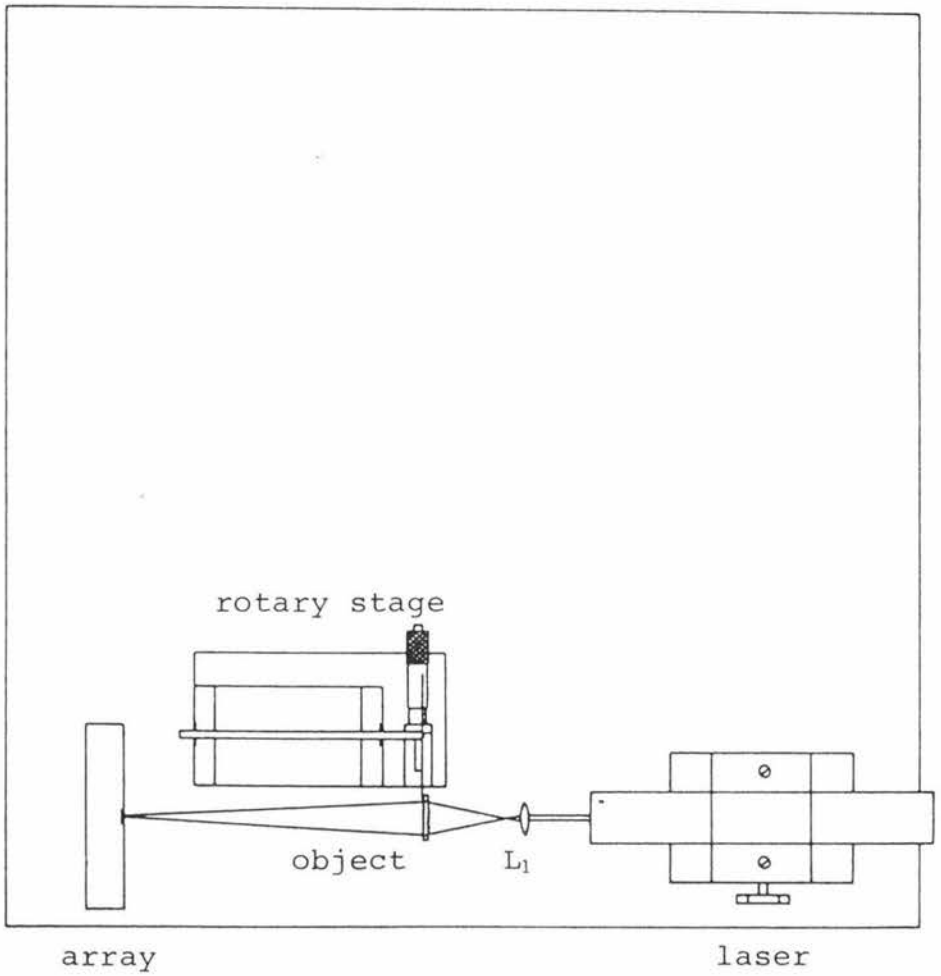

4. The Photodiode Array

Central to the success (or failure) of this thesis was the use of a charge-coupled photodiode array as the detector. This device was chosen for the three basic reasons listed below:

i) Used in conjunction with a microprocessor the array allows electronic measurement of speckle statistics without resorting to more conventional techniques (such as a vidicon and minicomputer system) which although more sophisticated are also complex and expensive.

ii) The charge-coupled device is a fairly recent addition to the optics field and so investigation of its usefulness from a general research point of view was deemed a worthwhile pursuit.

iii) Because the system is largely electronic, control is simple, and fast analysis of data is possible, unlike the standard photographic techniques which often require much time and skill in their development and analysis.

4.1 Description of the Photodiode Array

After reading the work of Stephens et al.{ref 4.1} it was decided that a Reticon 256 element linear array would be used because of its high resolution and reasonable cost.

This array (with reference to figure 4.1) is comprised of a line of 256 photodiodes (or pixels) with two 128-element shift registers placed on either side. Each pixel has an active area 16μm square with no significant gap between adjacent elements. The detector therefore has a light sensitive region 16μm wide and 4.096mm long.

Light incident on the sensing aperture generates a photocurrent which is integrated and stored as a charge on the

Figure 4.1 Simplified schematic diagram of the photodiode array

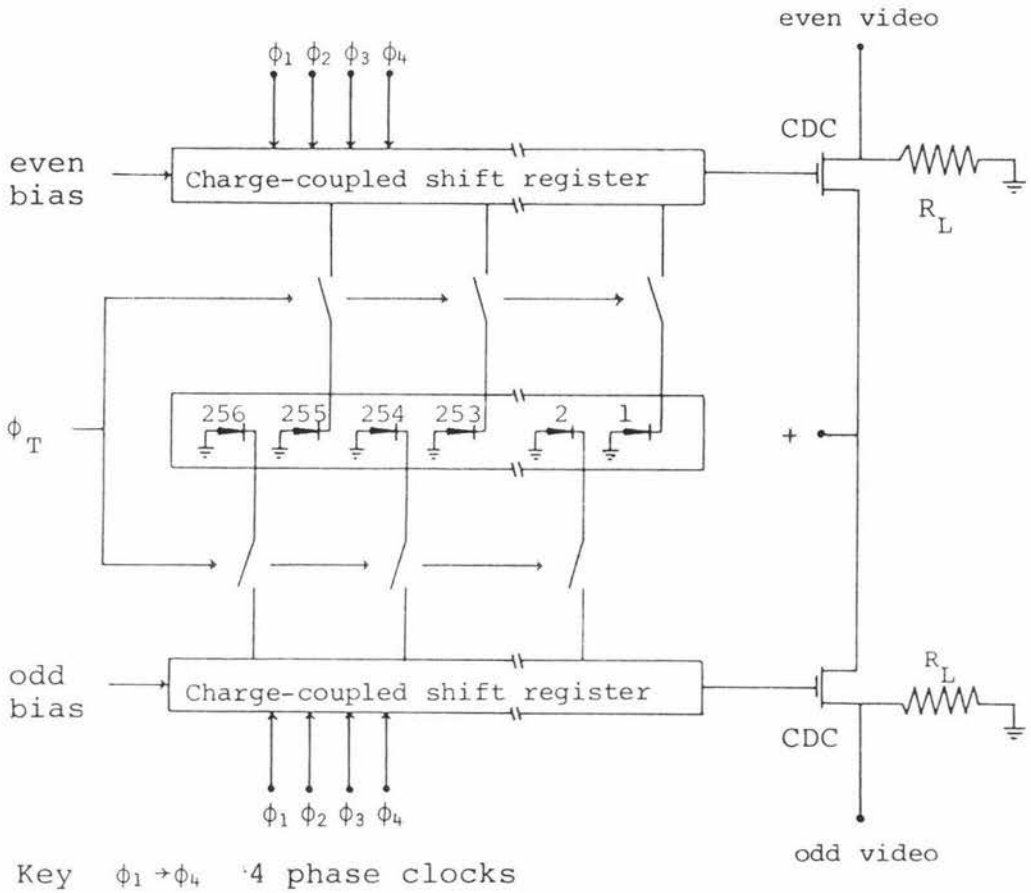

Key $\phi_1 \rightarrow \phi_4$ 4 phase clocks

ϕ_T transfer pulse

CDC Charge detection circuit

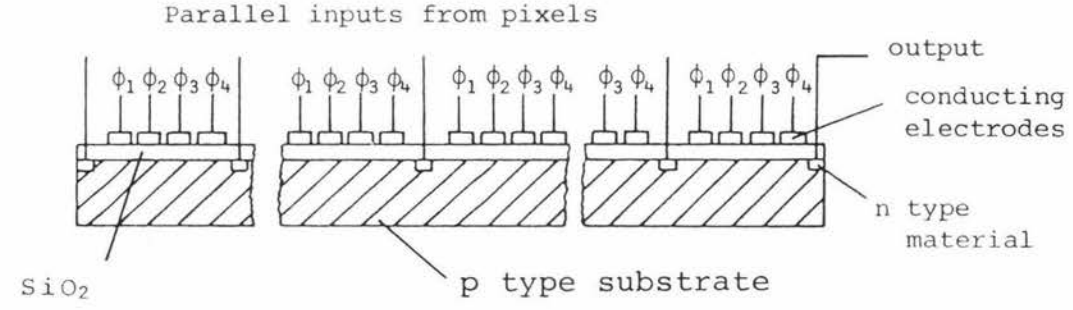

Figure 4.2 Construction of a charge-coupled device

capacitance of each photodiode. When the set integration (or exposure) period is completed analogue switches are closed causing charge to be transferred in parallel to two charge-coupled shift registers. For reasons of compactness, odd pixels (that is pixels 1,3,5 etc) have their charge transferred to a shift register on one side of the array and even pixels to one on the other. This means that the data obtained by the array is split into two separate sets which correspond to a sampling of the light intensity at 32μm intervals. This data is reassembled by a multiplexing circuit external to the array.

In figure 4.2 we see that the shift registers are made from a strip of p type silicon substrate overlaid with a thin film of SiO_2. Groups of 4 conducting electrodes connected to a 4 phase clock are bonded to this surface layer. Between each of these groups is a region of n type material which is diffused into the substrate to act as an input source for each of the pixels. The charge produced by each of these pixels is then transferred from this input source and along the substrate by proper manipulation of the voltages on the conducting electrodes. Figures 4.3 and 4.4 show this process in more detail. These figures and the following discussion have been adapted from a paper by Barbe {ref 4.2} and though not identical to the actual processes which occur in the array they do give a simplified illustration of what happens.

At time $t=t_1$ the two input regions under consideration each have an amount of charge proportional to the light intensity on their relevant pixel. Charge cannot move from these regions because of the potential barrier set up by the electrodes on either side. At time $t=t_2$, the potential on ϕ_2 is made positive forming a well under the ϕ_2 electrodes. Charge will then flow from the ϕ_1 wells to the ϕ_2 wells. At time $t=t_3$, the potential on the ϕ_1 electrodes has been reduced so that the remaining charge in the ϕ_1 wells will be pushed into the ϕ_2 wells. By $t=t_4$ all the charge which

Figure 4.3 Potential wells beneath electrodes $\phi_1 \rightarrow \phi_4$ as a function of time

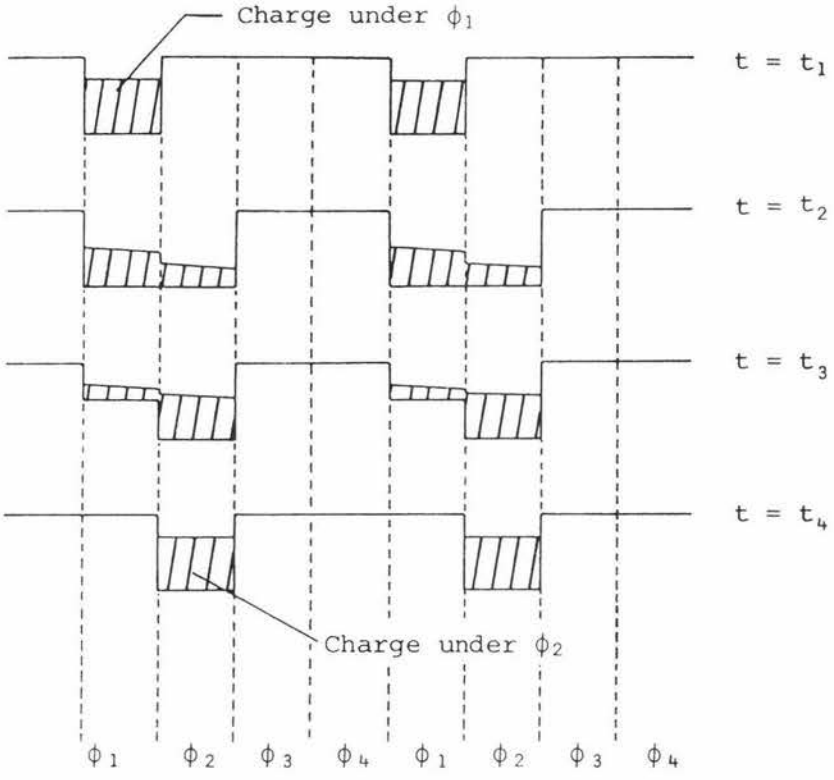

Figure 4.4 Multiphase clock waveforms used to generate the above charge transfer

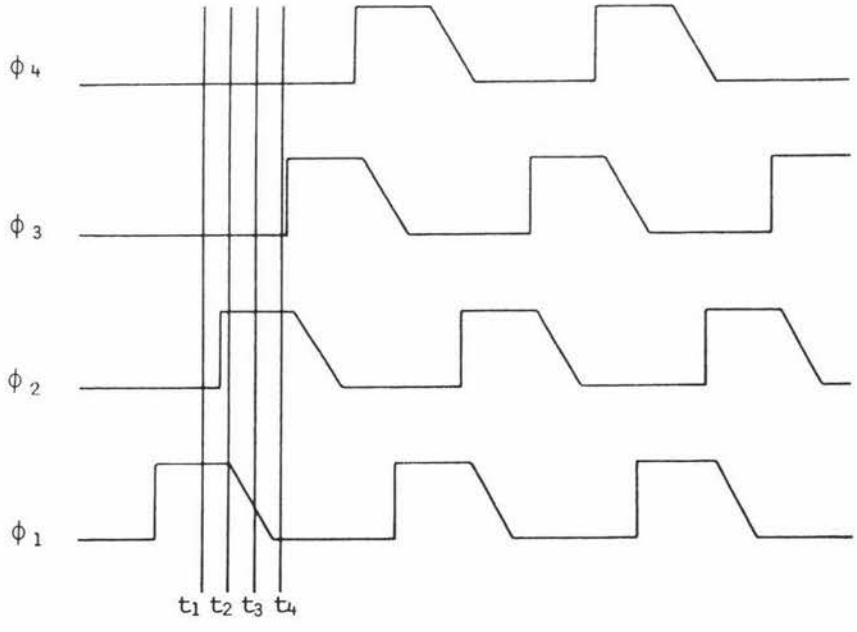

was under the ϕ_1 electrodes will have been transferred to the ϕ_2 electrodes. This process is repeated, transferring charge to ϕ_3 and ϕ_4 and then onto the next ϕ_1 electrode. When each packet of charge reaches the end of the register it is passed on to a charge detection circuit which converts it to a proportional voltage.

One particular aspect of the array which has not been considered is its antiblooming facility. If the charge accumulated on any photodiode exceeds a saturation value, the excess is shunted to an external circuit to avoid overload. This action may also be externally controlled so that the integration time can be made shorter than the readout time. (This facility would be useful at high light levels where the integration time must be kept very short).

For a more detailed description of the array and charge-coupled devices in general the reader is referred to Barbe's paper {ref 4.2} and the various Reticon specification sheets {ref 4.3 and 4.4}.

4.2 The Array Interface and Controlling Circuitry

To simplify construction interface boards were obtained with the array. The following discussion summarizes the description of the interface circuitry as given in the Reticon instruction sheets {ref 4.4}.

All timing in the array interface system (see figure 4.5) is controlled by a master clock which is derived from a 2MHz crystal oscillator external to the array circuitry . This drives a divide by 256 circuit to produce a stable 7812.5Hz square wave. This waveform is then fed to a group of flip-flops which produce the required 4 phase clock pulses $\phi_1 \rightarrow \phi_4$ which have a period of 512μs. (Four times that of the master clock). These clock pulses are then passed through various shaping circuits which delay their fall time for optimum charge transfer.

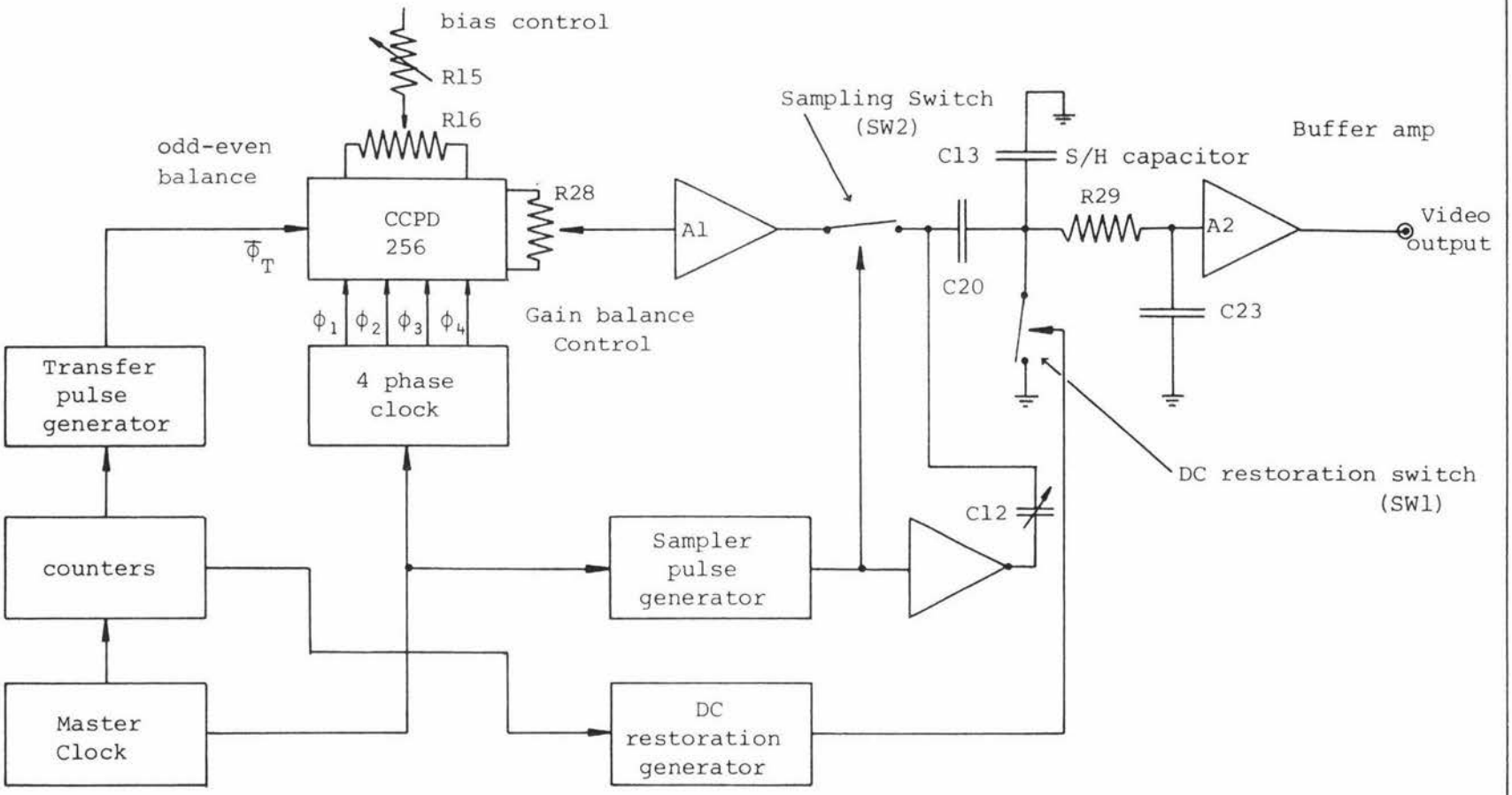

Figure 4.5 Simplified schematic of the array interface system

The master clock also feeds a divide by n counter which, after a predetermined period (called the integration time), produces a transfer pulse which initiates data exchange from the photodiodes to the video output. During this data transfer the charge on the photodiodes is removed by applying a reset pulse to the array. Once reset, the pixels are again ready to provide intensity information after the elapsed integration period. Because of this dual action (i.e. outputting old data while new information is being assimilated) there is little dead time between each scan.

Correct biasing of the array is obtained by adjusting R15 and R16. The odd and even outputs from the array are balanced and summed by R28 and preamp A1. Because the registers deliver their charge packets alternately the output from A1 will be a stepwise continuous video signal.

The video signal from each output is alternately set to a high level of 6V and then released to carry the video information at a lower level of around 2.5V. After combination and buffering the maximum video signal has an amplitude of approximately 2.5 volts peak-to-peak, riding on a (dark) bias level of approximately 4.5 volts.

The remaining analogue circuitry conditions this signal so that output is grounded for dark conditions and has a value of up to 2.4 volts when illuminated. This is achieved in the following manner. During data transfer from the pixels to the shift registers the D.C. restoration switch (SW1) is kept closed so that the voltage across C20 is 4.5V (DC bias level). When data is available from A1 SW1 is opened leaving C20 connected to A2 with 4.5V still across it. As each pixel output becomes available it is sampled by SW2 and stored on C13. C20's effect is to subtract 4.5V from the voltage across C13 leaving the video data to be buffered by A2.

R29 and C23 form a simple RC low-pass filter to minimize

residual switching spikes, and C12 is adjusted to minimize the spikes produced as SW2 is opened and closed. The resultant video output, as well as the odd and even outputs produced by the array, are pictured in figure 4.6.

4.3 Array Performance

On obtaining the array and interface boards it was found that the array was partially defective as one half of the odd pixels did not produce any output.

Since time was not available to go through the necessary channels to obtain a replacement it was decided to use the array as is, but to ignore the odd video output. This was achieved by disconnecting the odd video output from R28 and connecting a dummy resistance in its place. With this done, the resultant data was made up of 128 pulses, corresponding to the output of 128 pixels spaced at 32μm intervals. As long as the structure of the speckle pattern being studied did not have too high a spatial frequency the data thereby obtained would still be useful.

Because half the data was no longer available the output waveform (as illustrated in figure 4.7) was different. It was found, by trial and error, that the video signal had minimum amounts of non-uniformity with the dark level adjusted to $\sim$ - 0.5V and the saturated level to $\sim$ + 2.5V. Actual voltage values were not found to be particularly stable being subject to thermal drift, so that compensatory measures had to be taken when analysing the data.

Because only 128 pixels were active, results obtained from one scan did not always contain enough sample points to produce an accurate picture of the various statistical parameters used in analysing speckle patterns. To overcome this problem a number of scans were made over various parts of the speckle pattern and stored for later analysis. In this way statistical results could be obtained which

Figure 4.6 Ideal outputs from array circuits

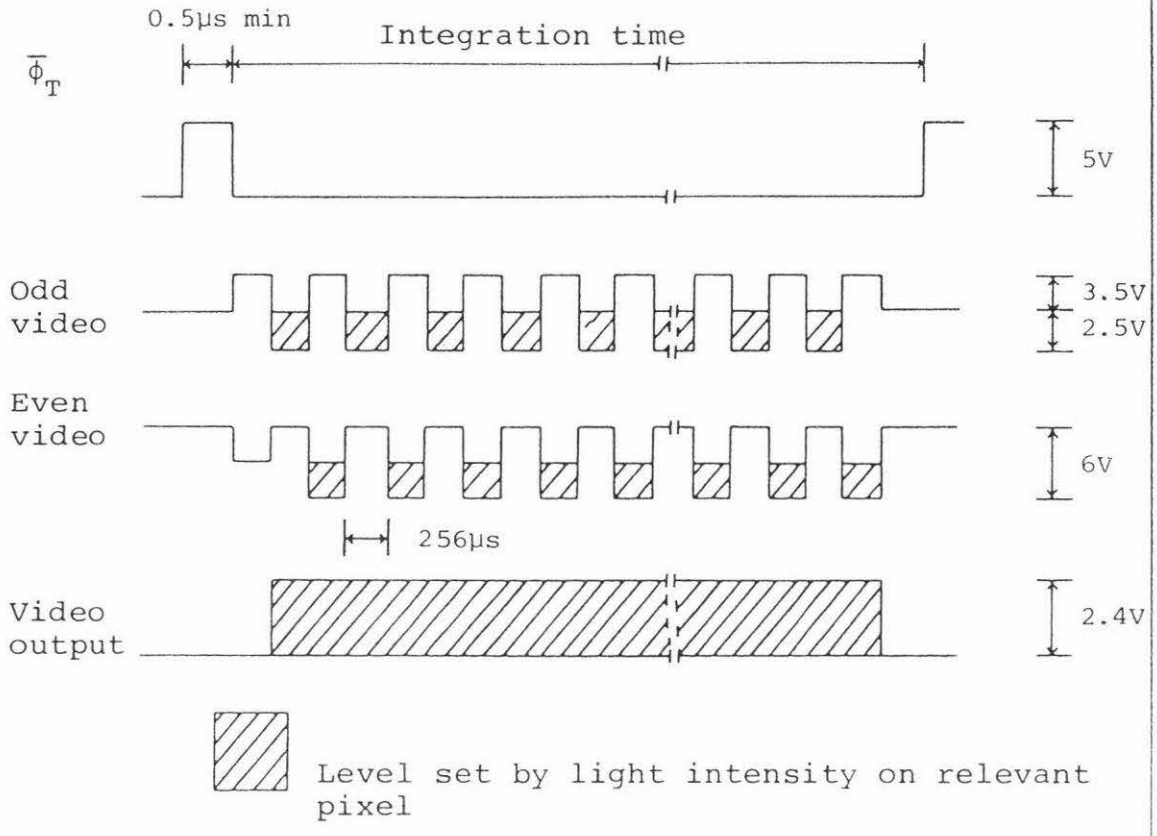

Figure 4.7 Actual outputs obtained after discarding odd video

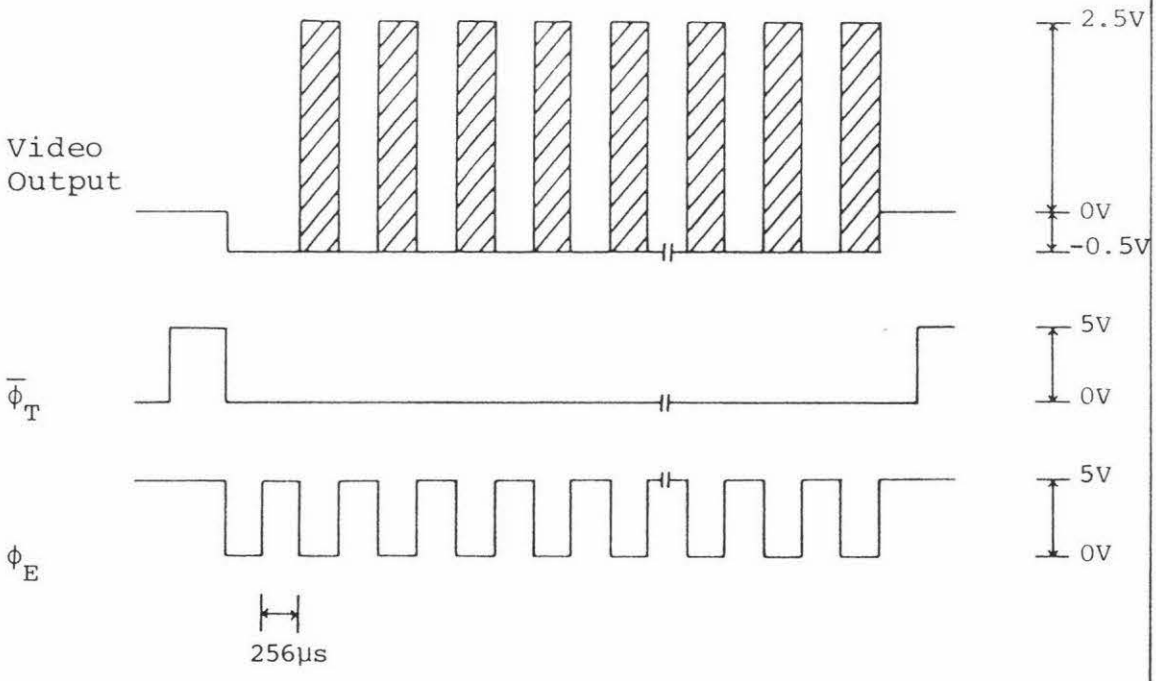

appeared to have been produced by a detector with many thousands of pixels.

Once adjusted, the array and interface circuit boards were mounted in a perspex container (size 161 x 120 x 44mm) and connected, via an 8 core ribbon cable, to the controlling computer to be described in the next chapter. Checks were then made of the array's response to various light inputs. Figure 4.8 pictures the array mounted in its container and itemises the input-output lines which connect it to the computer.

Since measurements of the array characteristics required the microprocessor, results from these tests are not given until after the next chapter. We can however list the manufacturer's specifications for the array so that a comparison can be made when these results are presented.

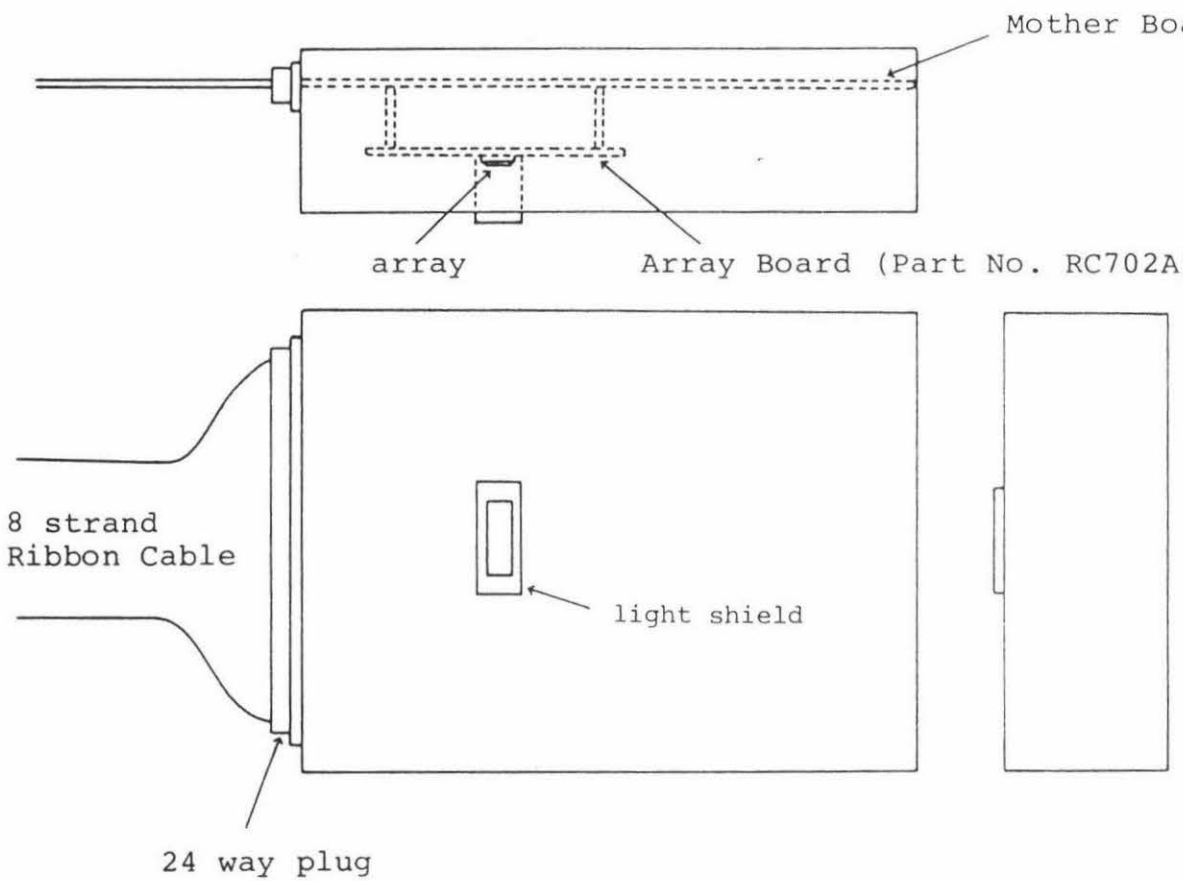

Input and Output lines to the array

Colour	Function
Purple	+15V at 150mA
Blue	0V
Green	-15V at 70mA
Yellow	+5V at 600mA
Orange	ϕ_E (Even video clock)
Red	Master Clock input
Brown	ϕ_T (Scan start pulse)
Black	Video output

Scale 1:2

Figure 4.8 Array and driver board assembly

Table 4.1 Manufacturer's specifications for CCPD 256 array

Parameter (Symbol)	Typical Value	Units	Notes
Dynamic Range (DR)	500	-	1
Spectral Response Limits	0.2→1.1	μm	-
Average Dark Signal (V_{dark})	10	mV	2
Dark Signal Non-Uniformity	10	mV	2
Responsivity (R)	2	$V/\mu Jcm^{-2}$	3
Photoresponse Non-Uniformity	±7	%	3,4
Saturated Output Voltage (V_{sat})	1	V	-
Peak-to-Peak Noise (N_{pp})	2	mV	5
Power Dissipation (P)	70	mW	-

Notes

1. Dynamic range is referred to peak-to-peak noise. It is approximately 5 times higher when referred to r.m.s. noise.

2. At $20^{o}C$ with 30 msec integration time (integration time for present set up is 256μs x 256 = 65.536msec).

3. Light source is a $2870^{o}K$ tungsten lamp.

4. Measured with uniform illumination at 50% of saturation.

5. Peak-to-peak noise is approximately 5 times rms noise.

5. The Microcomputer

To be of any practical use the intensity data obtained by the linear array must be able to be stored and manipulated quickly and accurately. The obvious candidate for such a task is some form of computer.

Fortunately, a COSMAC 1802-based microcomputer, which had been built by the author some years earlier, was available, and for reasons of cost and time available it was decided to use this to do most of the data manipulation, rather than build a faster and more powerful processor from scratch.

The original device was fairly limited having only 256 bytes of memory and no faculty for long term storage of programs or data. So the computer could be used for the desired purpose the following additions were made to improve its capabilities.

i) 512 bytes of permanent memory which held a simple hex monitor and a routine for reading and writing programs on cassette tape.

ii) A cassette interface for use with the routine mentioned in (i).

iii) 3 kilobytes of random access memory to hold data from the array and provide space for the necessary manipulation programs.

iv) An 8 bit analogue-to-digital converter to convert the analogue data produced by the array into a form compatible with the computer.

v) An 8 bit digital-to-analogue converter so that intensity data in the computer could be displayed in graphic form on an oscilloscope.

In addition the original unit had an 8 digit seven segment display and a hexadecimal keyboard.

A block diagram showing these major components is given in figure 5.1.

5.1 The Analogue-to-Digital Converter

The subsystem of special interest is the analogue-to-digital converter since any design defects in this part of the unit could lead to erroneous results. With reference to figures 5.2 and 5.3 we see that the system is based on a National Semiconductor ADC0800P 8 bit A/D Converter. The manufacturer's specifications for this device are listed on page 71.

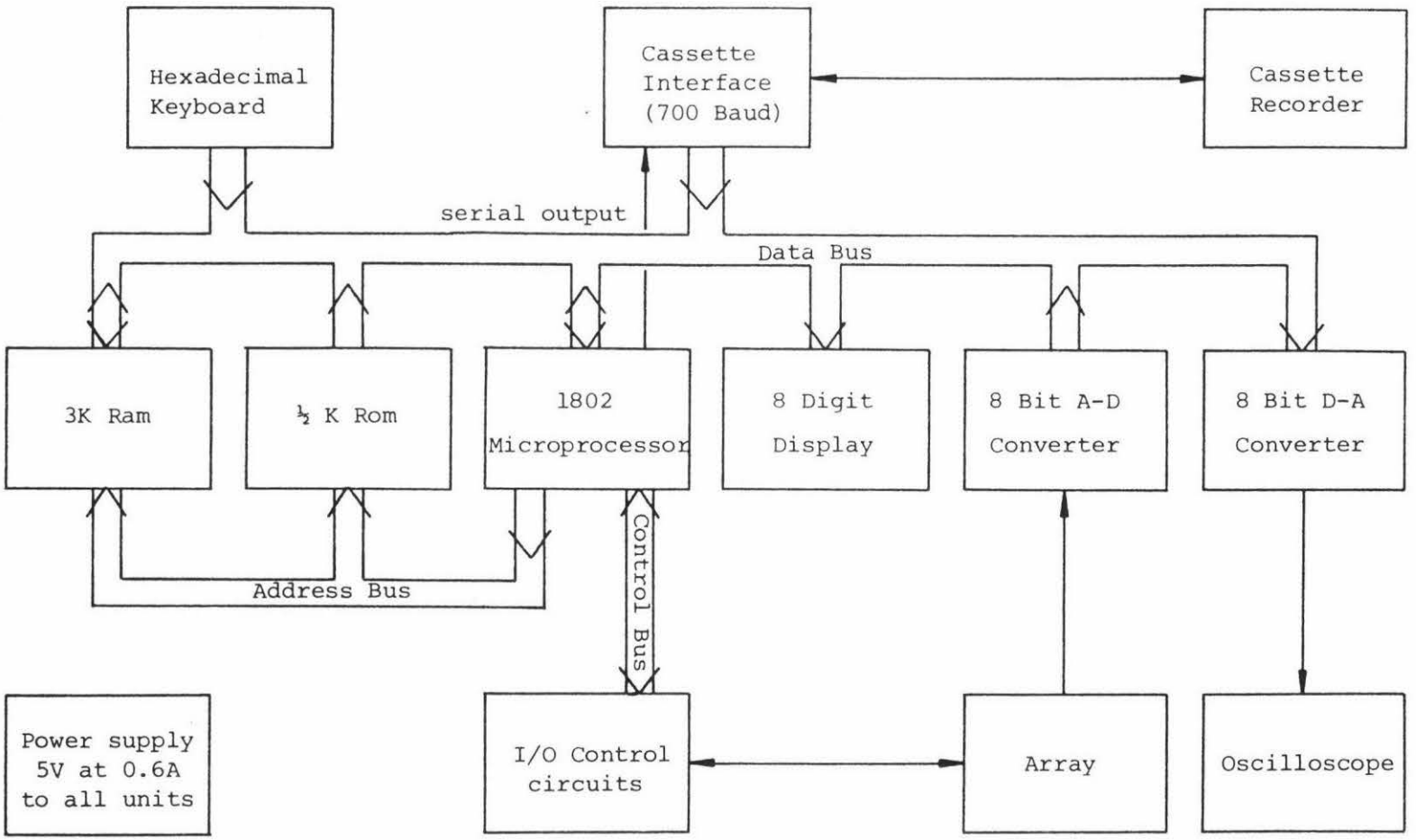

Figure 5.1 Block diagram of microcomputer & peripherals

Figure 5.2 Simplified schematic of A/D converter

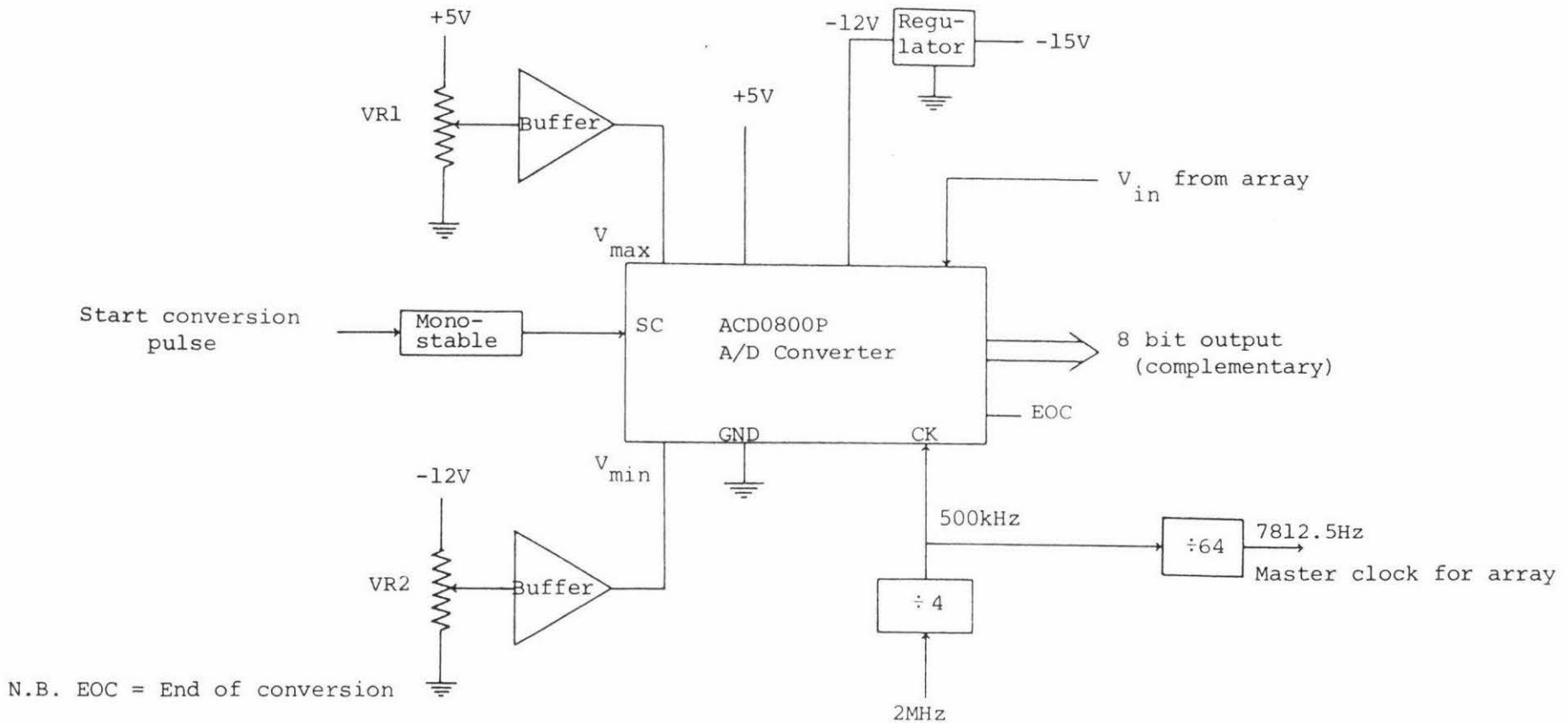

N.B. EOC = End of conversion

$V_{ref} = V_{max} - V_{min}$

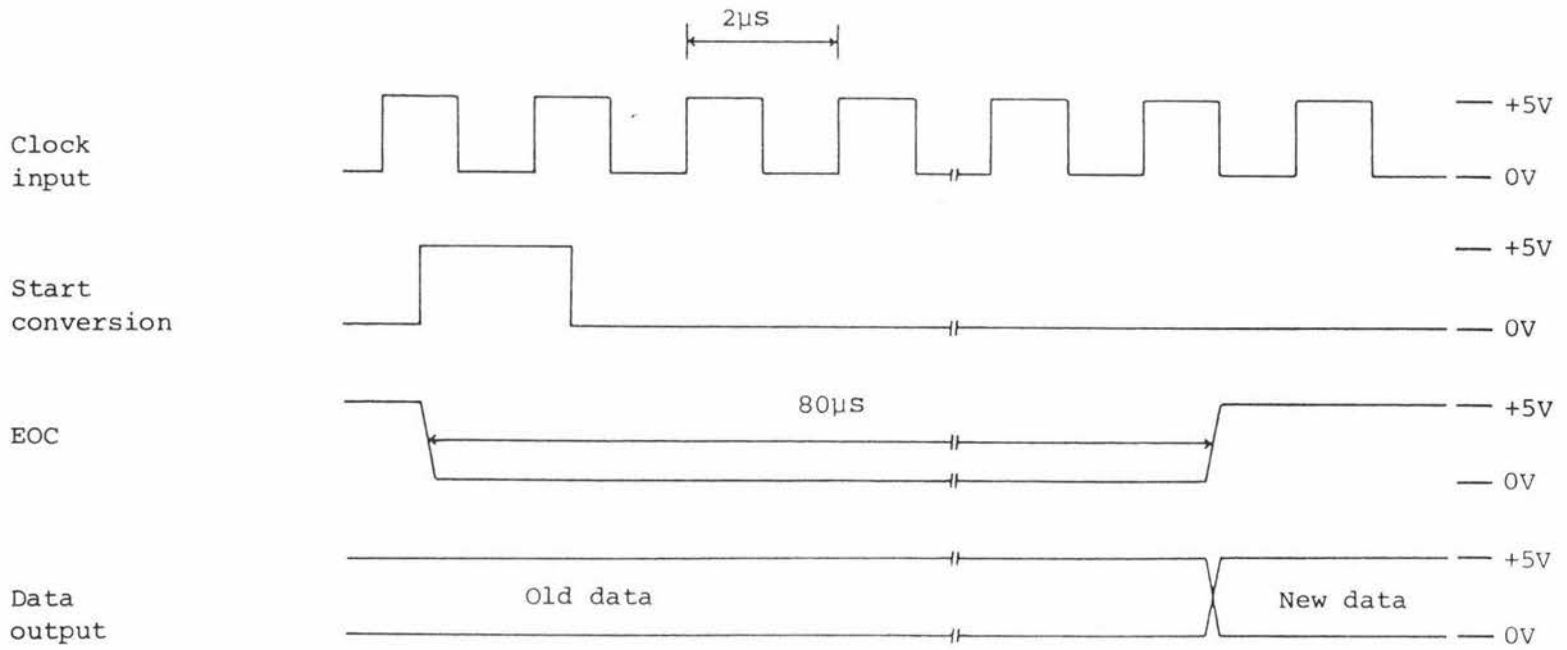

Figure 5.3 Timing diagram for A/D converter

Table 5.1 Specifications for the ADC0800P A/D converter

Parameter	Typical Value	Units	Notes
Power Supply Voltage	5,-12,Gnd	Volts	-
Power Supply Current	15	mA	-
Resolution	8	bits	-
Non-Linearity	±1	L.S.B.	1
Zero Error	±2	L.S.B.	2
Full Scale Error	±2	L.S.B.	3
Clocking Frequency	50 to 800	kHz	-
Conversion Speed	40	Clock Periods	-
Start Conversion Pulse Length	1 to 3½	Clock Periods	-
Input Voltage Range	from -5→+5 up to 0→10	Volts	4

Notes (LSB = Least Significant Bit)

1. Non-linearity is the departure of the device response from an ideal linear transfer curve.

2. Zero error is the departure of the actual input voltage from the ideal input voltage for a zero output count. (Expressed in terms of digital bits).

3. Full scale error is the departure of the actual input voltage from the ideal input voltage for full scale output count. (Expressed in terms of digital bits).

4. This range is variable and its limits are dependent on V_{max} and V_{min} (see figure 5.2).

On receiving a start conversion pulse of the appropriate length from the microprocessor this device will, after 40 clock periods, produce, by means of a successive approximation technique, a complemented 8 bit output proportional to the input voltage. (With the clock rate as indicated this corresponds to an 80μs conversion time).

By adjusting VR1 and VR2 the range of input voltages over which the device responds can be varied. To be compatible with the array output this range was set from approximately -0.35 to 2.45 volts. The exact value of these limits was not particularly important as long as they contained the maximum and minimum values produced by the array. Subsequent processing referenced all measurements to the dark video signal and thereby restored the zero level.

Measurements of complemented output count as a function of input voltage were made. The results obtained are plotted in figure 5.4. A least squares fit for this graph gave

$$\text{Count} = (91.4 \pm 0.2) \times V_{in} + (32 \pm 1). \qquad (5.1)$$

From this we can obtain the deviation of the actual curve from the best fit line (i.e. the non-linearity). This turns out to have a standard deviation of 0.75, within the ± 1 LSB specified by the manufacturer.

It should be noted that this unit was the third to be built, the first two being designed along quite different lines. The first used a simple ramp type system while the second produced a pulse which had a length proportional to the input voltage. Block diagrams of both these devices are shown in figure 5.5. Both circuits were eventually discarded in favour of the third option due to their relative complexity,

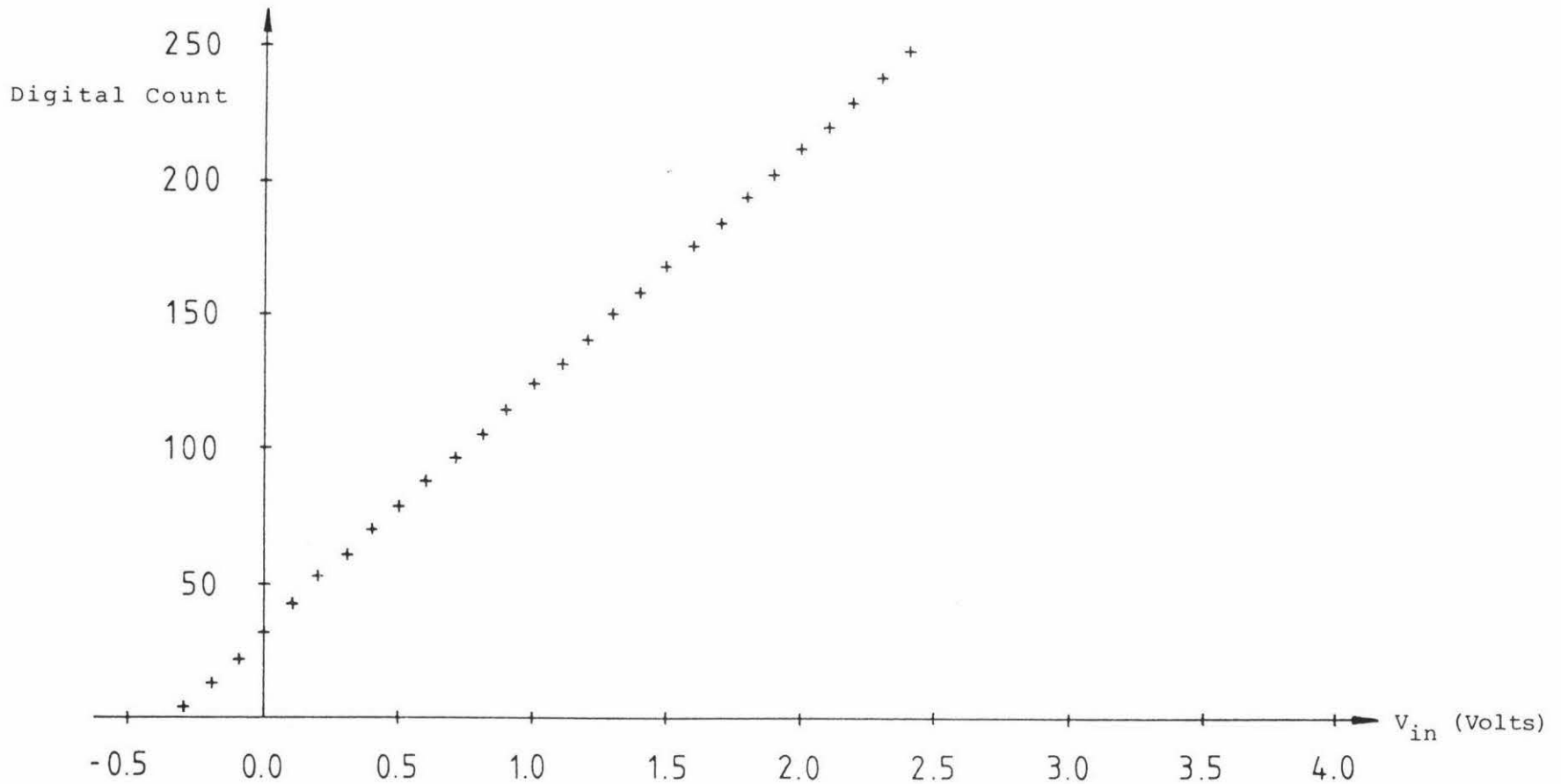

Figure 5.4 Output count vs. input voltage for the A-D converter

Figure 5.5 Alternative A/D converters

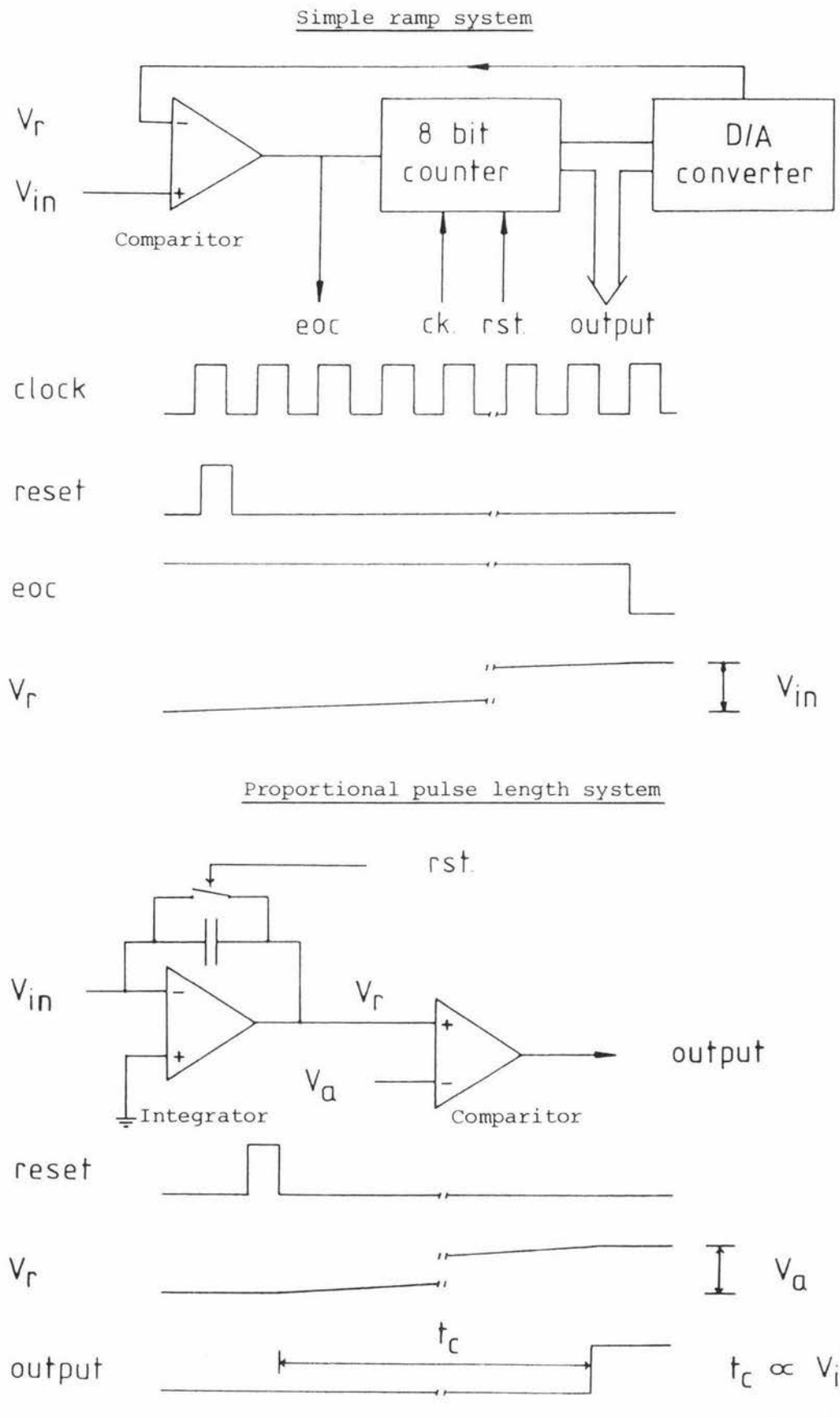

slow conversion speed and non-linearity.

Once the data from the array had been converted to 8 bit digital form it was then stored in blocks of 128 bytes in the computer's memory to await further manipulation.

5.2 Programming the Microcomputer

A number of programs were written to investigate the situations and results discussed in chapter 2, in particular measurement of surface roughness, surface displacement, the effect of depolarized illumination, and average speckle size. Since the basic instruction set for the 1802 is rather difficult to use when it comes to performing even simple mathematical operations, a 1 kilobyte maths package was written which included a number of useful routines that would make writing of the speckle analysis programs a lot simpler. As software for the 1802 is somewhat limited all these routines had to be written from scratch which, as can be imagined, took quite some time! The resultant routines, most of which were accessed by a one or two byte instruction, are listed in table 5.2. All arithmetic is performed in 3 byte blocks with another byte being used to indicate sign and overflow. This gives a decimal range of $\pm(2^{25}-1)$, adequate for most of the tasks undertaken.

Because all the arithmetic is integer in form certain calculations could not be completed by the computer (determining a standard deviation for example). However it was found that by allowing the computer to perform the bulk of the simple calculations (such as ΣI or ΣI^2) little time was lost by completing the maths on a calculator. A more sophisticated machine, with say a number crunching unit attached, would not have this problem.

Most of the instructions in table 5.2 are self explanatory being modelled on a (simple) programmable calculator.

However, some of them do merit attention.

Instructions 10 and 11 allow (speckle) data to be loaded into the X register, manipulated, and then returned to a previous (or new) storage location specified by the lower two bytes of register A.

Instructions 29 and 30 allow the program to run in machine language when high speed is required. Compared with machine instructions which take 8μs to perform, most of the new routines take between 100 and 1000μs to run. Exceptions to this are the multiply and divide routines and the $X_{Hex} \rightarrow X_{10}$ conversion which take tens of milliseconds. Despite their slow speed these instructions improved program design and readability greatly.

Once completed this package was stored on tape so that it could be quickly reloaded ($\sim$12 seconds) whenever required.

In the next chapter the programs used to load and analyse the laser speckle will be discussed and the experimental results obtained will be presented.

Table 5.2 Routines Developed for Speckle Analysis

General Maths Routines

(1) Go to cd
(2) Go to abcd
(3) Go to cd if X=0
(4) Go to cd if X≠0
(5) Go to cd if X<0
(6) Go to cd if X≤A
(7) Display X
(8) X→A
(9) A→X
(10) M(A)→X
(11) X→M(A)
(12) Constant→X
(13) Keyboard input →X
(14) 0→A
(15) 0→all memories
(16) Y+X→X
(17) Y-X→X
(18) Y×X→Y
(19) Y÷X→X
(20) X→-X
(21) Shift X right n times (i.e. $X \rightarrow X/2^n$)
(22) Shift X left n times (i.e. $X \rightarrow X \times 2^n$)
(23) Do subroutine at abcd
(24) Return from subroutine
(25) Shift stack up 1 X→Y→Z→Q
(26) Shift stack down 1 Q→Z→Y→X
(27) A=A+1
(28) Return from subroutine if X=0
(29) Run a machine code routine
(30) Return from a machine code routine
(31) $X_{Hex} \rightarrow X_{10}$
(32) Display a word

Key

1. abcd signifies an address anywhere in memory.
2. cd on its own indicates that ab is kept constant.
3. X,Y,Z and Q are stack registers
4. 'A' is a general register, (including the stack registers) of which there are 40.

6. Speckle Analysis Programs and Experimental Results

6.1 Data Load Routine

The first program to be developed was one which loaded video data from the array into the computer's memory. Because of the speed at which this had to occur the program was written in machine language and called as a subroutine from the main program when required.

So the program obtained data from the array in the correct sequence it first waited for an end of scan pulse to be detected. When this had arrived the even video clock (ϕ_E) was monitored, and at the beginning of the second low cycle a start conversion pulse was sent to the A/D converter. After an 88μs pause to allow for complete conversion the data was loaded into the computer's accumulator, complemented, and then stored in the appropriate memory location. This process was repeated 128 times until all pixel intensities were stored in memory. Control was then returned to the main program. The total time required for this process was around 65ms.

A pictorial representation of the above discussion may be seen in figures 6.1 and 6.2 which show the timing diagram and flow-chart for data acquisition. As can be seen from figure 6.1 a lower limit is set on the integration time (t_i) by the conversion period (t_c), and the time required to load data into the computer (t_ℓ). If shorter conversion times were required a faster (and therefore more expensive) A/D converter would be needed, and data would have to be loaded directly into the memory, bypassing the microprocessor completely (a technique which was used by Stephens et al. {ref 4.1} in their apparatus). An alternative solution to this problem would be to use the antiblooming control in the manner mentioned in section 4.1 and as described by Reticon {ref 4.3}.

Figure 6.1 Timing diagram for data conversion

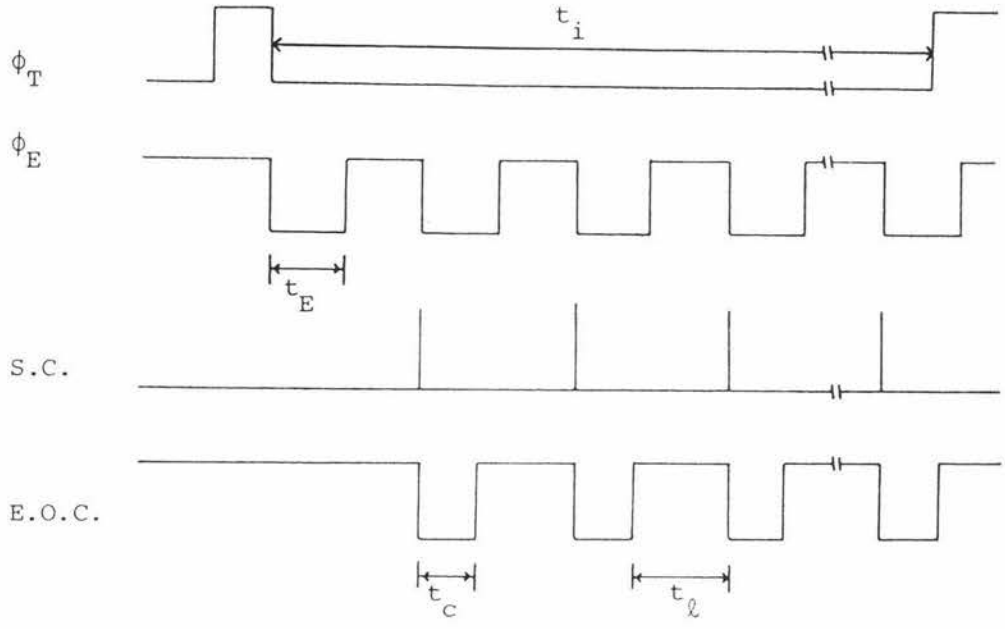

Key

1. ϕ_T = End of scan, or transfer pulse. Produced once every scan before data output.
2. ϕ_E = Even video clock. Keeps in step with video output waveform. Goes low when video output is active.
3. S.C.= Start conversion pulse. Produced by the microprocessor to start the A/D converter.
4. E.O.C= End of conversion waveform. Goes low while conversion is taking place.
5. t_E = period of each pixel transfer. Approximately 256μs for the present arrangement.
6. t_c = Conversion period, 80μs for the present arrangement.
7. t_ℓ = time available for computer to complement and load data = 512-80=432μs.
8. t_i = integration time.

Figure 6.2 'Load Video Data' flow chart

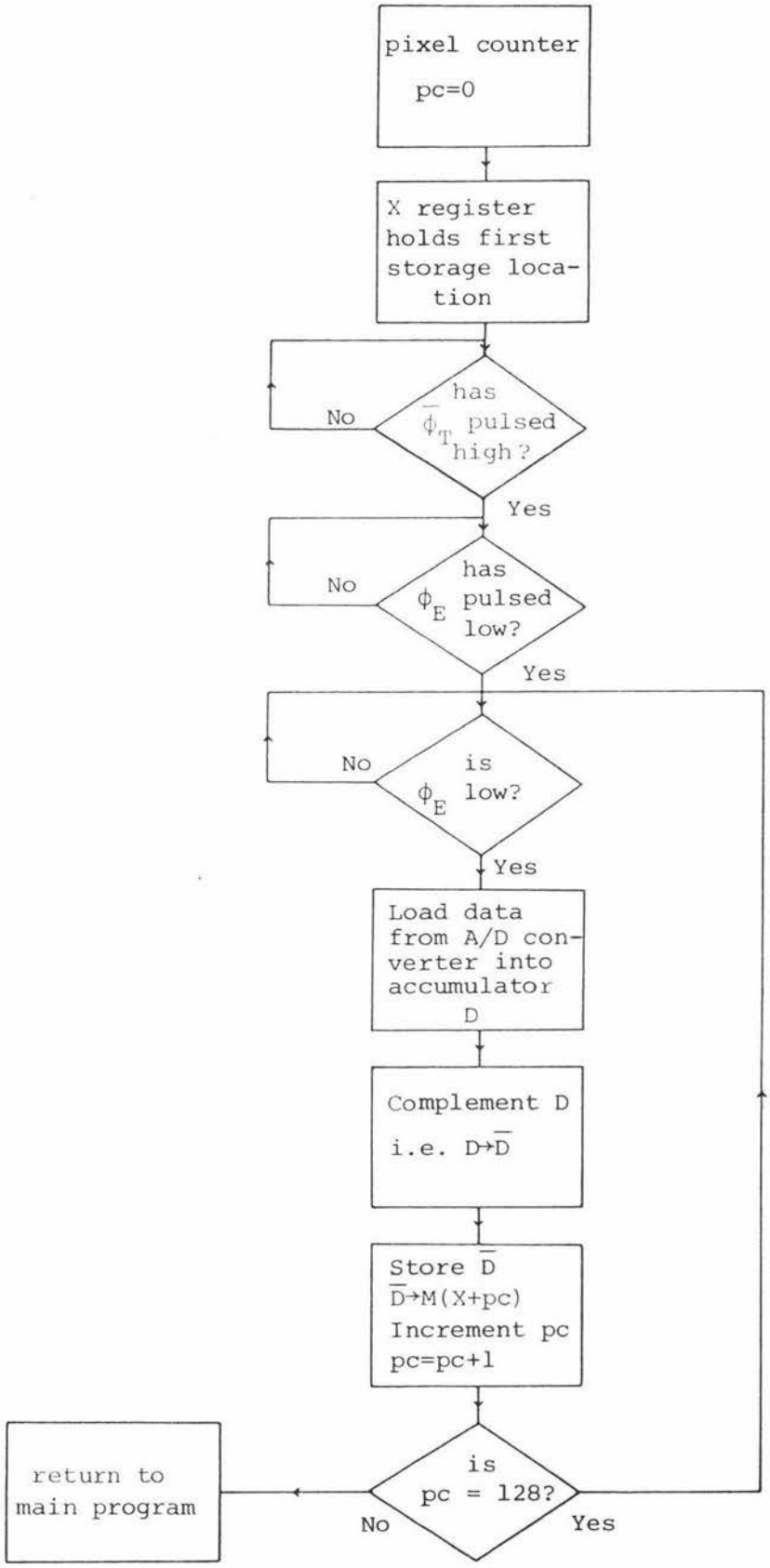

6.2 Intensity Compensation Routine

In section 4.3 it was noted that the output voltage from the array tended to drift slightly with time, especially when it was first switched on. In addition, for many applications, the value of the signal, with respect to the dark level, was quite important and so a reading was made of the intensity in the dark and then subtracted from the illuminated results. This action solved both problems and also had the (desirable) effect of removing the dark signal non-uniformity which was quite large ($\sim$30mV).

In addition to this problem it was observed that the sensitivity of pixels across the array was not uniform and although this non-uniformity was not marked it did cause difficulties with some of the measurements (probability densities in particular). To eliminate this problem a program was written which multiplied each pixel output by a correction factor. The effectiveness of this technique was based on the assumption that each pixel has a linear photometric response. To obtain sufficient accuracy each factor was 2 bytes long, requiring a total of 256 bytes of storage for all correction factors.

A flow chart showing the major steps involved in the above process is pictured in figure 6.3. Note that the first two operations in this routine are simply 'Load Video Data' subroutines as described in figure 6.2. Because it deals with only single byte numbers the third operation is run in machine language to improve program speed. However the fourth and final operation is somewhat more complex and so is implemented using the instructions in table 5.2. Since 128 multiplications have to be made this routine is relatively slow taking around 1.5 seconds to run.

So the reader may obtain some idea of the programming techniques used, a section of this last routine is flow charted in more detail in figure 6.4 along with the partic-

Figure 6.3 Data compensation routines

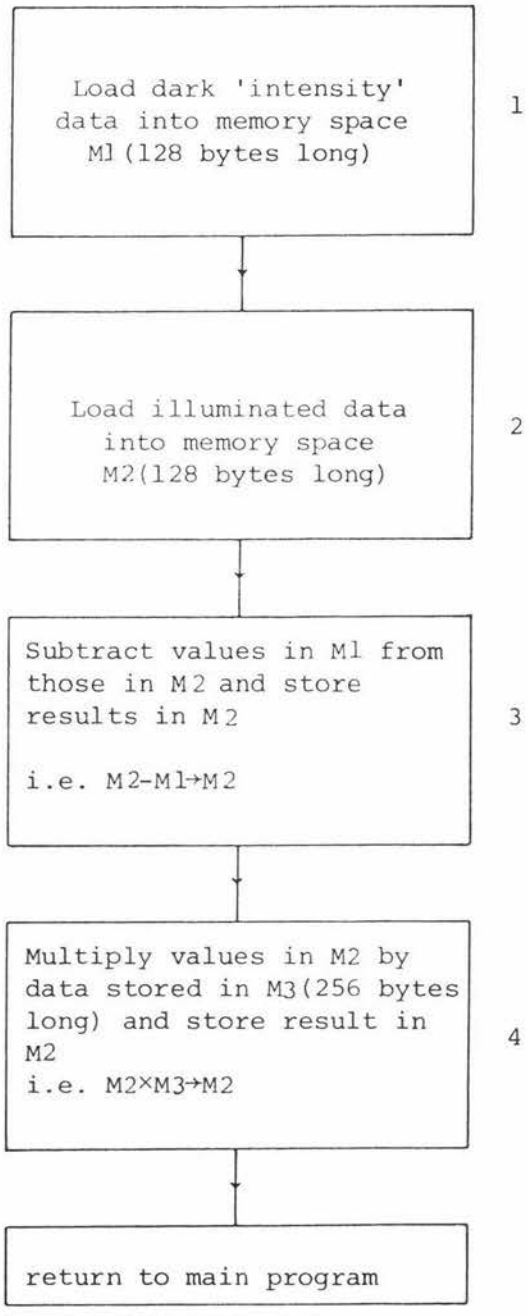

Figure 6.4 Section of compensation routine

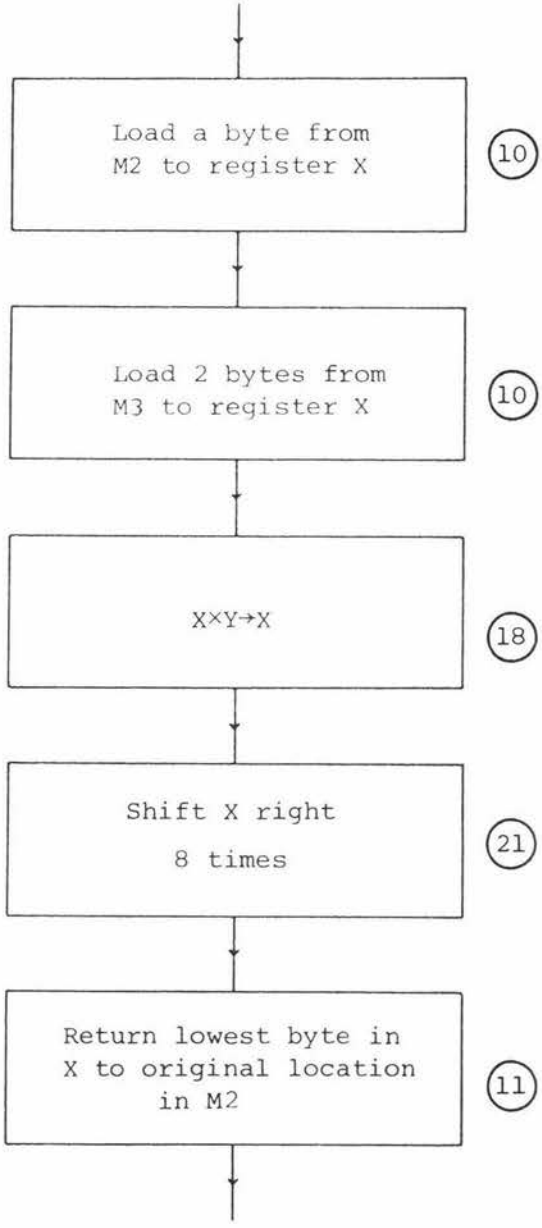

Notes

1. Circled numbers represent the instructions used (with reference to table 5.2).
2. Instruction 10 shifts up the stack before loading from the memory. Hence the first multiplicand is shifted from the X to Y registers in the second instruction.
3. In instructions 10 & 11 we can specify the number of bytes to be handled.
4. Instruction 21 effectively divides X by 256 = 2^8.

ular instructions used to perform each step.

6.3 Array Response Tests

Once the compensation programs had been run, the data in memory M2 was expected to be a fairly accurate measure of the light intensity across the array. To test this a number of experiments were performed. The results obtained from these experiments will now be presented.

i) The response of the array to varying light intensities

Ideally the array should show a linear response to varying light intensities. To test this, the array was set up with the optical arrangement shown in figure 6.5. Light from the laser was spatially filtered and then expanded by a microscope objective until it had a diameter of approximately 3cm. A magnetic stand was then introduced at this point with a piece of paper mounted on it to act as a diffuser. From equation 2.74 we see that this will give a speckle size of approximately 10μm for L = 20cm. Since the pixels are 16μm square this will result in an integrating effect which will tend to smooth out the speckle (i.e. reduce the contrast). To further enhance this effect the paper was moved rapidly during the exposure to produce a practically uniform field of illumination. By changing the distance L the intensity of the light could be varied over a wide range. After the video data had been loaded into the computer the compensation routine previously described was applied. Once completed the mean and standard deviation of this data was then found using the formulae

$$c = \frac{\Sigma c}{n},$$

and

$$\sigma_c = \left(\frac{\Sigma c^2}{n} - \left(\frac{\Sigma c}{n} \right)^2 \right)^{\frac{1}{2}}, \qquad (6.2)$$

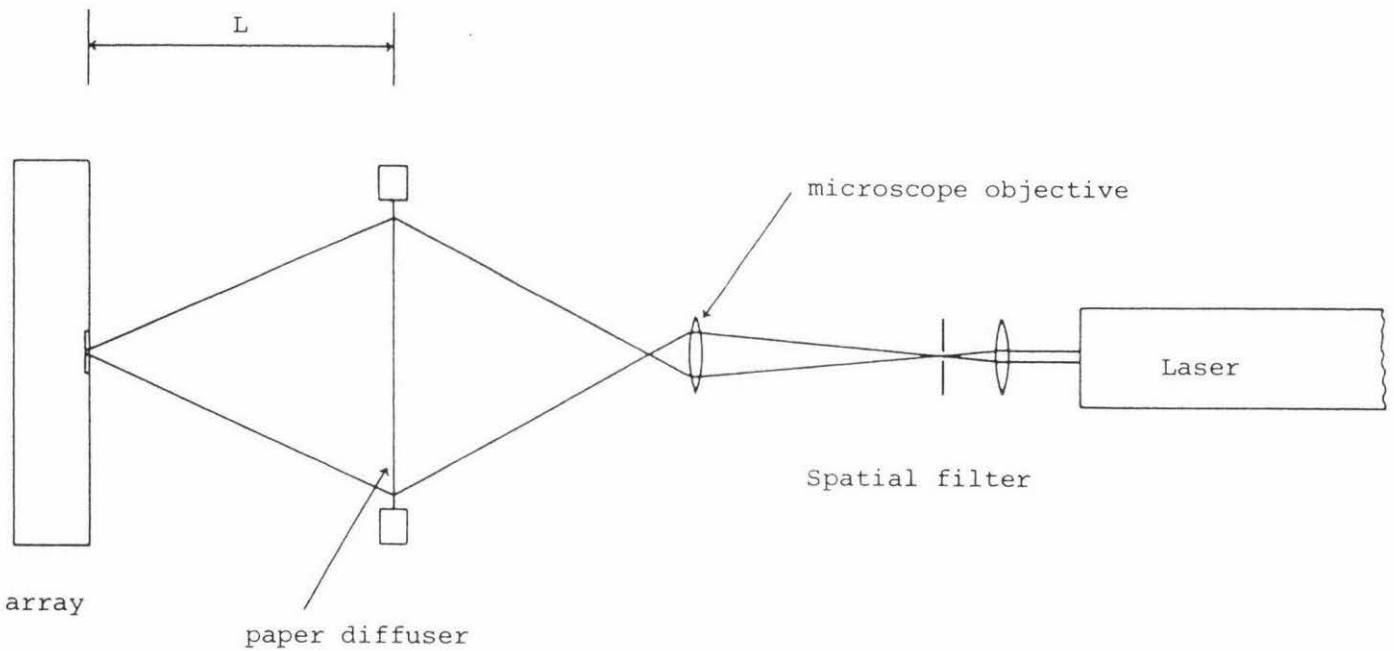

Figure 6.5 Optical arrangement for measuring intensity response

where c is the compensated video data (hopefully proportional to the light intensity) and n = 128, the number of sample points available in each scan.

The results obtained are tabulated below as a function of L^{-2}, which should be proportional to the light intensity.

Table 6.1 Mean count, <c>, as a function of L^{-2}

L(mm) ± 1mm	L^{-2} (m^{-2})	$\langle c \rangle \pm \sigma_c$
50	400.0	194.0 ± 0.5
60	277.8	139.0
80	156.3	75.0
100	100.0	49.0
120	69.4	34.0
140	51.0	25.0
160	39.1	20.0
180	30.9	16.0
200	25.0	13.0
220	20.7	11.0
240	17.4	9.0
260	14.8	8.0
280	12.8	7.0

As the standard deviation σ_c was found to be fairly constant it seems reasonable to assume that any residual non-uniformity in c was due to electronic noise rather than variations in pixel sensitivity. This indicates that the compensating routines have functioned correctly.

The obviously linear relationship which exists between L^{-2} and <c> (as seen in figure 6.6) indicates that the compensated video data is directly proportional to the light intensity on the array. Although simple this result is most important as it allows the compensated video data to be used as a direct measure of intensity, something which is necessary if the theory in chapter 2 is to be investigated.

Figure 6.6 Mean count vs. L^{-2}

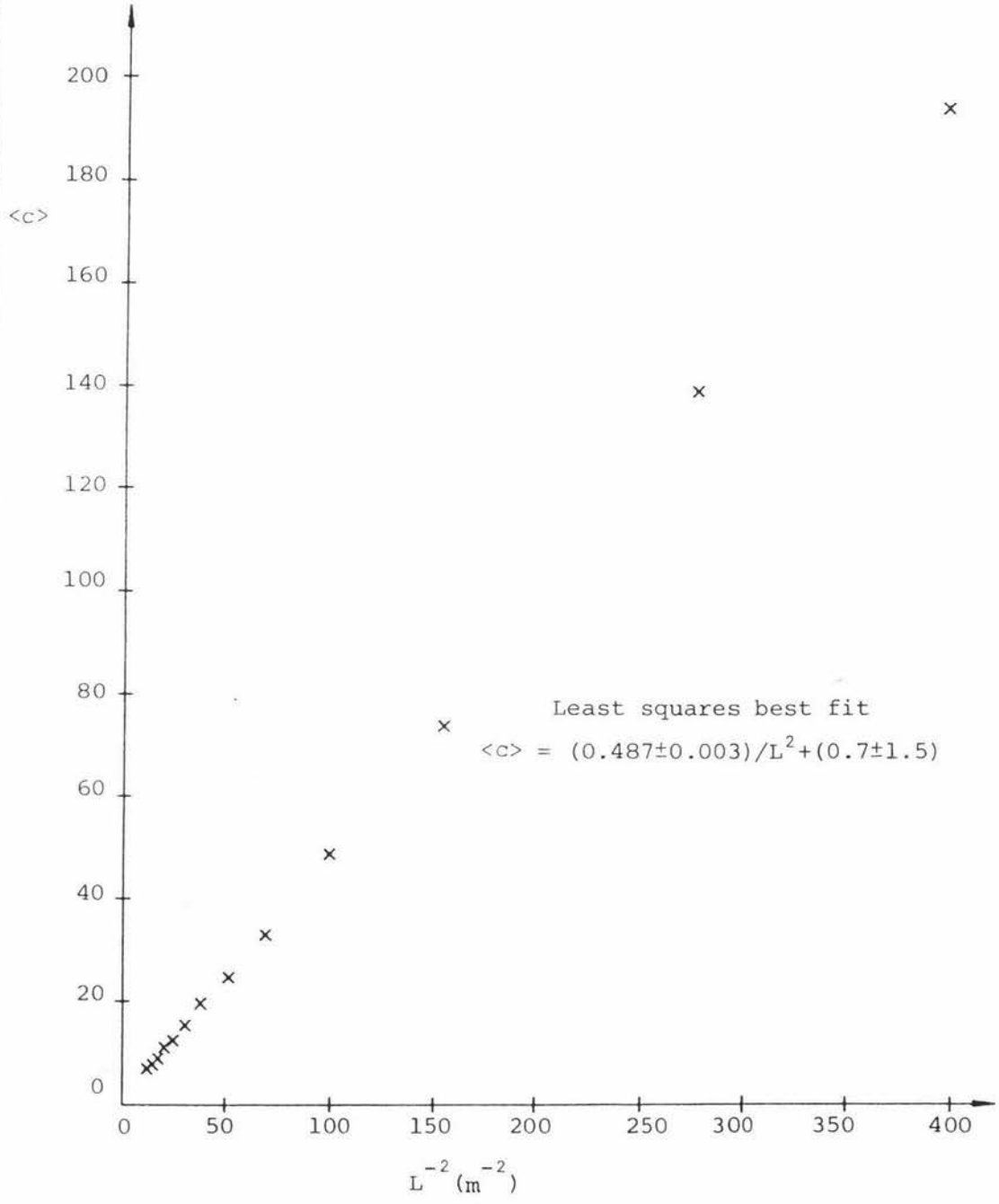

ii) Non-uniformity as a function of wavelength

When the first compensation programs were written the correction factors were obtained using a diffuse white light source. It was soon discovered that when this routine was used on data obtained from a laser source (such as in figure 6.5) the video data was no longer uniform. It was suspected that this was caused by a difference in the spectral response of each photodiode. To check this possibility non-compensated scans (still zero-corrected) were made for various light sources and from these, mean and standard deviations were calculated. The results for the four light sources considered are pictured in figures 6.7 and 6.8 and show quite marked differences from one another. (These graphs have been made by averaging the results over every four consecutive pixels). In particular the yellow helium source shows an especially large amount of non-uniformity. The mean and standard deviation for each of these results are listed below.

Table 6.2 Array non-uniformity for various light sources

Source	Predominant Colour	Mean	Standard Deviation	Non-uniformity
Cadmium	blue	130.2	3.4	± 2.6%
Mercury	green	137.1	2.9	± 2.1%
Helium	yellow	107.8	12.4	±11.5%
Laser	red	136.6	3.3	± 2.4%

where non-uniformity is given by

$$\text{Non-uniformity} = \pm \frac{\text{Standard Deviation of intensity}}{\text{Mean intensity}} \times 100. \qquad (6.3)$$

The high non-uniformity produced by the helium source was also seen in white light, thus accounting for the discrep-

Figure 6.7 Intensity profiles as measured by the array (data is uncompensated)

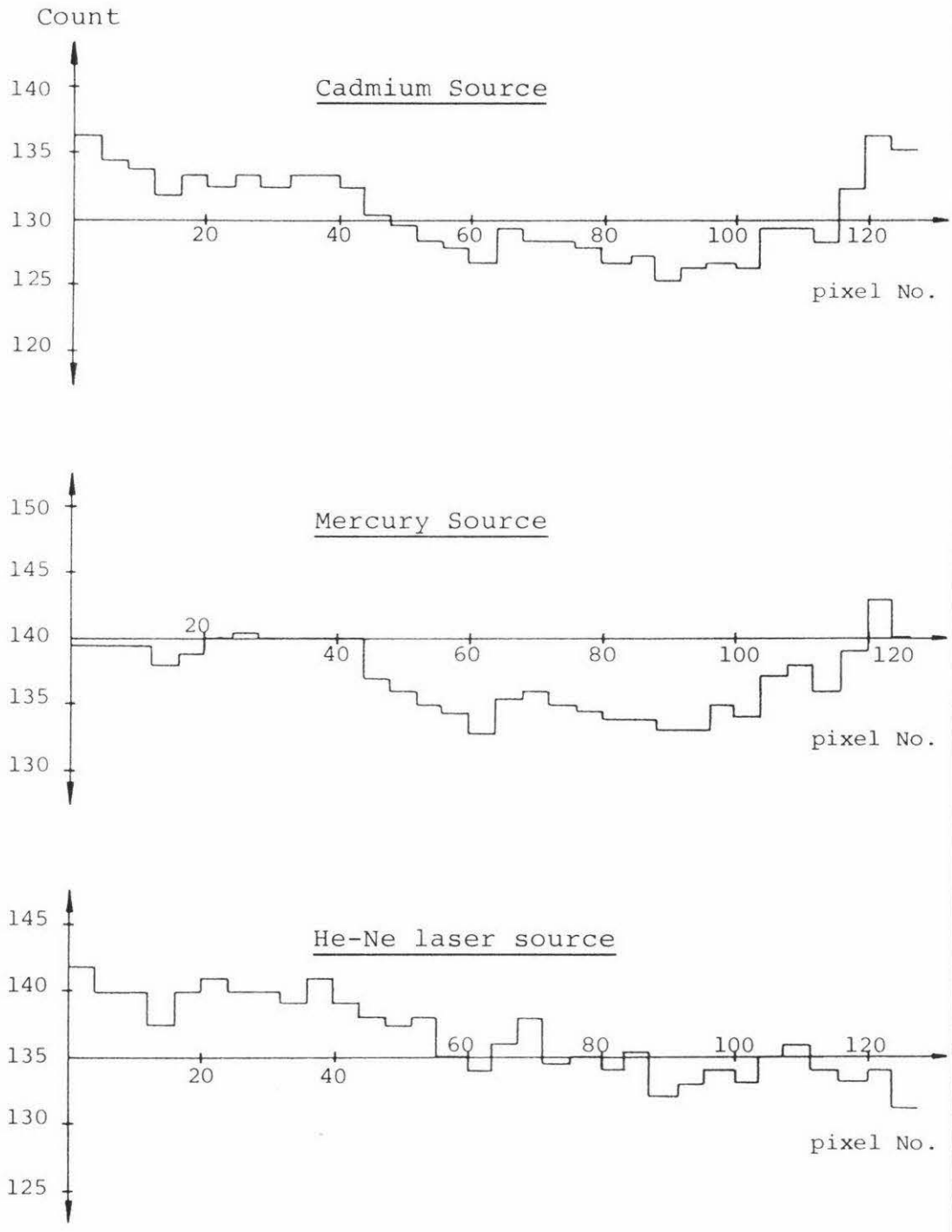

Figure 6.8 Intensity profile as measured by the array (data is uncompensated)

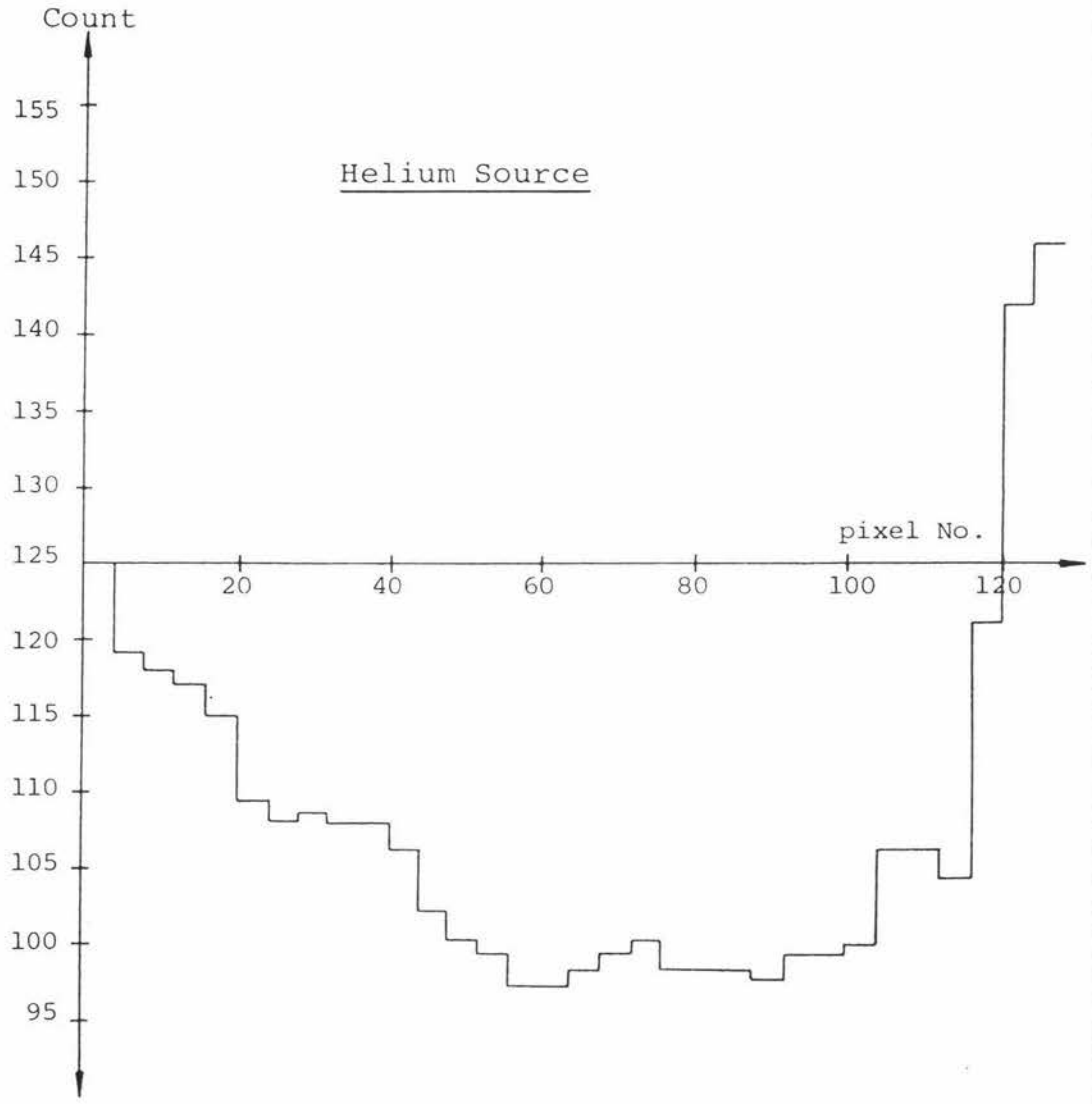

ancies obtained earlier when the laser was used.

Apart from the helium source all other lights produced a non-uniformity within the expected limits of ± 7%. The response of the pixels to the helium source was rather unexpected as the manufacturer's specified response indicated that maximum sensitivity occurs around 800nm, well into the infrared. Large variations in response should therefore be more likely with the red laser source.

iii) Array Noise

In any experiment where data is to be collected noise will be present. If this data is to be digitized it is pointless to use an A/D converter with a resolution greater than the signal-to-noise ratio of the transducer. The manufacturer's specifications indicate a S/N ratio for the array of approximately 500 for a saturated output of one volt. This figure would seem to indicate that an 8 bit A/D converter producing 256 grey levels would be sufficient. Any more resolution would produce little extra useful information (the next available level of resolution is a 10 bit A/D converter which has 1024 grey levels).

To check the above specification we need only look at figure 6.6 which shows the intensity response of the array. From the least squares best fit we see that when the intensity is zero (i.e. $L^2 \rightarrow \infty$) we will have a mean output of 0.7 ± 1.5 counts. A value of 0.7 gives a S/N ratio of 256/0.7 ≃ 370 an acceptable result when one considers the large uncertainty, and the fact that this figure also depends on noise produced by sources other than the array.

An alternative method of determining array noise will be considered later in the chapter.

6.4 Probability Distribution of a Speckle Pattern

Now it has been established that the array produces an output with predictable response and low noise we can use it to make measurements of speckle statistics.

Figure 6.9 shows a typical speckle intensity profile obtained using the apparatus in figure 3.11 and the compensation programs previously discussed. To obtain information concerning the intensity distribution for such a pattern we need only count the number of pixels at each level of intensity. Unfortunately because of the small number of sample points (128) and the large intensity range (256 levels) this will generally lead to a rather nondescript distribution which could represent practically anything. A significant improvement may be obtained by counting the number of pixels with intensities between predefined limits. An example of this is given in figure 6.10 using the intensity data from figure 6.9.

Further enhancement of this result may be obtained by looking at a large number of different speckle patterns, obtained by moving the object slightly, and then determining the intensity distribution for the total number. In this way the size of the array can be effectively increased many times. It was this technique which was finally used to obtain all measurements of probability density and surface roughness.

6.5 Probability Density of a Fully Developed Speckle Pattern

To investigate the fully developed speckle pattern the apparatus in figure 6.11 was used. Light from a polarized 80mW laser was filtered and attenuated before being shone onto the translating stage described in chapter 3. The array was positioned so that the average speckle size was around 390μm, large enough for the speckle to be recorded

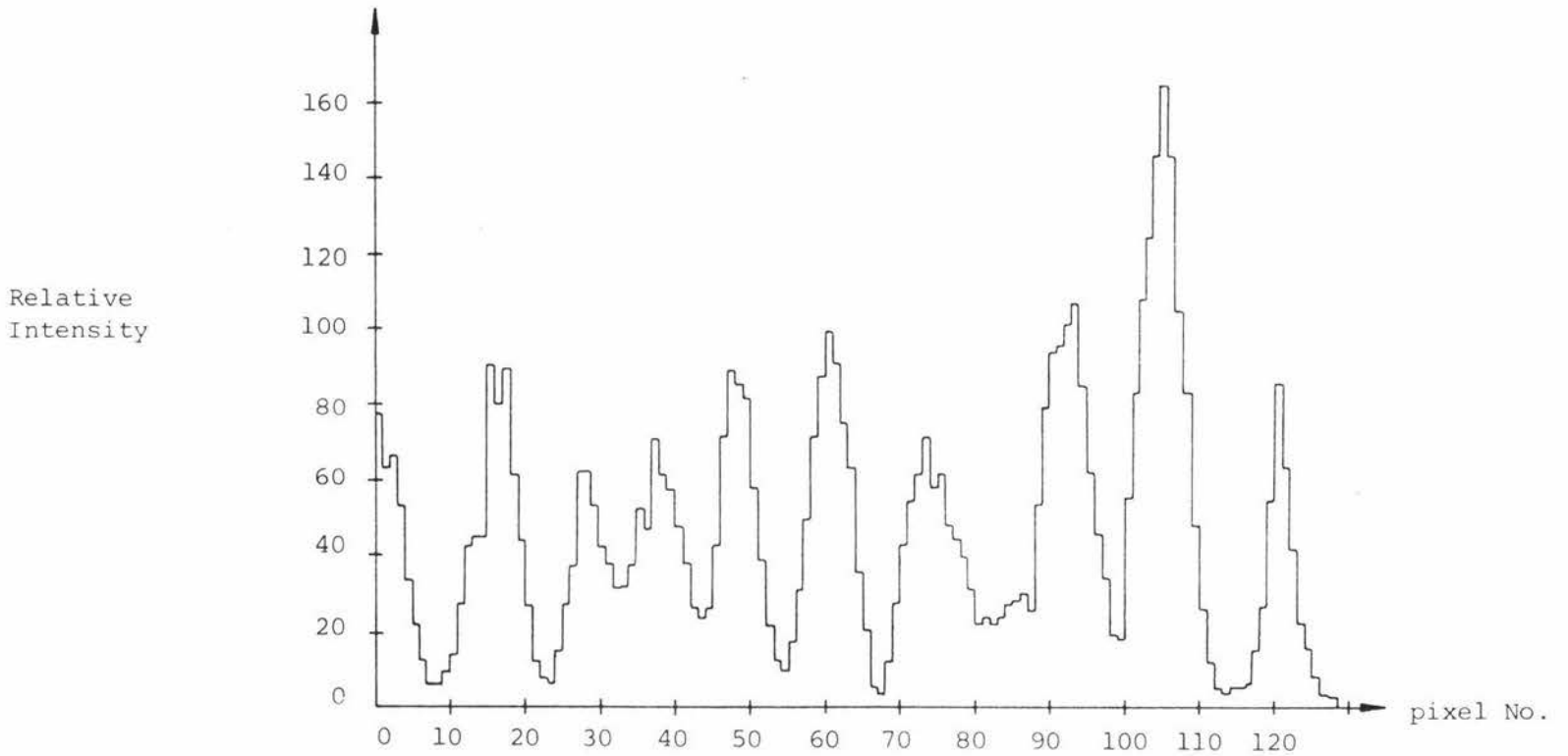

Figure 6.9 Speckle intensity profile

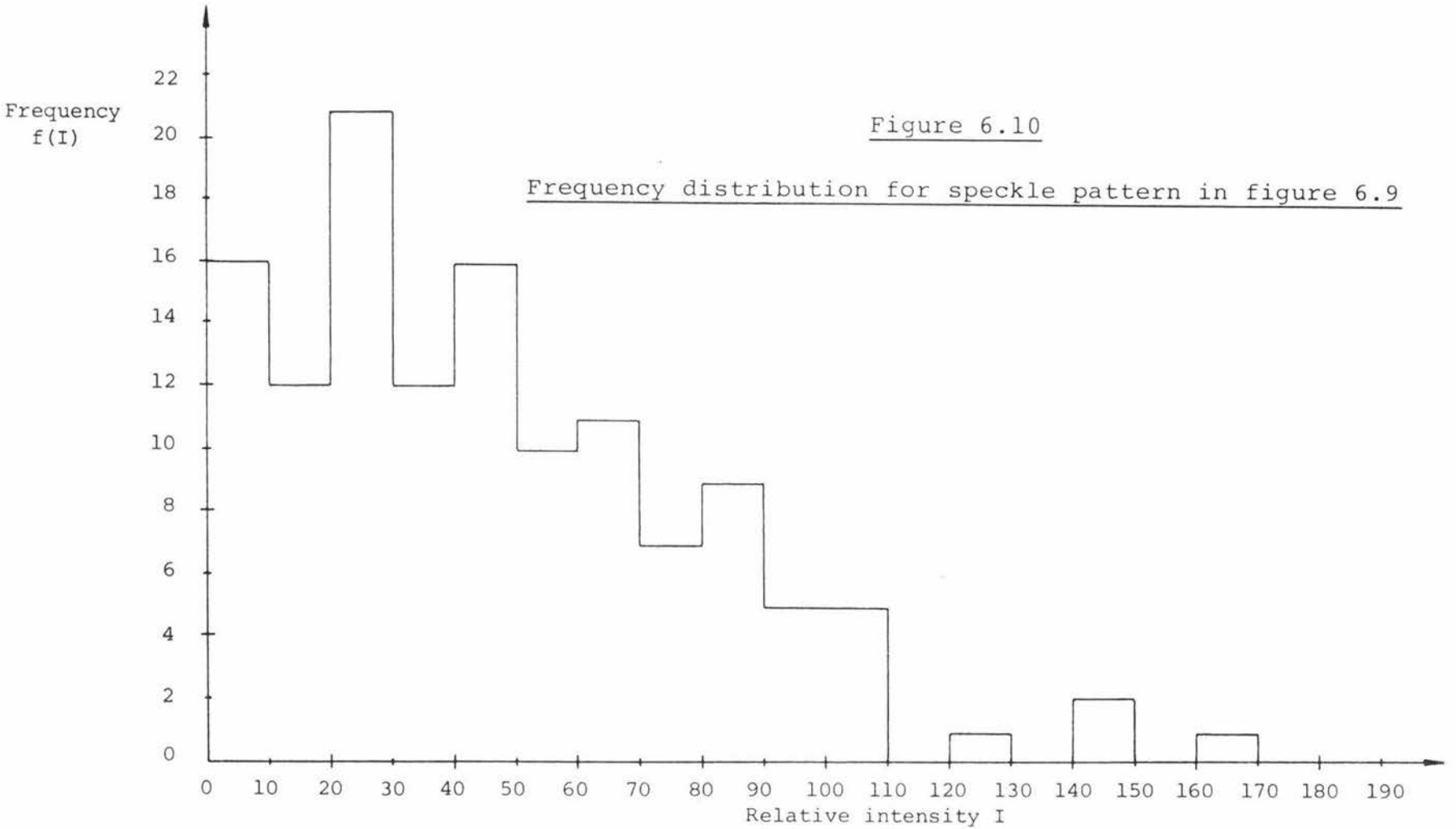

Figure 6.10

Frequency distribution for speckle pattern in figure 6.9

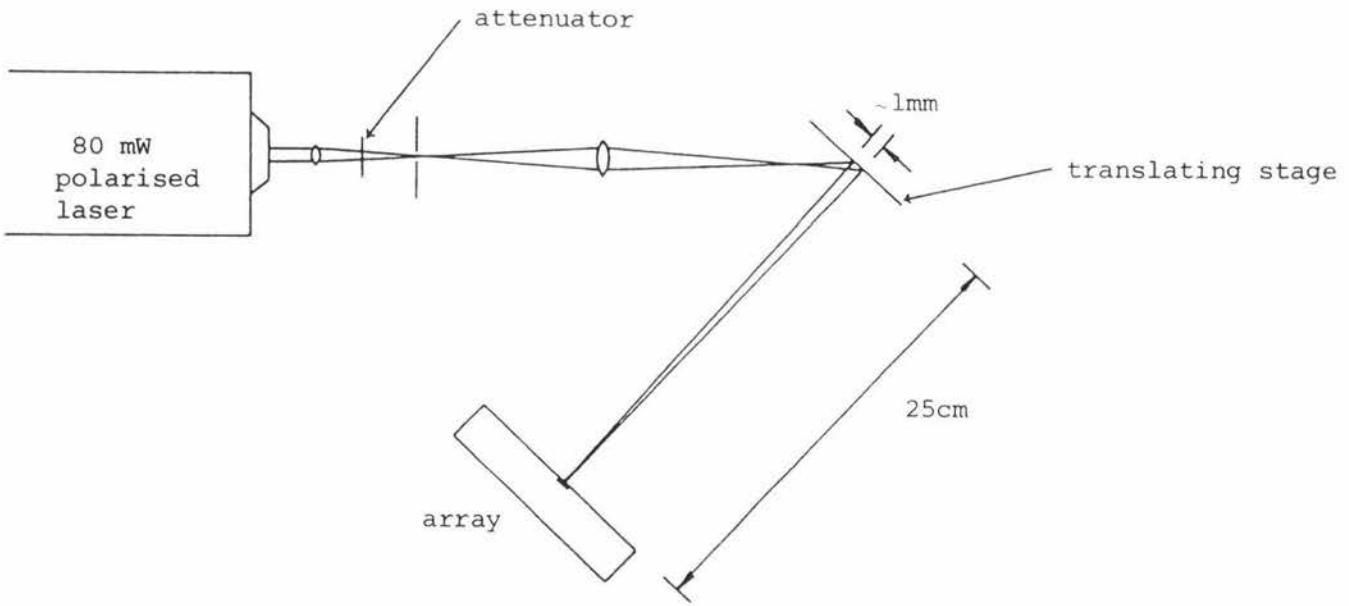

Figure 6.11 The optical arrangement used to produce a fully developed speckle pattern

as a smooth curve by the array. The object used to form the speckle pattern was rough enough to ensure large values of phase shift for all but glancing angles of incidence.

The program used in conjunction with this arrangement, to obtain the intensity distribution of the speckle pattern, is given in figure 6.12. The following notes are given to clarify each flow charted operation.

1. When the program is run the computer displays the word 'input' on its 8 digit display to act as a prompt to the experimenter to adjust the apparatus.

2. When a shutter has been placed in the beam's path to darken the array the experimenter presses a key to continue the program.

3. The prompt signal is removed.

4. A scan is made of the darkened array and the resultant data is stored in the computer. This data is then used throughout the experiment to provide zero corrections. (During the course of the experiment voltage drift will be small and so a single dark scan will be sufficient).

5,6. The experimenter is prompted to adjust the object's position so that a new speckle pattern is produced.

8. The new speckle pattern is loaded, corrected and then stored in memory M2 (128 bytes long).

10. The contents of location A + pc is loaded into the X register. (A is the address of the first location in M2 and pc refers to the particular pixel intensity being considered).

Figure 6.12

Program to find intensity distribution

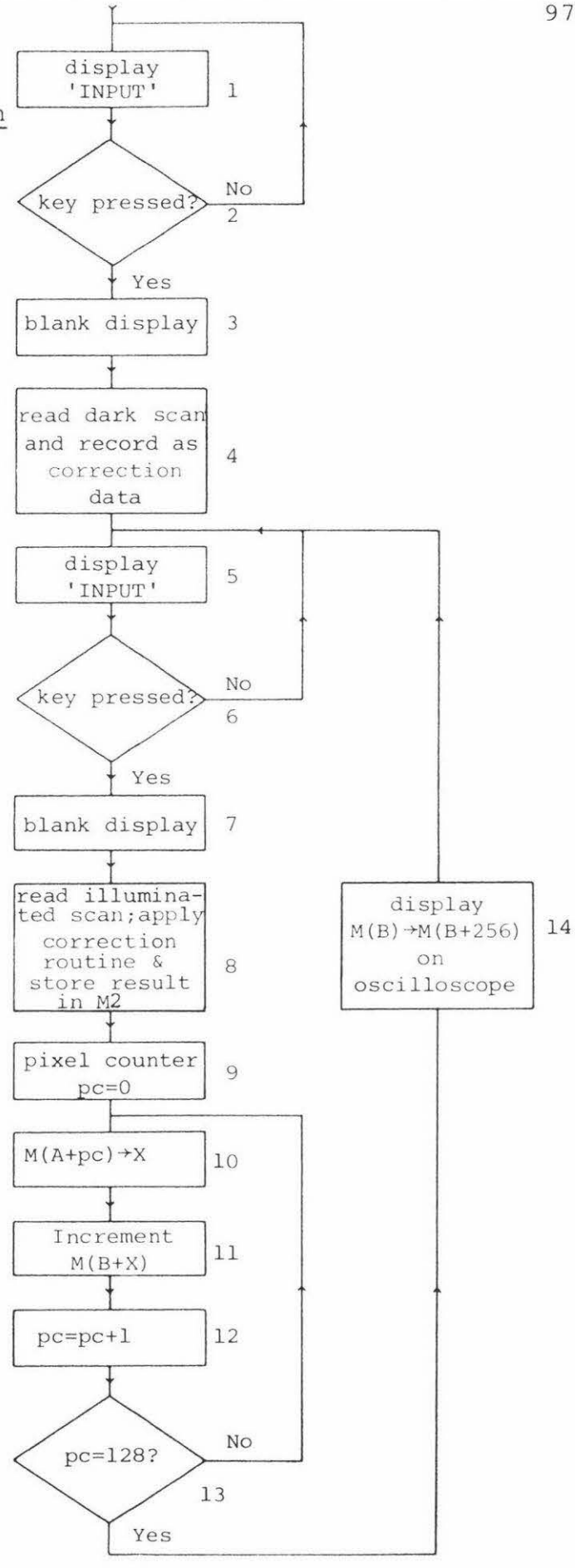

11. The contents of location B + X in memory M4 (256 bytes long) are incremented by one. (Where B is the address of the first location in M4 and X refers to the contents of the X register).

12,13. Increment pc and check to see whether all pixel outputs have been considered.

14. Display the contents of M4 (the intensity distribution) on the oscilloscope for five seconds.

Although not shown in the flow chart, memory M4 is cleared before the start of the program.

Once a satisfactory intensity distribution has been produced (which often requires 20 to 80 scans of the array) the program is terminated by the experimenter. The data in M4 is then used by another program which calculates the sums

$$\Sigma f(I)I;\ \Sigma f(I)I^2;\ \Sigma f(I), \tag{6.4}$$

where f(I) is the frequency of occurrence for the particular intensity I. This value can be obtained directly from M4. (Note that 'I' is now being used rather than the count c to represent the compensated data because we have established that it is proportional to the light intensity).

Once these results have been obtained it is then a simple matter to calculate the contrast with a pocket calculator since

$$\begin{aligned} \sigma_I &= (\langle I^2\rangle - \langle I\rangle^2)^{\frac{1}{2}} \\ &= \left(\frac{\Sigma f(I)I^2}{\Sigma f(I)} - \left(\frac{\Sigma f(I)I}{\Sigma f(I)}\right)^2\right)^{\frac{1}{2}}, \end{aligned} \tag{6.5}$$

and $C = \frac{\sigma_I}{\langle I \rangle}$.

The intensity distribution data stored in M4 may be converted to a probability distribution by dividing each value of f(I) by the total number of sample points $\Sigma f(I)$. Figure 6.13 is a typical example of such a distribution, obtained using the apparatus and programming previously described. To simplify plotting, and smooth out statistical fluctuations the results have been summed over every five consecutive data points.

This graph clearly shows the expected decaying exponential form at medium and high intensities but problems do seem to have arisen at low intensities where f(I) is very small. This particular phenomenon was observed in all probability measurements that were made, and was probably caused by one or more of the following effects.

i) Electronic noise.

ii) Light scatter from the glass covering the array, and from surrounding objects.

iii) Possible depolarization of the light scattered by the object.

iv) The phenomenon of charge transfer inefficiency within the array.

These four possibilities are discussed more fully in Appendix E with the conclusion that the first two contenders are the most likely.

To compare the results obtained in figure 6.13 with the predicted curve in figure 2.8 we must decide how much of the detected intensity is <u>not</u> due to fully developed speckle. Since the data has been graphed by grouping five intensities

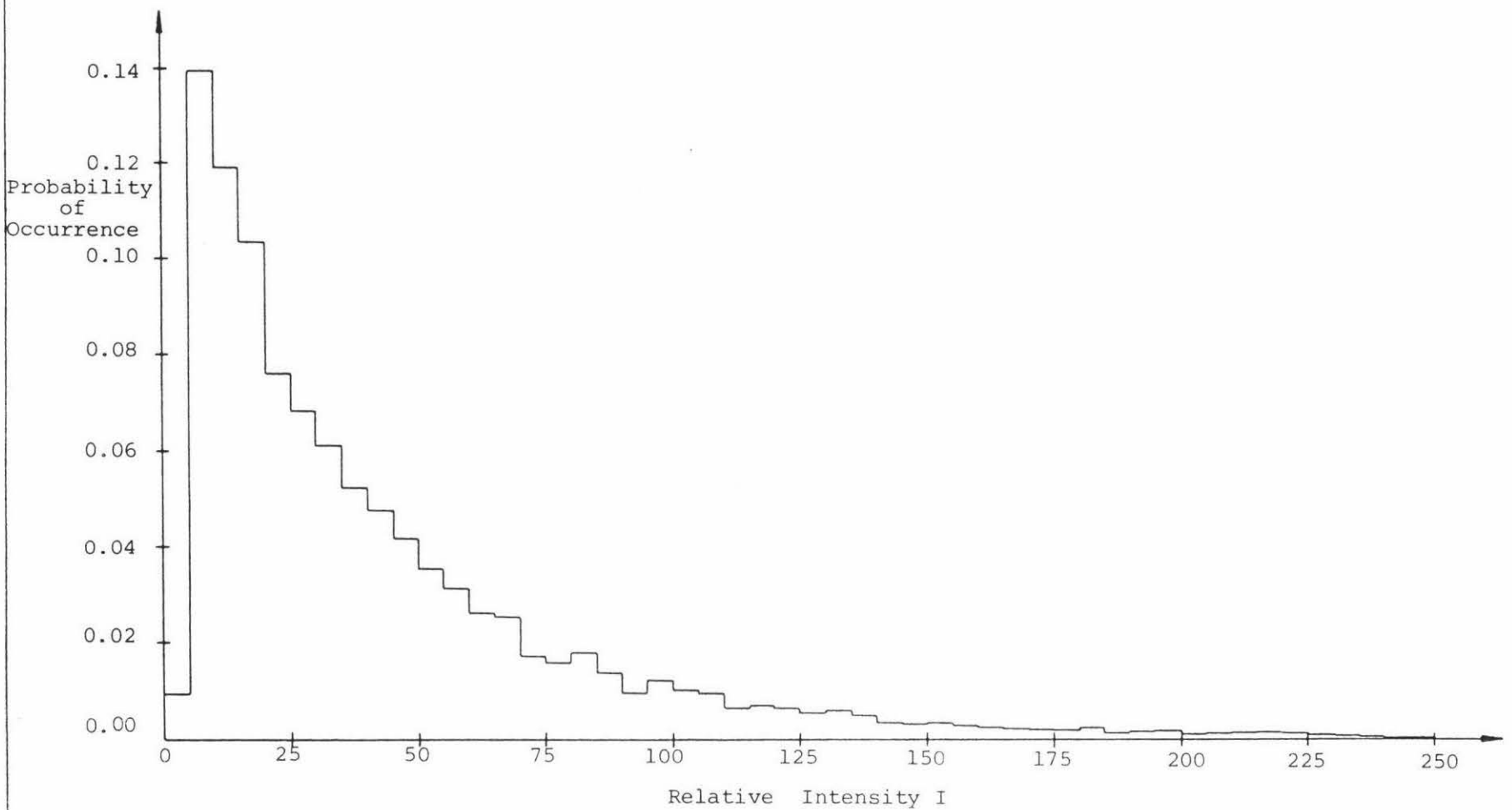

Figure 6.13 Probability distribution for a fully developed speckle pattern (after 60 scans)

together it was decided to see what would happen if the first five intensities were ignored. Figure 6.14 is the result.

The expected probability density is given by the equation

$$p(I) = \frac{1}{\langle I \rangle} \exp\left(\frac{-I}{\langle I \rangle}\right), \qquad (6.6)$$

but since we have essentially integrated our intensities over five pixels, figure 6.14 actually represents

$$P(I) = \frac{1}{\langle I \rangle} \int_a^b \exp\left(\frac{-I}{\langle I \rangle}\right) dI, \qquad (6.7)$$

where $a = I - 2.5$ and $b = I + 2.5$.

This particular function has been plotted for comparison with the experimental data in figure 6.14. The close fit between the two results (when statistical fluctuations $f(I)^{\frac{1}{2}}$ are considered) would appear to confirm the theoretical treatment given in chapter 2. (A more accurate test done by McKechnie {ref 2.2 p 19}, who used 23,000 samples, produced an even closer fit).

The contrast for this pattern was found to be 0.93 before correction and 1.05 afterwards, indicating an ideal correction value of less than five intensity levels. To see if these contrast results were typical of all speckle patterns five more measurements were made for various values of $\langle I \rangle$ and speckle size. The results are listed on page 103. Because of the difficulty in determining the contribution of scatter and noise to these results it was decided to establish the criterion of ignoring all intensities with zero probability. (For the results in figure 6.13 there happened to be three).

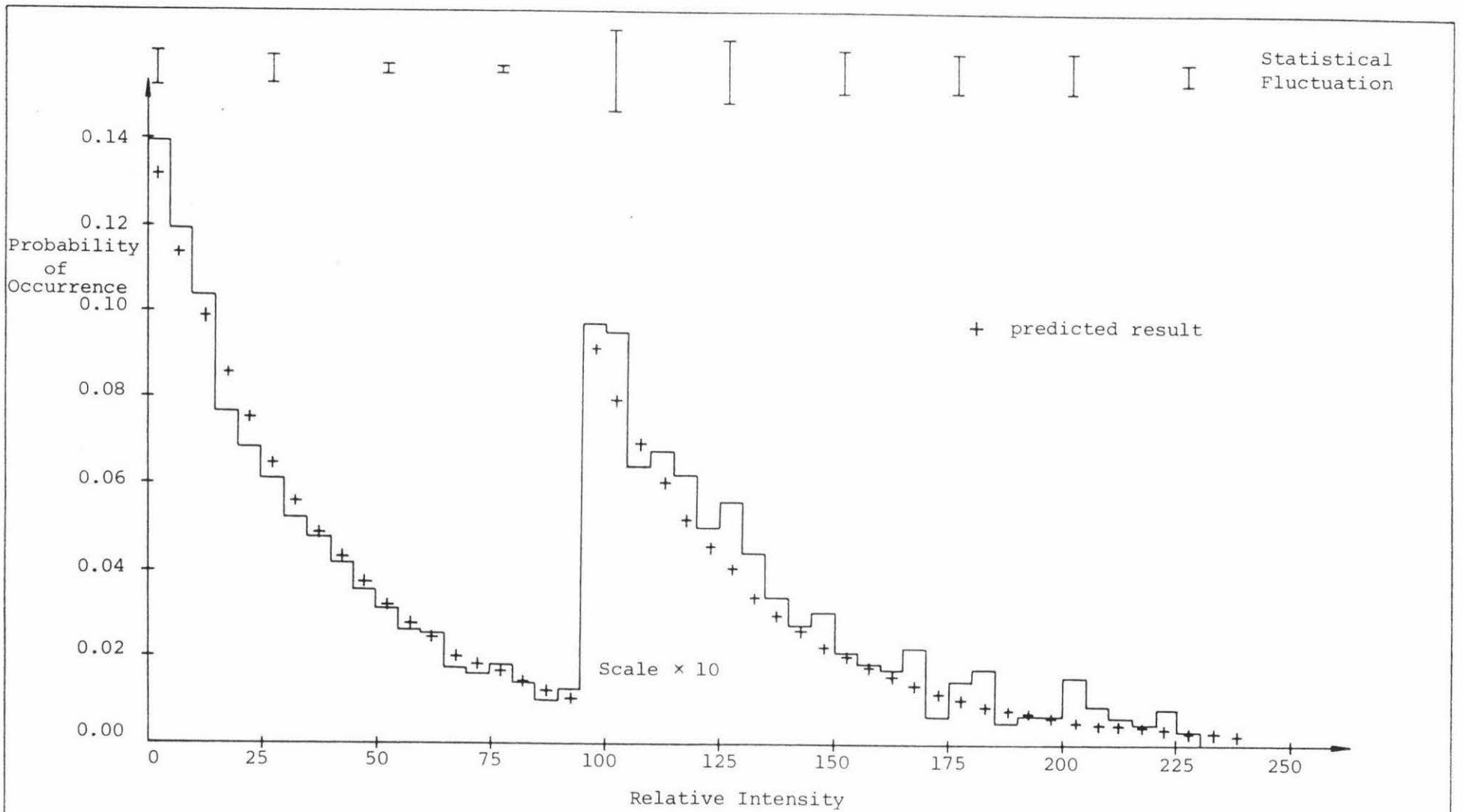

Figure 6.14 Corrected probability distribution and theoretical results

Table 6.3 Contrast for six fully developed speckle patterns

Run	<I>	σ_I	Contrast	Z	Corrected Contrast
1	12.40	12.40	1.00	0	1.00
2	29.16	28.00	0.96	2	1.03
3	21.63	20.52	0.95	1	0.99
4	24.45	21.69	0.89	3	1.01
5	24.13	22.04	0.91	2	1.00
6	40.37	37.35	0.93	3	1.00

where Z = number of intensity levels with zero probability (not including high intensities).

The average contrast for these speckle patterns is 1.01±0.01, close to the predicted contrast. It is interesting to note that the brighter speckle patterns generally had larger values of Z, as would be expected if the error were caused by scatter.

6.6 Probability Density and Contrast of a Partially Polarized Speckle Pattern

To check the results obtained in section 2.5 the above experiment was repeated using a 4mW partially polarized laser as the light source. A typical probability distribution for the speckle pattern produced using this arrangement is given in figure 6.15. Results have been summed over every five consecutive intensity levels and for the sake of comparison the first five levels have again been ignored.

The most obvious difference between this result and that pictured in figure 6.14 is the reduction in the probability at low intensities. As expected from the discussions in section 2.5 there is also a marked decrease in contrast; if we use the above mentioned criterion a contrast of 0.86 is obtained against 1.01 for the fully developed pattern.

Figure 6.15 Corrected probability distribution of a partially polarized speckle pattern (from 64 scans of array)

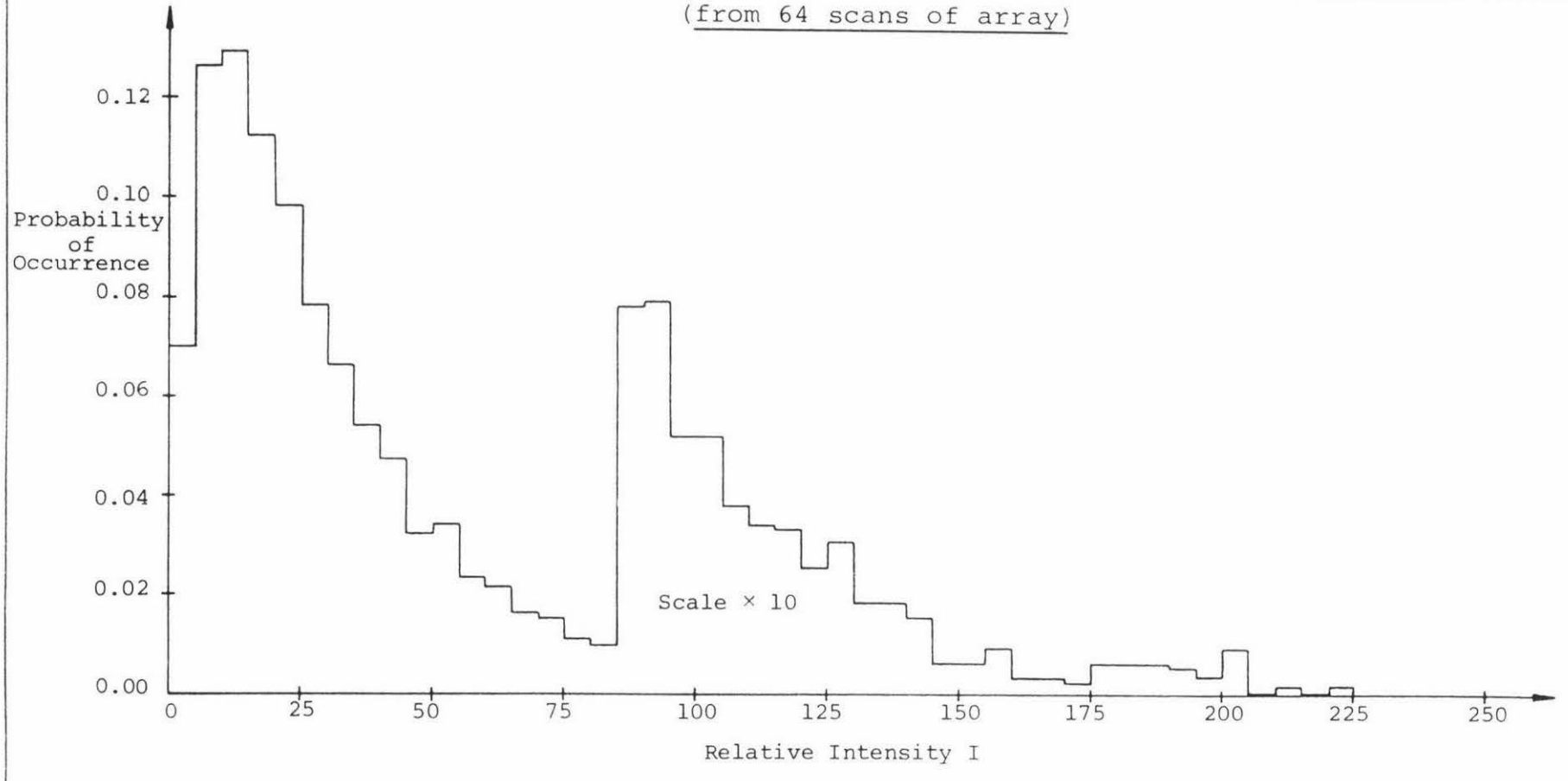

Table 6.4 lists six similar results which give an average contrast of 0.91±0.01.

Table 6.4 Contrast for six partially developed speckle patterns

Run	<I>	σ_I	Contrast	Z	Corrected Contrast
1	25.53	21.40	0.84	2	0.91
2	27.28	22.23	0.81	3	0.92
3	27.05	21.63	0.80	3	0.90
4	26.83	21.80	0.81	3	0.91
5	27.02	21.66	0.80	3	0.90
6	27.68	22.03	0.80	3	0.89

To check on the degree of correlation between the two orthogonally polarized patterns the above experiment was repeated with a sheet of polaroid placed in the beam. This will leave only one plane polarized beam which should produce a fully developed speckle pattern. The results are tabulated below.

Table 6.5 Contrast results with polaroid added

Run	<I>	σ_I	Contrast	Z	Corrected Contrast
1	32.55	24.50	0.75	3	0.83
2	30.89	24.52	0.79	2	0.85
3	21.90	18.44	0.84	2	0.93
4	29.35	24.50	0.83	2	0.90
5	27.75	22.80	0.82	2	0.89
6	33.49	29.37	0.88	3	0.96
7	28.59	24.88	0.87	3	0.97
8	35.81	28.22	0.79	3	0.86

Mean contrast is 0.90±0.05.

This result was not totally unexpected as visual observation of large speckle patterns showed that there was little change in the structure of the pattern when the polaroid was introduced and rotated. This indicated a close correlation between the two speckle patterns.

What was unexpected, was the low contrast obtained both with and without the polaroid. If the two components were closely correlated then we would expect (from figure 2.12) a fully developed speckle pattern in both cases. The only plausible explanation for this effect would seem to be that the object has depolarized the incident light in both instances. However this does not explain why the polarized laser, which used an identical optical arrangement, produced a contrast of one. More information concerning the mode structure and polarization of the 4mW laser would appear to be necessary before any firm explanation can be given.

6.7 Surface Roughness Measurement

Conventionally surface roughness (σ_r) and correlation length (T) have been measured by a stylus-type instrument which rubs over the object's surface producing an output voltage proportional to the surface profile. This technique, discussed in detail by Reason {ref 6.1}, has the disadvantage of looking at only small portions of the surface. There is also the possibility of scratching the surface with the diamond stylus.

The following technique, although not as precise, does allow non-contact measurement of surface roughness over reasonably extended areas, with only moderate difficulty.

As shown in Chapter 2 a reduction in speckle contrast (in the specular direction) results when the surface roughness (σ_r) is reduced, or the angle of incidence (θ) increased. The following experiments measure this variation in contrast for a variety of angles and surfaces. The optical arrange-

ment depicted in figure 3.10 and discussed in section 3.8 was used throughout this experiment with the test object mounted on the translating stage. The various apparatus measurements are listed below.

i) Lens L_1 to pinhole; 72mm.
ii) Lens L_2 to object; adjusted to suit angle of illumination.
iii) Object to lens L_3; 60mm
iv) Lens L_3 to array; adjusted to suit angle of illumination.
v) Focal length of L_1 and L_2; 72mm.
vi) Focal length of L_3; 16mm.

All measurements, ± 1mm.

To investigate the variation in probability density which occurs as θ is adjusted the experiment was performed, using a glass test object roughened with 800 grit carborundum powder, at incidence angles ranging from 60 to 85 degrees in 5 degree steps. The results are depicted in figures 6.16 to 6.21. The various statistics calculated from these distributions are listed below.

Table 6.6 Contrast as a function of θ

θ(degrees)	N	<I>	σ_I	Contrast
60	13312	50.11	33.62	0.67
65	13952	60.85	34.79	0.57
70	13952	73.08	36.61	0.50
75	14848	114.03	27.70	0.24
80	6528	123.79	12.49	0.10
85	1536	61.87	3.30	0.05

where N is the number of sample points being considered, e.g. if N = 13312 then there have been 13312/128 = 104 scans of the array made. (Note that none of the above contrast results have been corrected for scatter).

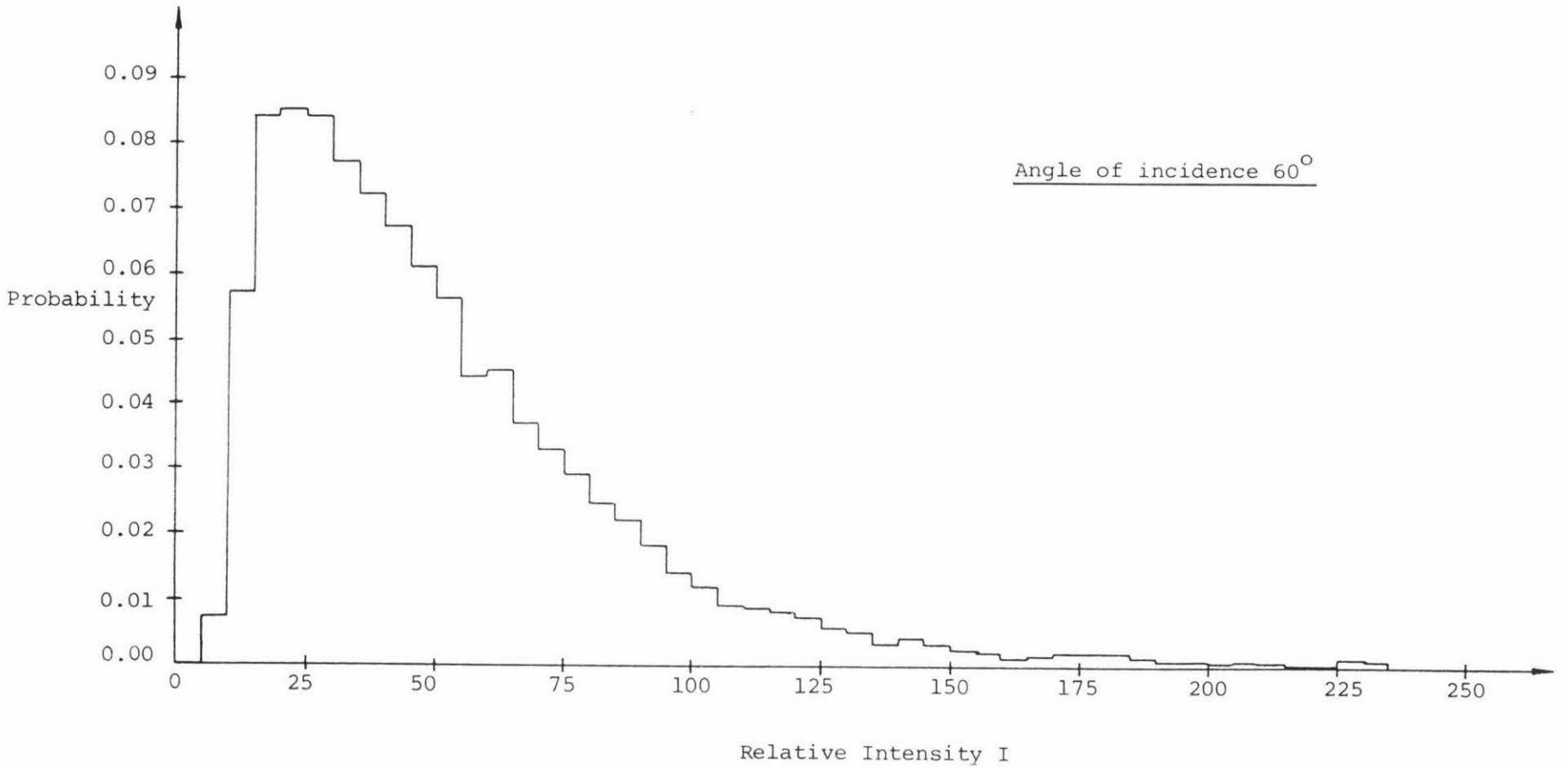

Figure 6.16 Probability distribution of laser speckle

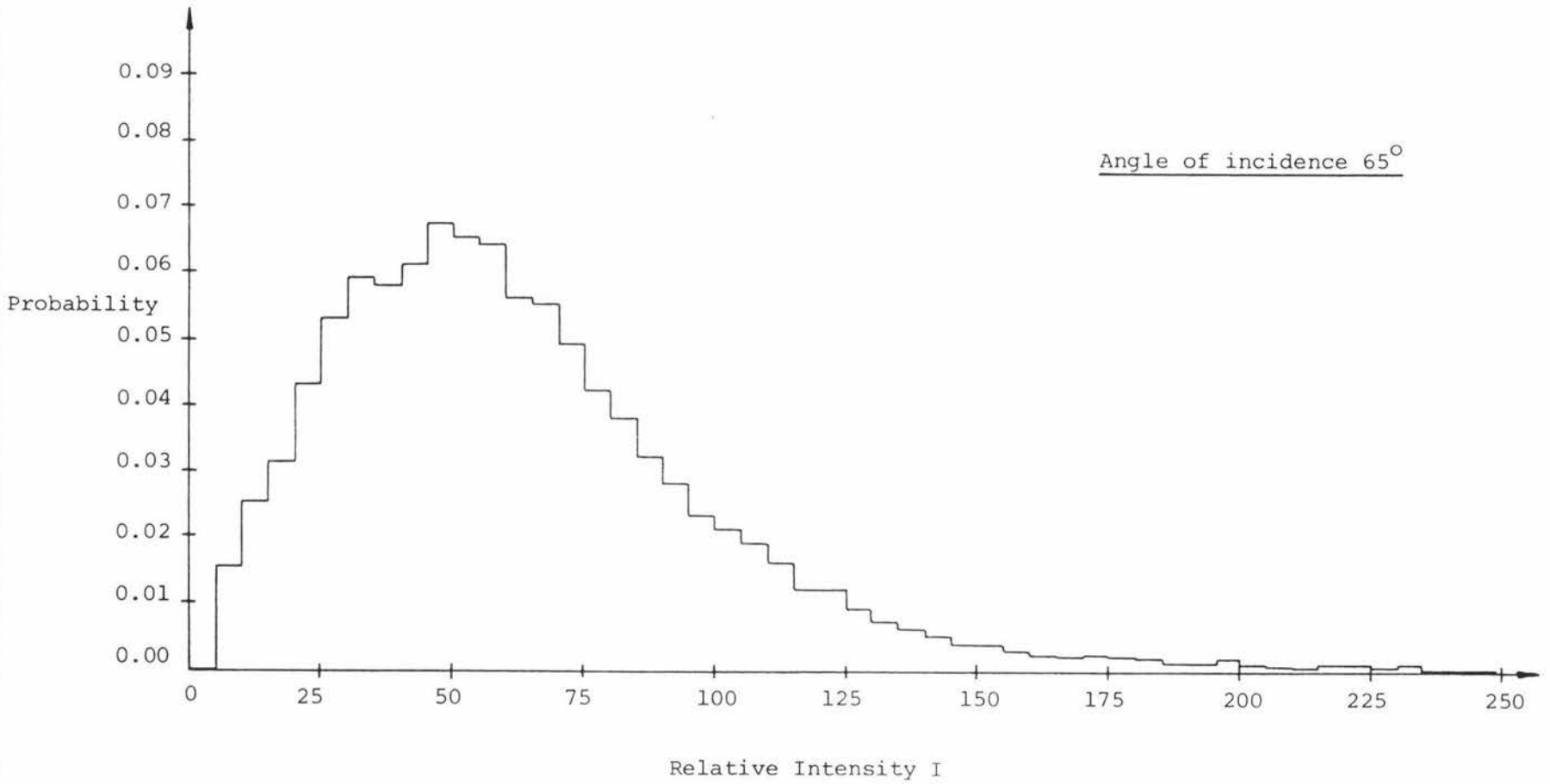

Figure 6.17 Probability distribution of laser speckle

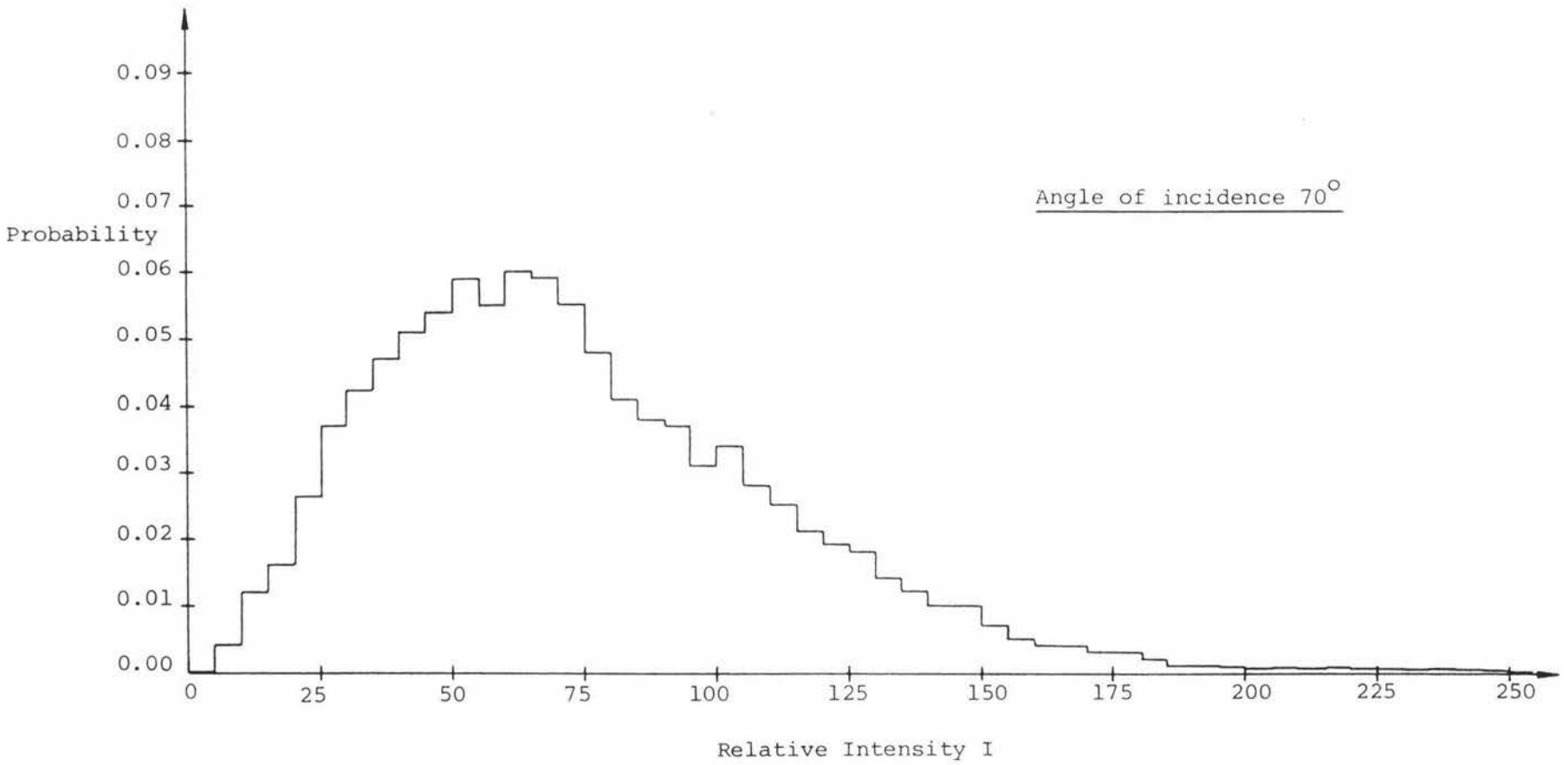

Figure 6.18 Probability distribution of laser speckle

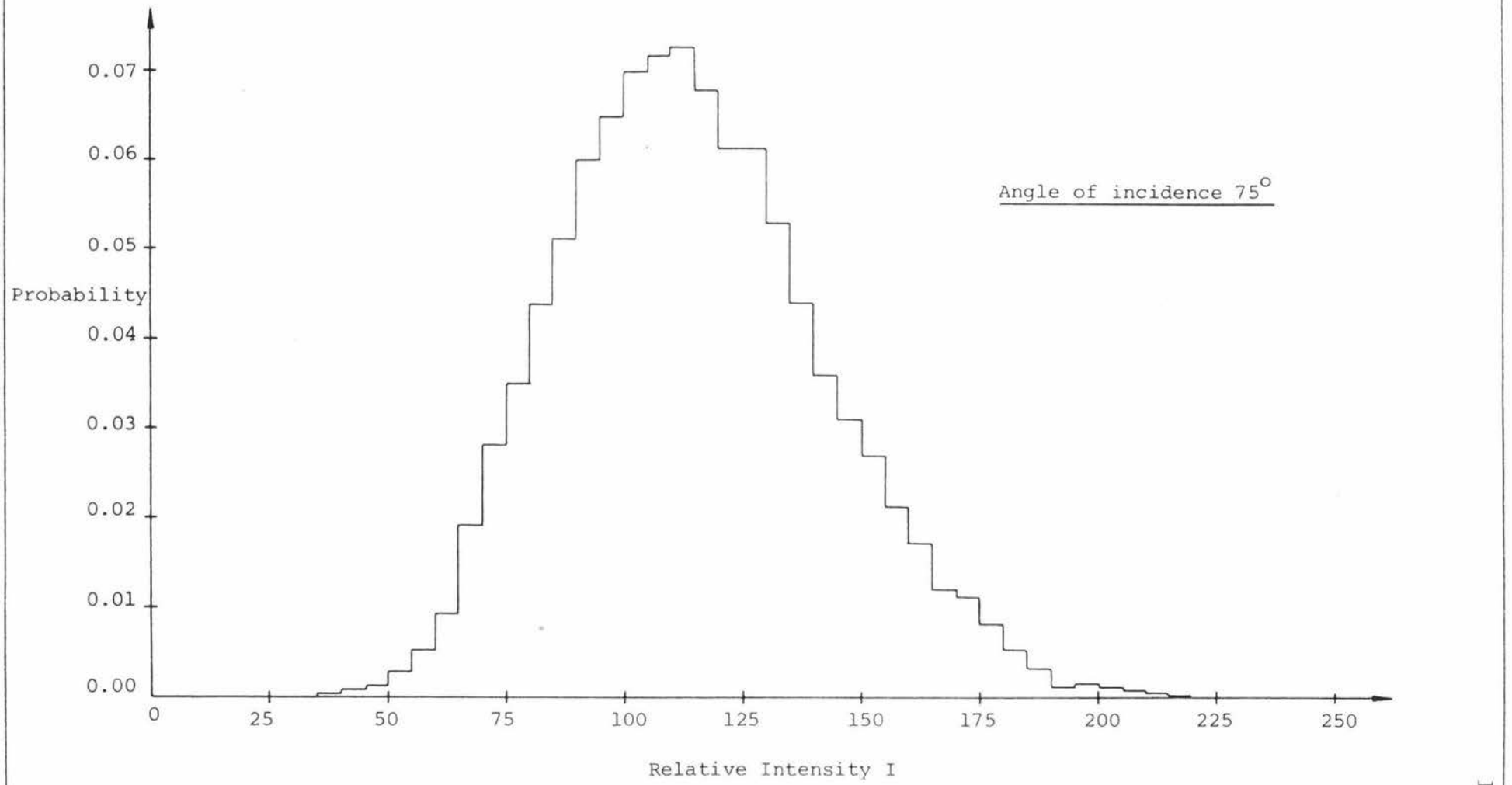

Figure 6.19 Probability distribution of laser speckle

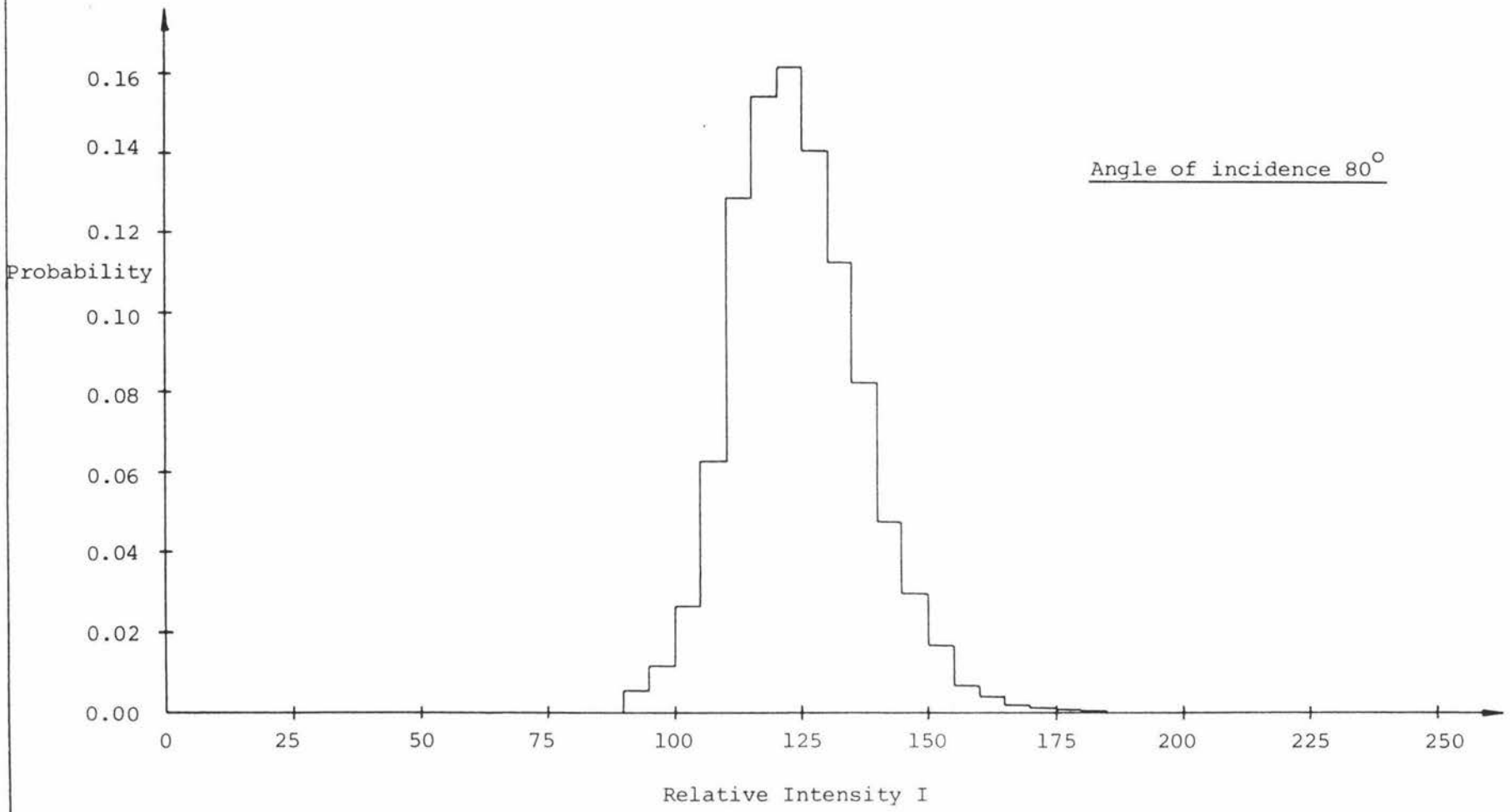

Figure 6.20 Probability distribution of laser speckle

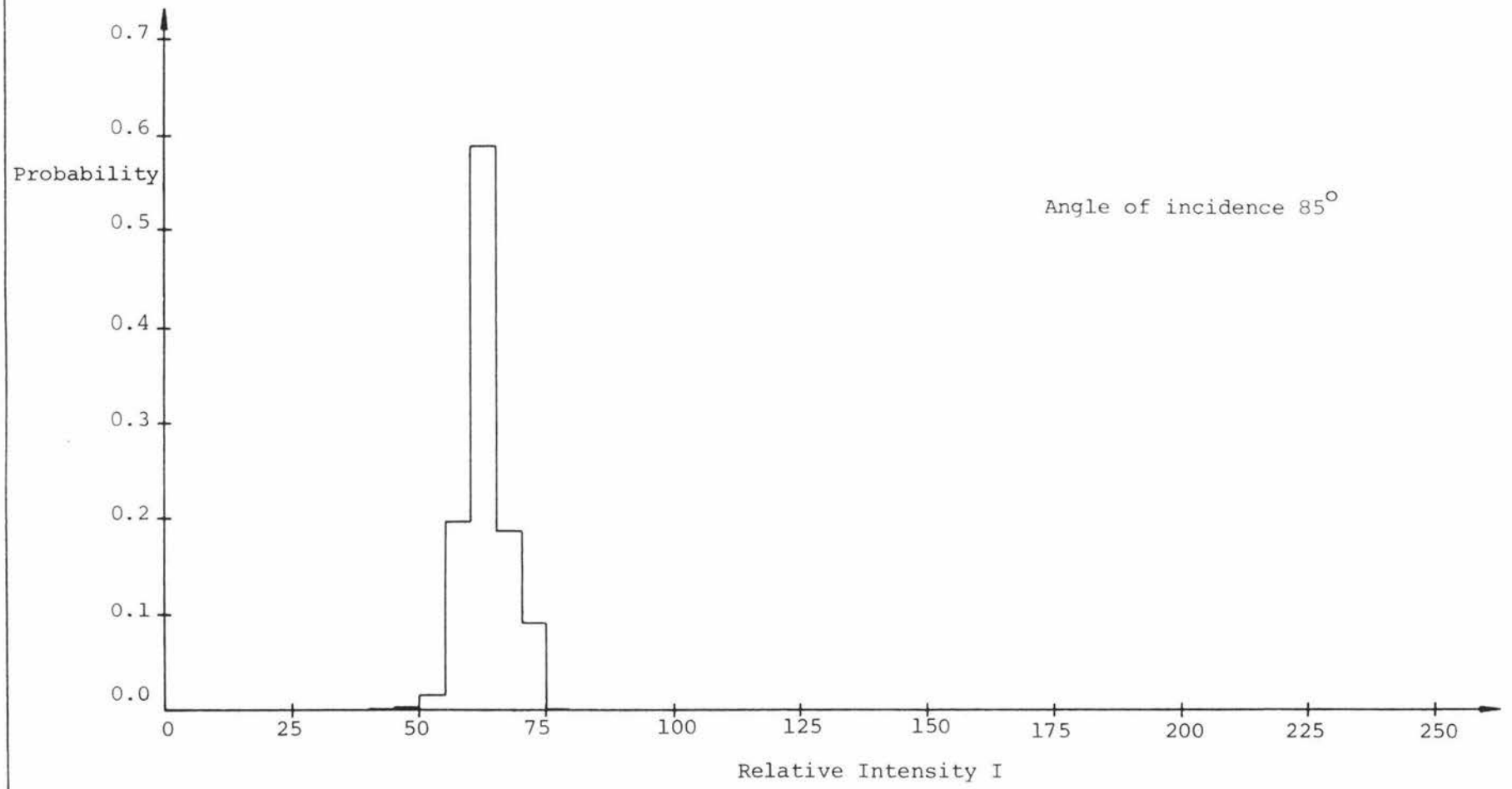

Figure 6.21 Probability distribution of laser speckle

Figures 6.16 to 6.21 clearly show the transition from the fully developed speckle pattern for small ($<60^{o}$) angles of incidence to the more symmetrically placed distributions at glancing incidence angles. As θ tends toward 90^{o} the probability distribution will approach a delta function centred at $I = \langle I \rangle$. With the present experimental arrangement this result is not possible for the following reasons.

i) At glancing angles of incidence the illuminating spot becomes very extended and will tend to illuminate objects other than the desired surface. This will effectively increase the surface roughness and so, (from figure 2.6) increase the contrast.

ii) Small scratches, particles of dust, and films of grease on the surfaces of lenses (especially L_3) and the array window produce diffraction and interference patterns which cause intensity variations across the array.

iii) Electronic noise ($\sim \pm \frac{1}{2}$ count) presents a degree of variation in the video signal which increases contrast slightly.

At the other end of the scale (small values of θ) the speckle pattern will not be fully developed because a partially polarized light source is being used. This will tend to reduce the contrast from the expected value of 1.

The above factors must be taken into account when analysing the surface roughness measurements.

The actual measurement of surface roughness was undertaken by determining contrast for a range of angles and surfaces and then curve fitting the results to equation 2.45. Three surfaces were used, all made from aluminium abraded

with different grades of carborundum grit. Five measurements were made for each angle, from which an average contrast and uncertainty were obtained. The results are tabulated below.

Table 6.7 Contrast as a function of θ for three differently abraded surfaces

Angle of incidence(θ)	Surface A (220 grit)	Surface B (500 grit)	Surface C (800 grit)
45.0±0.5°	-	-	0.87±0.08
50.0	-	-	0.85±0.06
55.0	-	-	0.78±0.02
60.0	-	-	0.69±0.04
65.0	-	0.90±0.06	0.50±0.02
70.0	0.95±0.07	0.85±0.05	0.33±0.02
72.5	-	0.59±0.02	-
75.0	0.93±0.04	0.40±0.03	0.21±0.02
80.0	0.83±0.05	0.23±0.03	0.14±0.02
82.5	0.45±0.02	-	-
85.0	0.13±0.02	0.09±0.02	0.06±0.02

Note that the criterion established earlier, concerning the correction of the intensity distribution, could not be applied to these results because most of them had zero values of intensity probability which resulted from a real low contrast, as well as from scatter. It is this lack of correction which has resulted in the comparatively large uncertainties in the above results. (An improved correction procedure for this more general situation is discussed in Appendix E).

The above results have been plotted in figure 6.22 along with best fit curves obtained by performing a least squares analysis on the data. The resultant roughness parameters are listed on page 117.

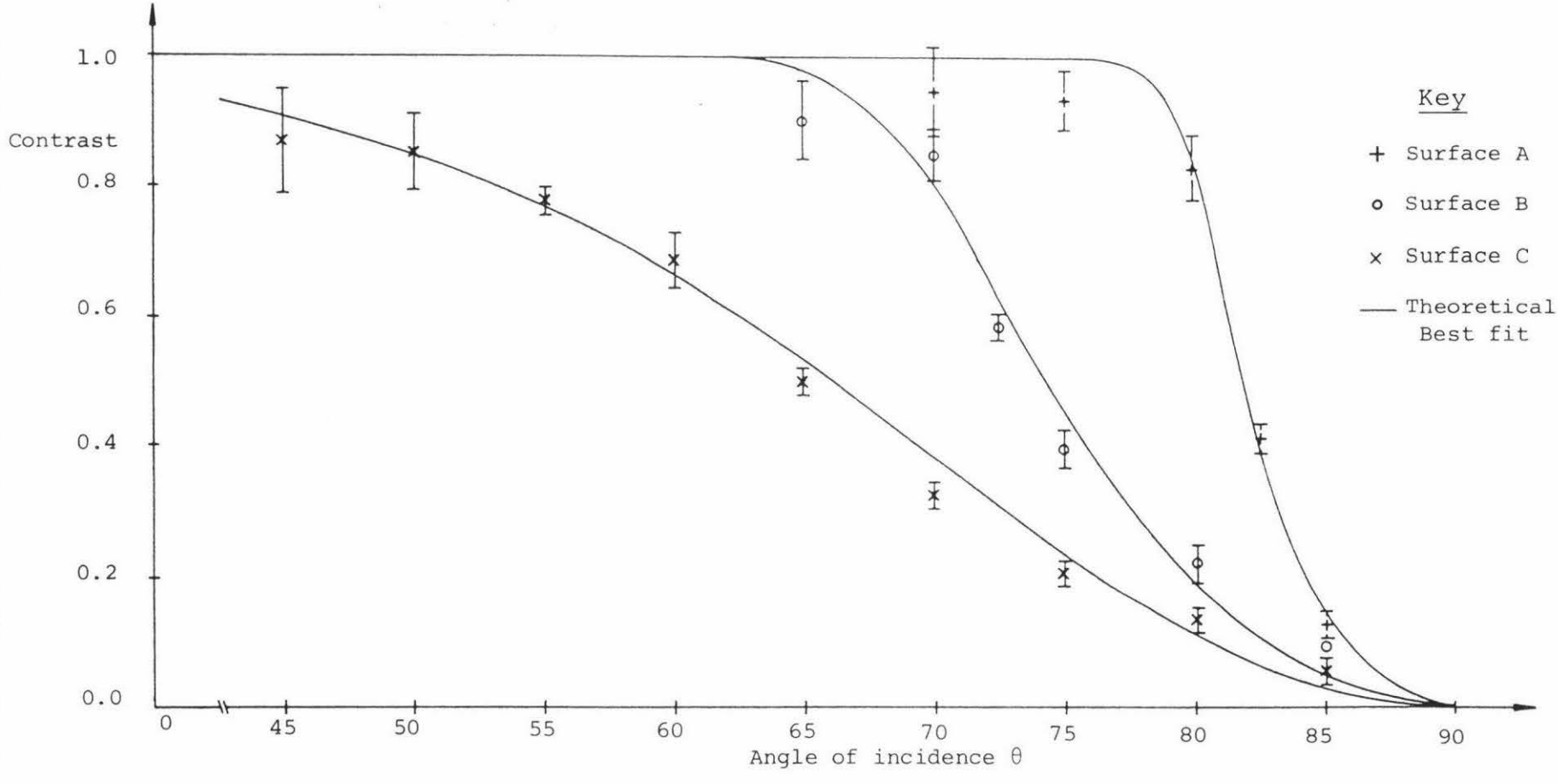

Figure 6.22 Contrast vs. θ for 3 rough surfaces

Table 6.8 Surface roughness results

Surface	Roughness (σ_r)	Number of scattering centres (n)	Sum of the squares ($\Sigma\Delta^2$)
A	0.61μm	97	0.0094
B	0.27μm	42	0.016
C	0.09μm	2	0.081

No uncertainties have been given here because of the difficulty in getting equation 2.45 into a linear form. The least squares analysis was performed on a computer (see Appendix C) using a simple trial and error program which substituted various values of n and σ_r into 2.45 until a minimum value of $\Sigma\Delta^2$ was found, where Δ is the difference between the experimental and theoretical results.

The value of n can be determined approximately by other means. With the optical arrangement in figure 3.10 and the apparatus measurements given previously, the array will be in the defocus plane of the objective lens L_3 (see figure 2.4). This means that all of the illuminated area on the object ($\sim$ 1mm in diameter) will contribute to the intensity of any one pixel. By equation 2.49 we can therefore say that for a value of T of the same order as θ_r, n will be

$$n = \frac{d^2}{T^2} = \frac{(1\times10^{-3})^2}{(0.5\times10^{-6})^2} = 4\times10^6.$$

If, as indicated by Nakagawa et al. {ref 6.2 p 953}, T is larger than σ_r (often by as much as a factor of 10 to 100) the value of n will be reduced to between 400 and 40000, still larger than the results obtained in table 6.8.

However, if the factors noted earlier in the section are considered, the situation changes quite appreciably. A decrease in contrast at large angles θ would result if all optical noise were removed and an increase at small angles

if a polarized laser were used. This would have the effect of steepening the curves which, from figures 2.6 and 2.7, would lead to an increase in both σ_r and n, as required.

Future experiments along these lines will need to be carefully thought out if good results are to be obtained. The use of a polarized laser would partially solve the problems, as would improved optical componentry. The correction problem with regards scatter would also have to be improved as this leads to a lessening of the contrast at all angles.

The chief advantage which this technique has over the more standard roughness measurement procedures (which use speckle) is the ability to observe contrast changes for even optically rough surfaces by adjusting the angle θ appropriately. The more conventional techniques (e.g. Asakura ref 2.4) generally measure probability density and contrast at a normal or small angle of incidence. This limits the surfaces used to those with optically smooth surfaces (i.e. $\sigma_\phi < \pi$).

6.8 Array Noise

As mentioned in section 6.3 there is an alternative method for measuring array noise. If the probability distribution routines, as previously described, are carried out with the array in the dark, the noise recorded by the microprocessor will show up as intensities greater than zero having a non-zero probability of occurrence. After 39 scans it was found that the intensity level 1 had been observed 256 times. No larger intensities were observed. This means that 5% (256/(128x39)) of all noise levels were greater than ½ a count but less than 1½ counts. Since the peak-to-peak amplitude of the noise is not affected by the zero correction routine (which subtracts another noise scan) we can say that the peak-to-peak noise lies somewhere between ½ and 1½ intensity levels, consistent with the value of 0.7 obtained in section 6.3. A more detailed estimate would require knowledge of the noise amplitude distribution after correction.

6.9 Surface Displacement Measurement

Standard photographic techniques which use speckle to measure surface displacement require a doubly exposed photograph to be made; one exposure before and one after the displacement. The resultant negative will then consist (for a limited range of displacements) of a large number of doubled speckles all approximately the same distance apart. If a laser is shone through such a transparency interference fringes will be formed because of the close and reasonably consistent spacing of the doubled speckles. The spacing of these fringes can then be directly related to the object's displacement using standard diffraction formulae.

The chief difficulties associated with this technique are listed below.

i) For displacements of more than approximately 20 speckle diameters the pattern begins to decorrelate i.e. the speckles change shape and intensity. This results in a loss of fringe contrast.

ii) Large displacements cause the shifted speckles to overlap unrelated unshifted speckles. This also results in a loss of fringe contrast.

iii) For very large displacements (>1mm) the speckles may move so far, and be so large, that formation of a fringe pattern is not possible.

iv) For displacements of less than one speckle diameter the fringes will have reduced contrast because of the incomplete speckle separation.

v) The photographic process is necessarily fairly slow requiring (for modest laser powers) long exposures (tens of seconds), developing, a second exposure to record the fringes, and then a possible microdensi-

tometer scan of the fringe pattern.

The chief advantage of this technique is that it allows displacement measurements to be made over an entire surface from a single doubly-exposed negative, something which is impossible with the electronic system to be described below.

The linear array and microprocessor system is ideally suited to displacement measurement since the recording of a speckle pattern can be simply and quickly accomplished using the techniques described previously. Once two such patterns have been stored in the computer's memory a cross-correlation may be performed to determine the displacement which has occurred between storage times. The method by which this is accomplished can be understood by studying figures 6.23 to 6.26 in conjunction with the notes given below.

i) The two speckle patterns (examples of which are pictured in figures 6.23 and 6.24) are stored in memory M4 (see Appendix B) after having been zero-corrected and compensated to remove non-uniformities.

ii) Data in the first half of M4 (M4a) has its mean value $\langle I_a \rangle$ calculated. A similar process is carried out on M4b to find $\langle Ib \rangle$.

iii) Data values in M4a greater than or equal to $\langle I_a \rangle$ are set to 1 while those with values less than $\langle I_a \rangle$ are set to zero. This 'clipping' process is repeated on M4b using $\langle I_b \rangle$.

iv) The segment of data in M4b from pixel 20 to 107 is multiplied by the segment of pixels 0 to 87 in M4a. (Multiplication can now be accomplished using the microprocessor 'AND' instruction because of the clipping process). The resultant products are added together to produce the cross-correlation coefficient for lag -20.

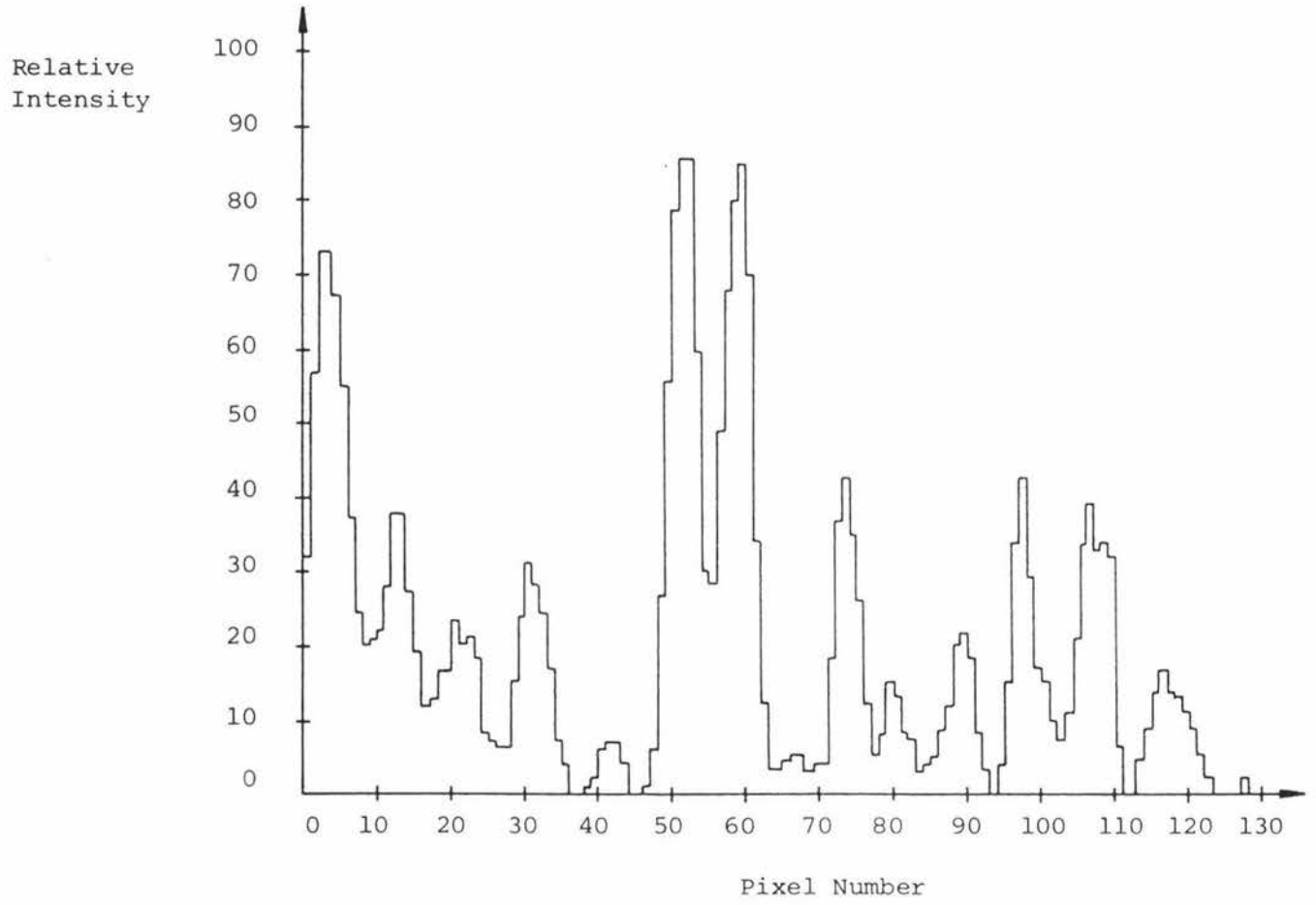

Figure 6.23 Speckle profile before displacement

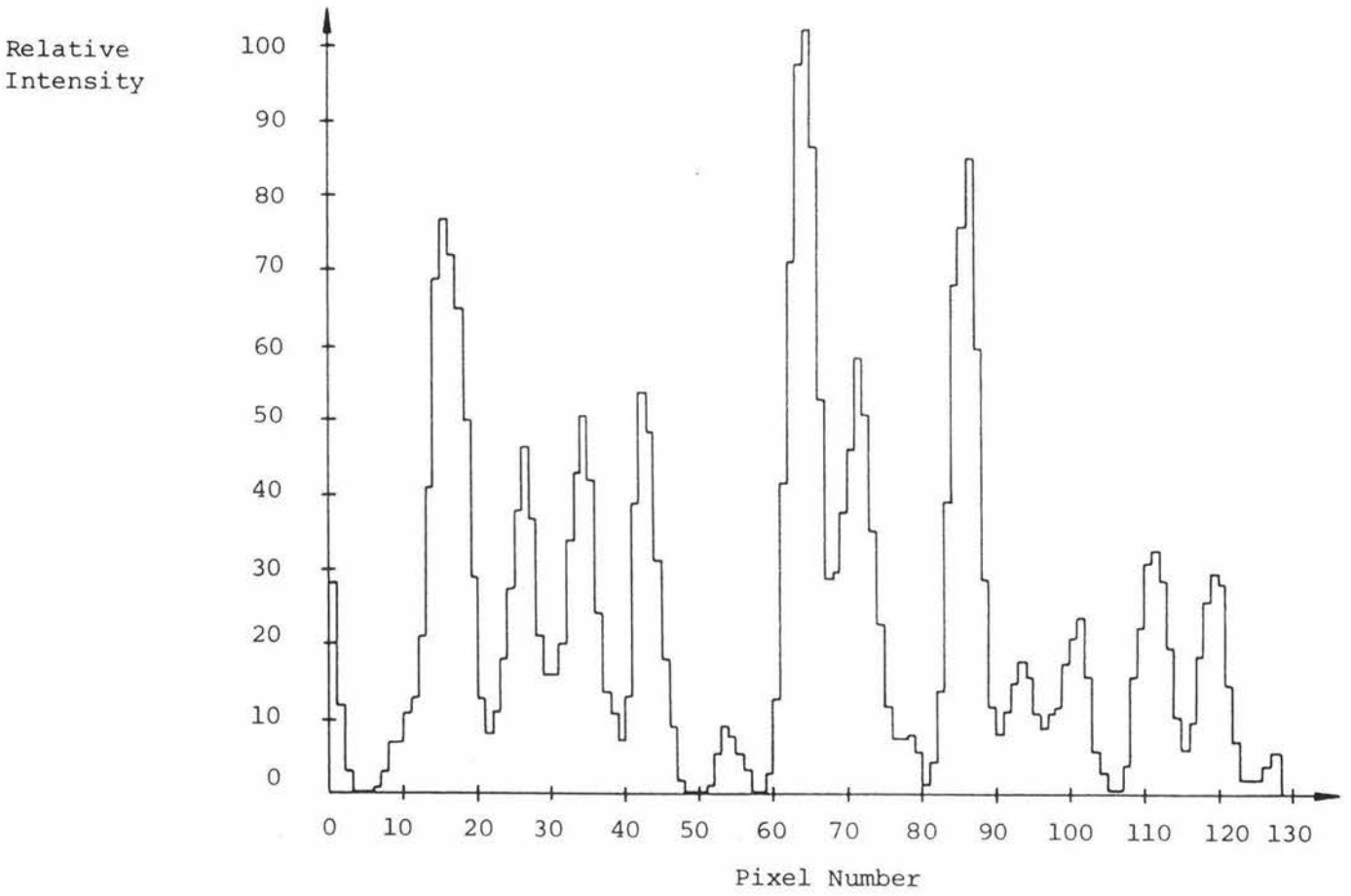

Figure 6.24 Speckle profile after displacement

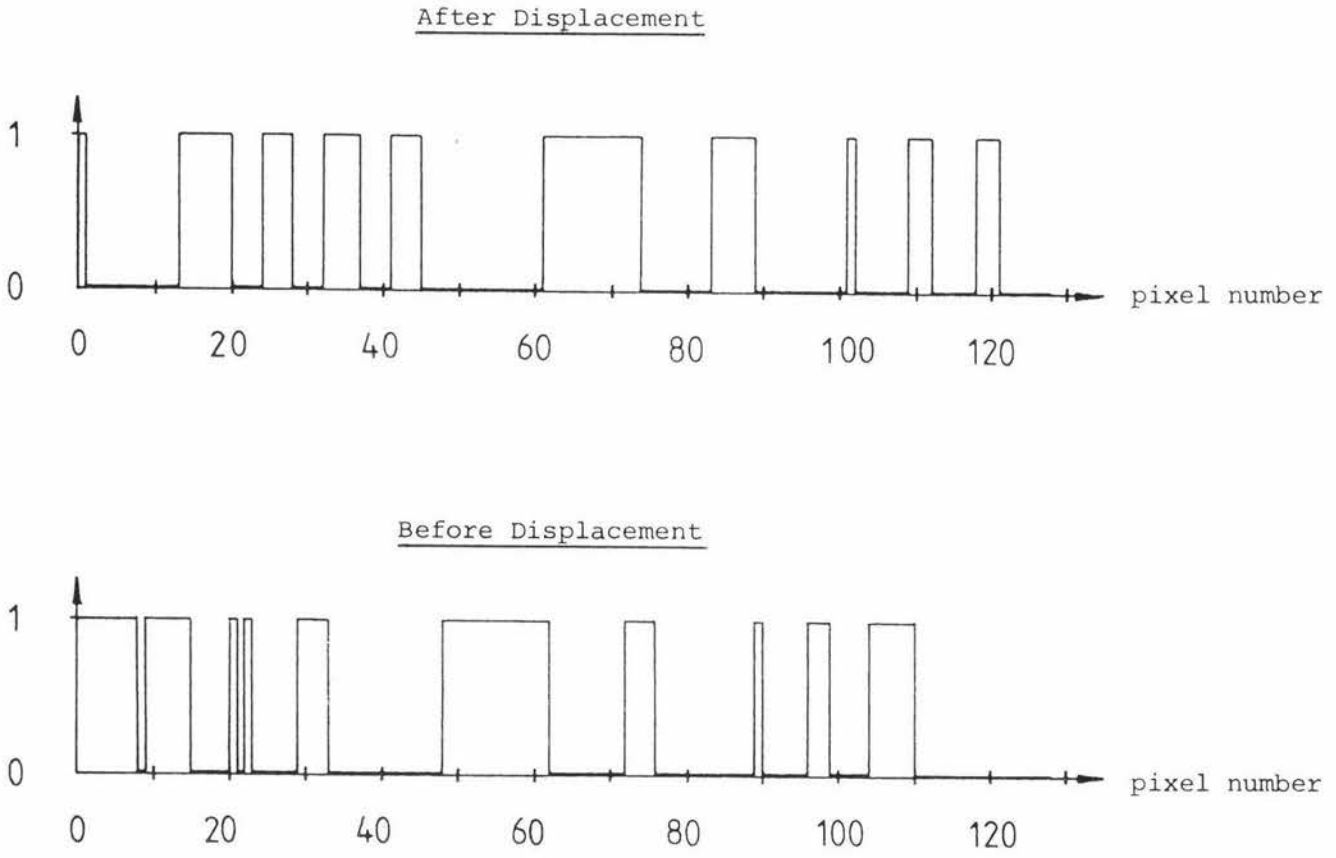

Figure 6.25 Clipped results

v) The process in step (iv) is repeated but this time pixels 20 to 107 in M4b are multiplied by pixels 1 to 88 in M4a. The resultant product-sum is the clipped, cross-correlation coefficient for lag -19.

vi) The above process is continued until all cross-correlation coefficients from lag -20 to lag +20 are obtained. A subroutine then determines the lag at which the correlation coefficient is greatest. This corresponds to the average displacement of the shifted speckle pattern. Figure 6.26 shows the cross-correlation coefficients obtained from the clipped data in figure 6.25. From these results we can see that the maximum correlation has occurred at lag +12 which corresponds to a speckle displacement of 12 × 32 = 384 μm (since adjacent, active pixels are 32μm apart).

Note that the data in figures 6.23 and 6.24 has rather a large number of zero intensities. This was caused by the array's thermal drift problem mentioned earlier. When the unit is first switched on, the dark level is below the lowest level (∿-0.5V) which can be accepted by the A/D converter. The data in figures 6.23 and 6.24 was collected under just such conditions. Although a problem when obtaining probability densities thermal drift caused few difficulties when measuring displacements.

A maximum lag of ±20 was chosen because of the limited number of data points available (128). Any larger lags would have produced erroneous results because of the limited region of correlation between the two samples. Larger arrays would of course allow much larger lags thereby increasing the precision and range of the displacement measurements. (E.g. a 1024 pixel array would allow a maximum lag of ±160 if the above criterion were used).

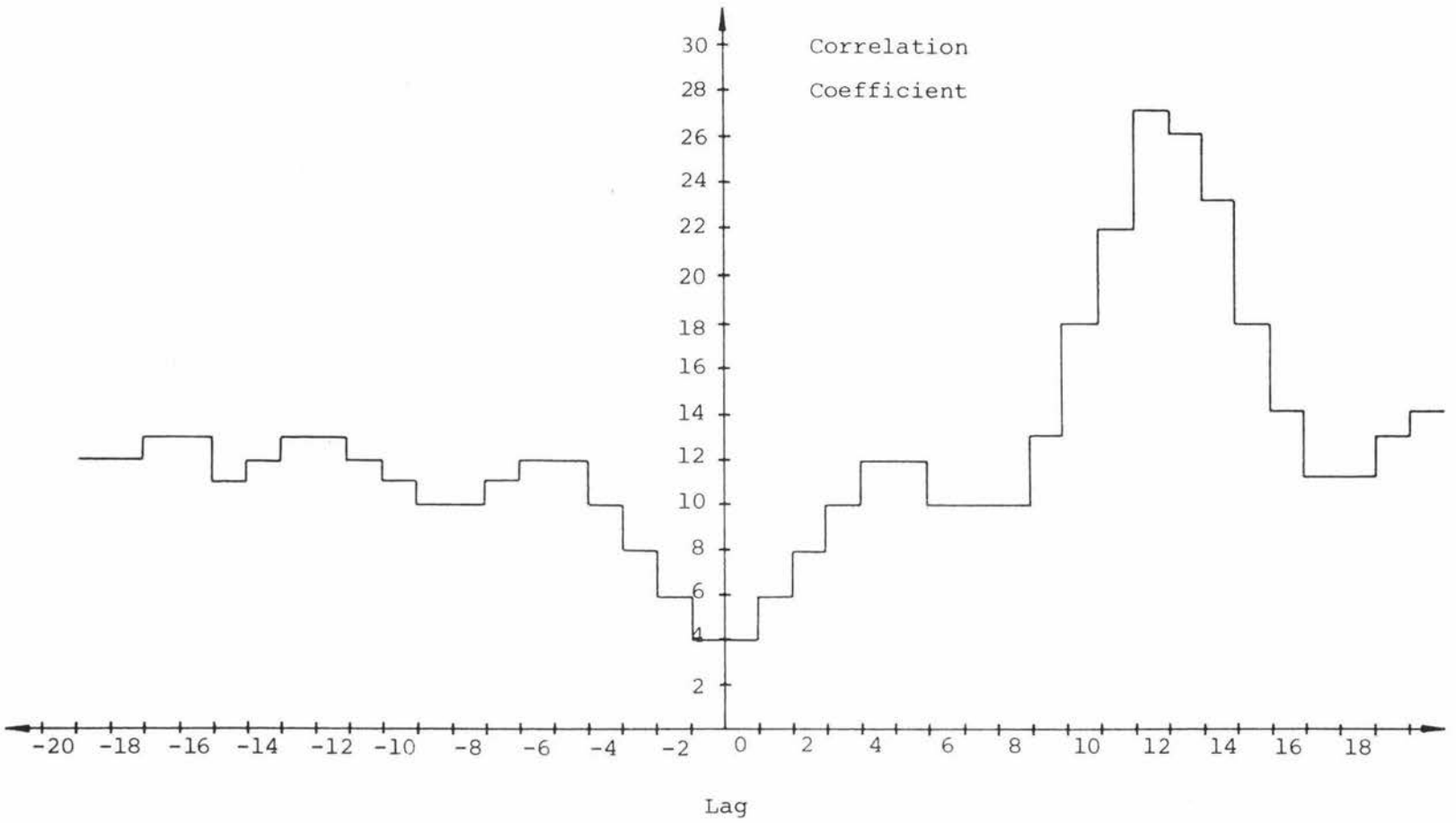

Figure 6.26 Cross-correlation coefficient as a function of lag

Step (iii) in the above notes is not essential as results can be obtained by simply multiplying the pixel intensities together. However the time required to perform the average multiplication of two 1 byte numbers is around 5ms; against 8μs for the AND instruction used in the clipping correlator. After adding additional instructions the clipping correlator runs about 30 times faster than the unclipped version, allowing displacement measurements to be made in a tolerable 1 or 2 seconds. The information lost by clipping did not seem to affect the correlator's ability to measure displacements in any significant manner.

6.10 Experimental Results Obtained when Measuring Surface Displacements

The apparatus used in this experiment is illustrated in figure 3.11. Light from the laser falls directly onto the translating stage and the resultant speckle pattern is monitored by the array. Results were first obtained for a displacement of 150μm at various distances from the array. This was done to check the assumption (made by many workers in speckle) that the speckle pattern moves with the object. A number of measurements were made at each distance and from these results a mean and standard deviation were calculated. The results are tabulated below.

Table 6.9 Speckle displacement as a function of object-array distance

Object Array Distance (mm)	Lag for Maximum Correlation	Mean	Displacement (μm)
100 ± 2mm	7,6,5,5,6,5	5.7±0.8	182±26
200	8,7,7,6,6,7,7	6.9±0.7	221±22
300	9,7,7,8,7,7	7.5±0.8	240±26
400	10,7,8,8,9,6	8.0±1.4	256±45
500	8,10,9,9,9,9	9.0±0.6	288±19
600	11,9,10,12,9,10	10±1	320±32
700	11,14,13,11,10,13,11,11	12±1	384±32

The displacement listed here is calculated by multiplying the mean lag by 32μm. This is the speckle displacement as measured by the array.

The results in table 6.9 have been graphed in figure 6.27 with a least squares best fit of

$$\Delta x = (0.30\pm0.02)\times L+(150\pm30), \qquad (6.8)$$

where the measured displacement (Δx) is in μm and the object-array distance (L) in mm.

Although this result indicates that the measured displacement increased as the object-array distance is increased, it does show that the speckle displacement at the object is the expected 150μm.

One possible reason for the increase in speckle displacement with distance can be obtained by considering the following model of speckle formation.

In the transmission speckle pattern pictured in figure 2.14 the object may be represented by a large number of randomly placed apertures, each having a diameter of the same order as the correlation length T. The speckle pattern to the right of the object will be formed by the coherent superposition of all the diffraction patterns produced by these apertures.

Consider now a single aperture, and its diffraction pattern. A parallel beam of coherent light with a diameter much greater that the aperture size, will produce a diffraction pattern, which moves as the aperture moves (see figure 6.28). However, if a diverging beam is used, movement of the aperture will produce a greater displacement in the diffraction plane. The reason for this phenomenon may be seen in figure 6.29. From this diagram we see that the displacement of the diffraction pattern is given by the formula

$$\Delta x = D(1 + \frac{L}{b}), \qquad (6.9)$$

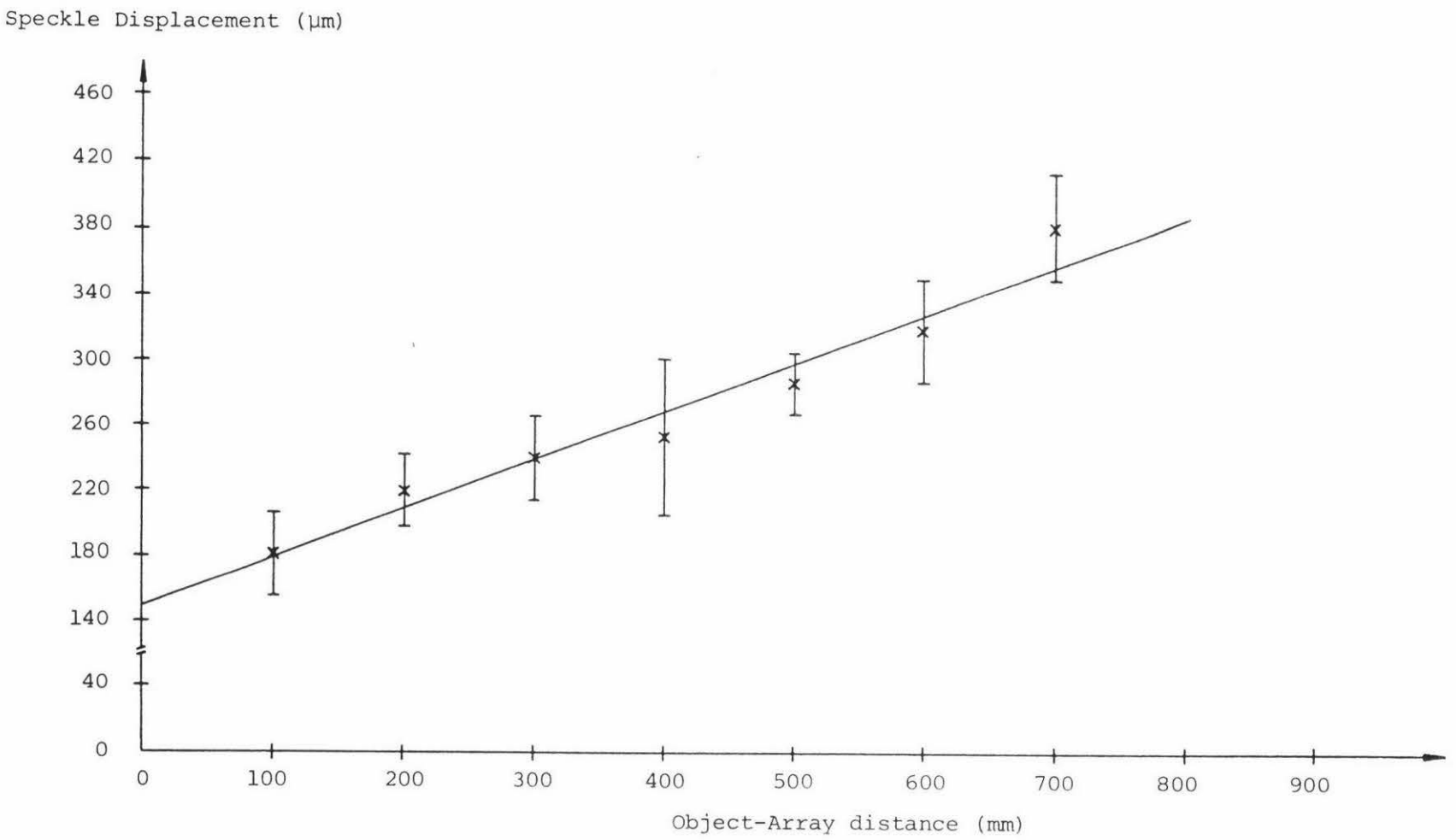

Figure 6.27 Speckle displacement vs. object-array distance

Figure 6.28 Collinear illumination of an aperture

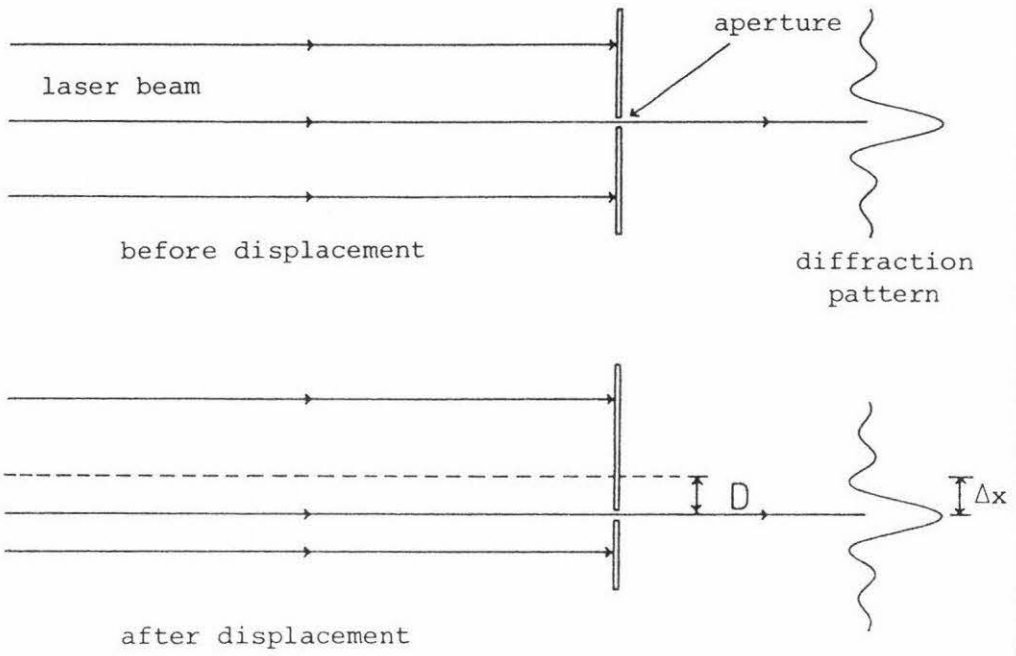

Figure 6.29 Divergent illumination of an aperture

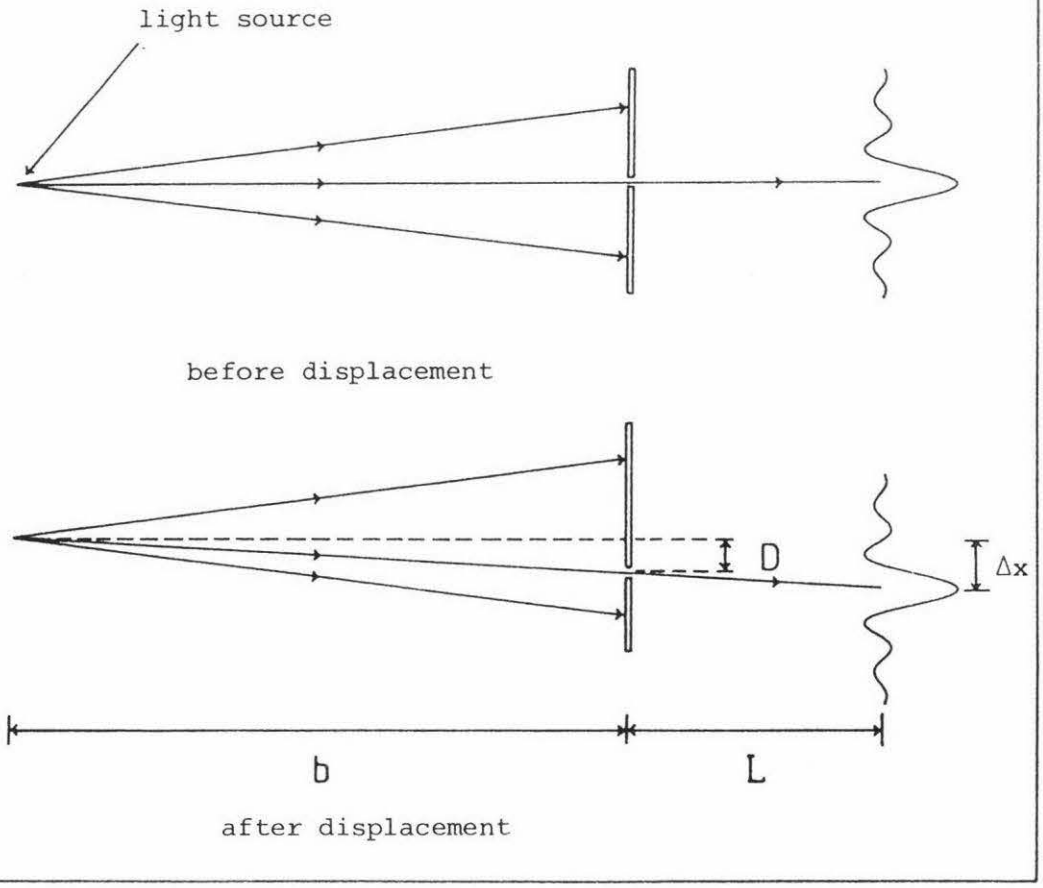

where D is the distance moved by the aperture, L the aperture to image distance, and b the distance from the light source to the aperture.

This result will also be correct when all apertures are considered. It will then represent the displacement of the speckle pattern as a function of object movement and object-array distance.

To test the relationship given in equation 6.9 the apparatus pictured in figure 3.12 was used. Light from the laser was expanded by lens L_1 to produce a spot approximately 1.5mm in diameter on a piece of ground glass, which was attached to the edge of the rotary stage. The resultant speckle pattern was then monitored by the array. A more detailed diagram showing all relevant measurements may be found in figure 6.30. From this diagram the light source to object distance can be seen to be 22±1mm. In deriving this result it has been assumed that the laser's slight beam divergence, of 1.2mrad, has little effect on the focal point of lens L_1.

From figure 3.6 we saw that the lever arm on the rotary stage was 115mm long. This means that for every 1mm of movement by the micrometer the glass object will move 66/115mm. This corresponds to a demagnification factor of 0.57. With these results we can now substitute into equation 6.9 to find Δx.

$$\Delta x = D(1+\frac{239\pm1}{22\pm1}) = D \times (11.9\pm0.5), \qquad (6.10)$$

but since $D = M \times (0.57\pm0.01)$, where M is the micrometer displacement, we have

$$\Delta x = M \times (0.57\pm0.01)\times(11.9\pm0.5) = M\times(6.8\pm0.3). \qquad (6.11)$$

The experimental values of speckle displacement (Δx) obtained for various micrometer displacements (M) are tabulated below along with the expected results from (6.11).

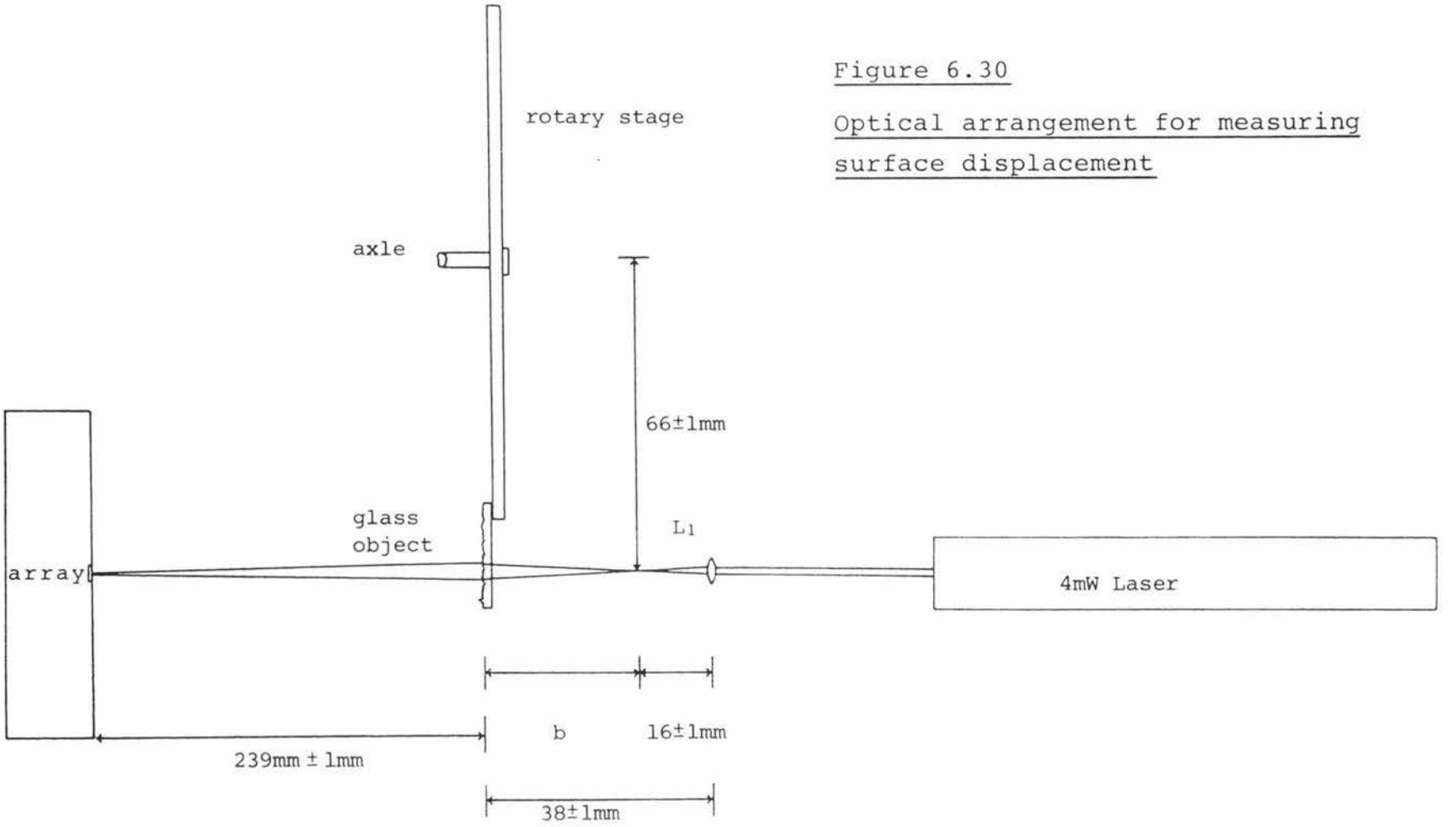

Figure 6.30

Optical arrangement for measuring surface displacement

Table 6.10 Measurement of speckle displacement

Micrometer Displacement (μm)	Mean Lag	Experimental Δx (μm)	Expected Δx (μm)
0	0	0	0
10	2.3±0.6	74±19	68±6
20	4.0±0.0	128±0	136±12
30	6.3±0.3	202±10	204±18
40	8.3±0.6	266±19	272±24
50	9.8±0.3	314±10	340±30
60	12.7±0.6	406±19	408±36
70	15.0±0.0	480±0	476±42
80	16.7±0.6	534±19	544±48
90	18.7±0.6	598±19	612±54

Notes

1. The mean lag was derived from 3 separate measurements. Those with zero error gave identical results on each run.

2. The experimental value of Δx is obtained from the mean lag by multiplying by 32μm.

The results in table 6.10 have been plotted in figure 6.31 with a least squares best fit of

$$\text{Speckle displacement} = (6.7\pm0.1)\times M+(-1\pm17). \qquad (6.12)$$

A result consistent with the values given in equation 6.11.

One interesting factor which is evident when figures 6.27 and 6.31 are compared is the smaller errors that have arisen when the rotary stage is used. This was typical of all measurements made with this device, which had a noticeably smoother action than the translating stage.

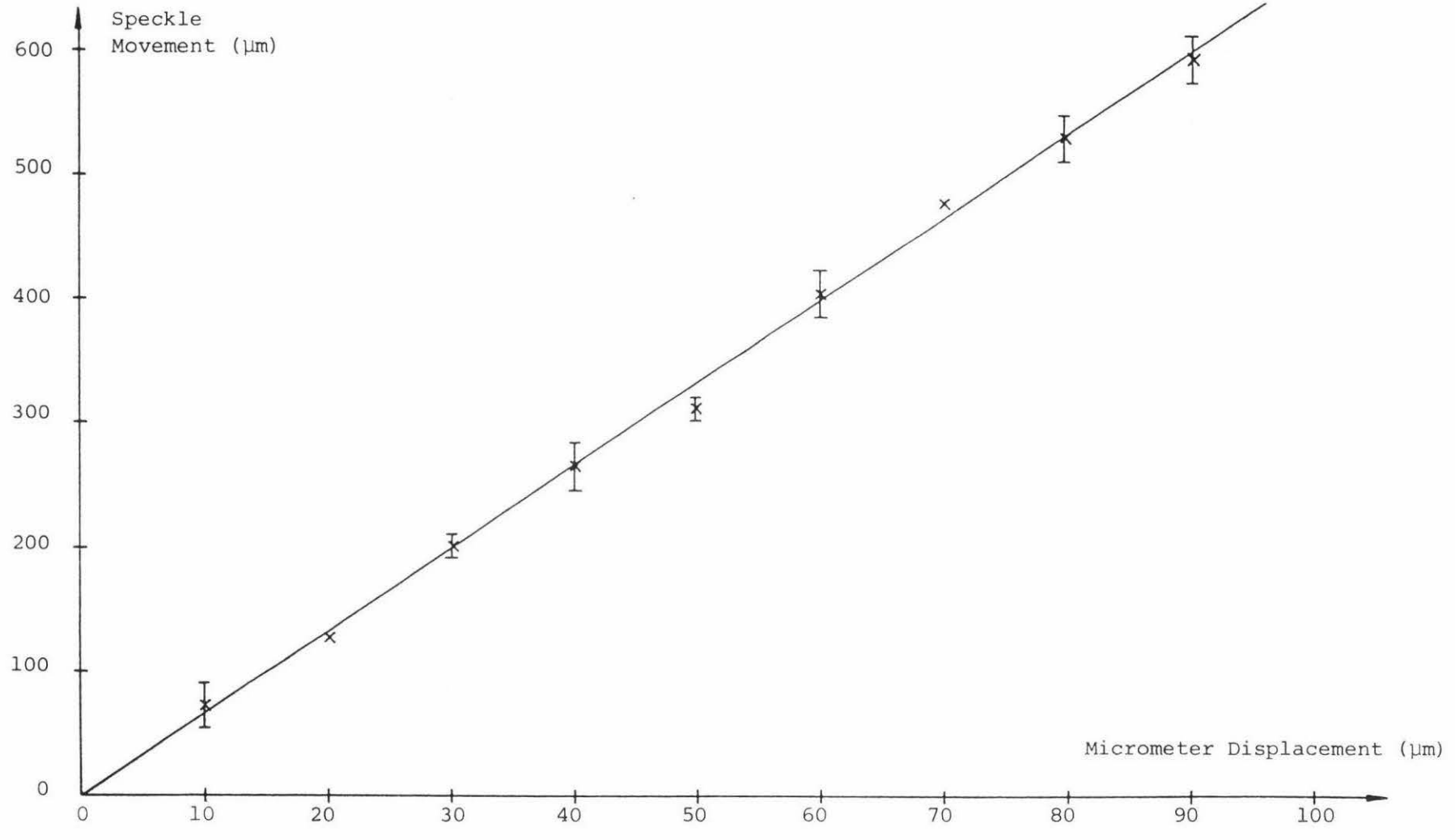

Figure 6.31 Speckle displacement as a function of micrometer movement

The uncertainty in Δx can be reduced still further by increasing the spot size on the object. A larger spot means that less speckle decorrelation will occur as the object is moved. The upper limit to spot size is dependent on the following two factors.

i) As the spot size is increased speckle size decreases. If speckles become smaller than a few pixel lengths consistent cross-correlation results will no longer be obtainable.

ii) When the rotary stage is moved, significant variations in the displacement D will occur across a large spot. This will lead to decorrelation of the speckle pattern because different speckles will move different distances.

With both these factors considered, the optimum spot size was found to be around 3.5mm. This was obtained by placing lens L_1 71mm from the object. The results plotted in figure 6.32 were obtained using this spot size along with an object-array distance of 250mm. The lack of error bars in the graph may be understood by determining the relationship between M and the expected mean lag for this arrangement. From equation 6.9 we have that

$$\Delta x = D(1 + \frac{L}{b}). \qquad (6.13)$$

Now

$$L = 250\pm1\text{mm}$$
$$b = (71\pm1)-(16\pm1) = 55\pm1\text{mm}.$$

Therefore

$$\Delta x = D\times(5.55\pm0.08), \qquad (6.14)$$

but

$$D = M \times (0.57\pm0.01). \qquad (6.15)$$

Figure 6.32 Micrometer displacement vs. lag

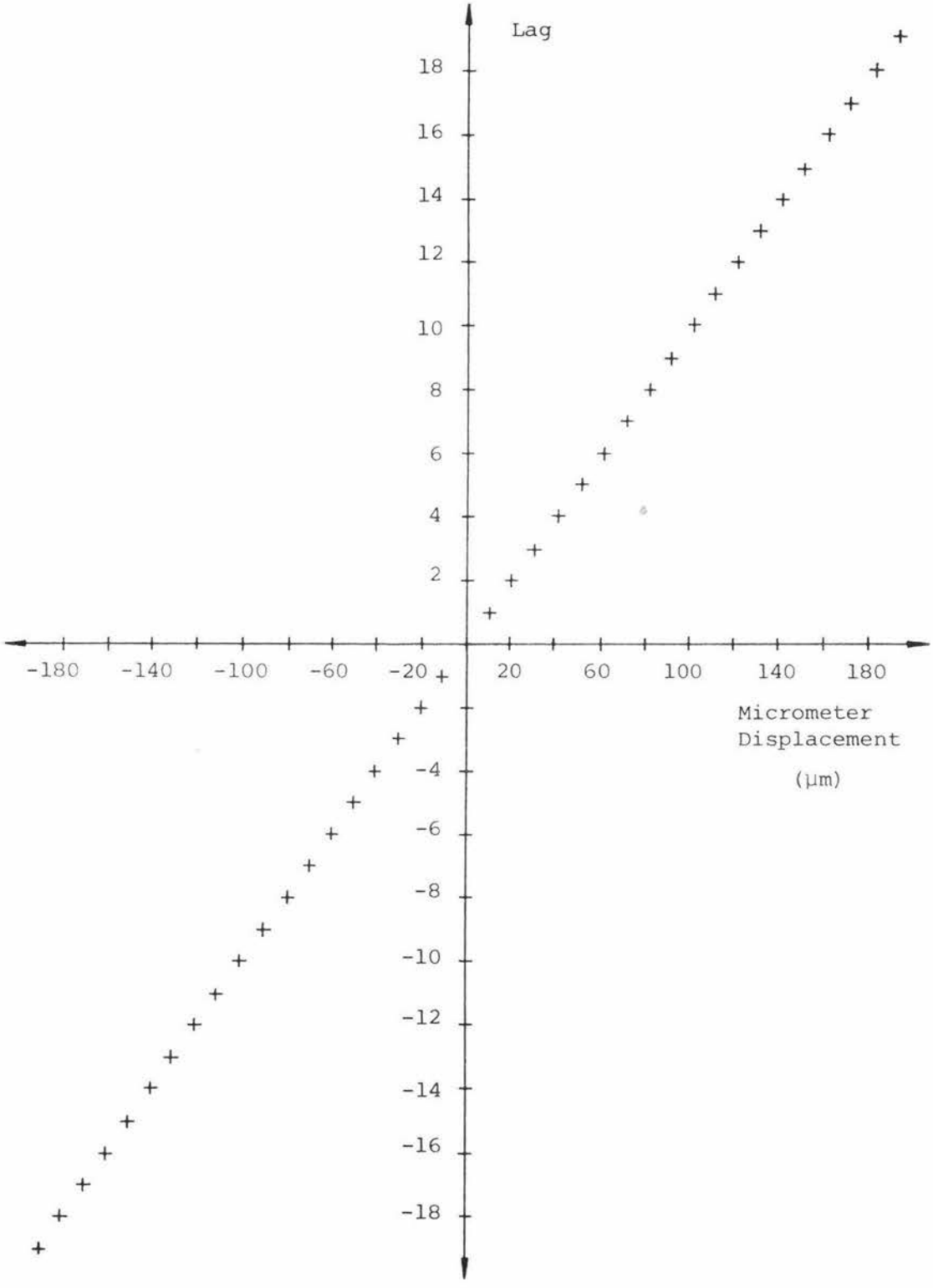

Therefore

$$\Delta x = M\times(3.16\pm0.07). \tag{6.16}$$

But since Lag = $\Delta x/32\mu m$ we have that

$$\text{Lag} = M\times(0.099\pm0.002\mu m^{-1}). \tag{6.17}$$

This expression is in close agreement with the experimentally observed results which from figure 6.32 give

$$\text{Lag} = M\times(0.1\mu m^{-1}). \tag{6.18}$$

For micrometer displacements which are multiples of 10μm the expected lag will, from equation 6.17, be close to an integer. Since lag is a discrete quantity the measured lag for each of these micrometer displacements will always be the same and so no errors will be observed. If measurements had been made with micrometer displacements that were not multiples of 10μm a maximum uncertainty of ± ½ lag would have resulted.

The results obtained in the last two experiments were made by detecting light scattered perpendicular to the surface. Experiments were also carried out by observing the speckle patterns produced by scattering light at oblique angles from metal surfaces. The results obtained were rather surprising as they did not agree with the predicted expressions obtained from equation 6.9.

Observation of speckle patterns produced using the translating stage showed that although speckle displacement was not a function of incidence or scattering angles, it did seem to be consistently larger than expected. The expected results for the data given in table 6.9 will now be derived as an example of this effect. Figure 6.33 shows the experimental arrangement. The relevant apparatus measurements are listed below.

Figure 6.33 Surface displacement measurement using the translating stage

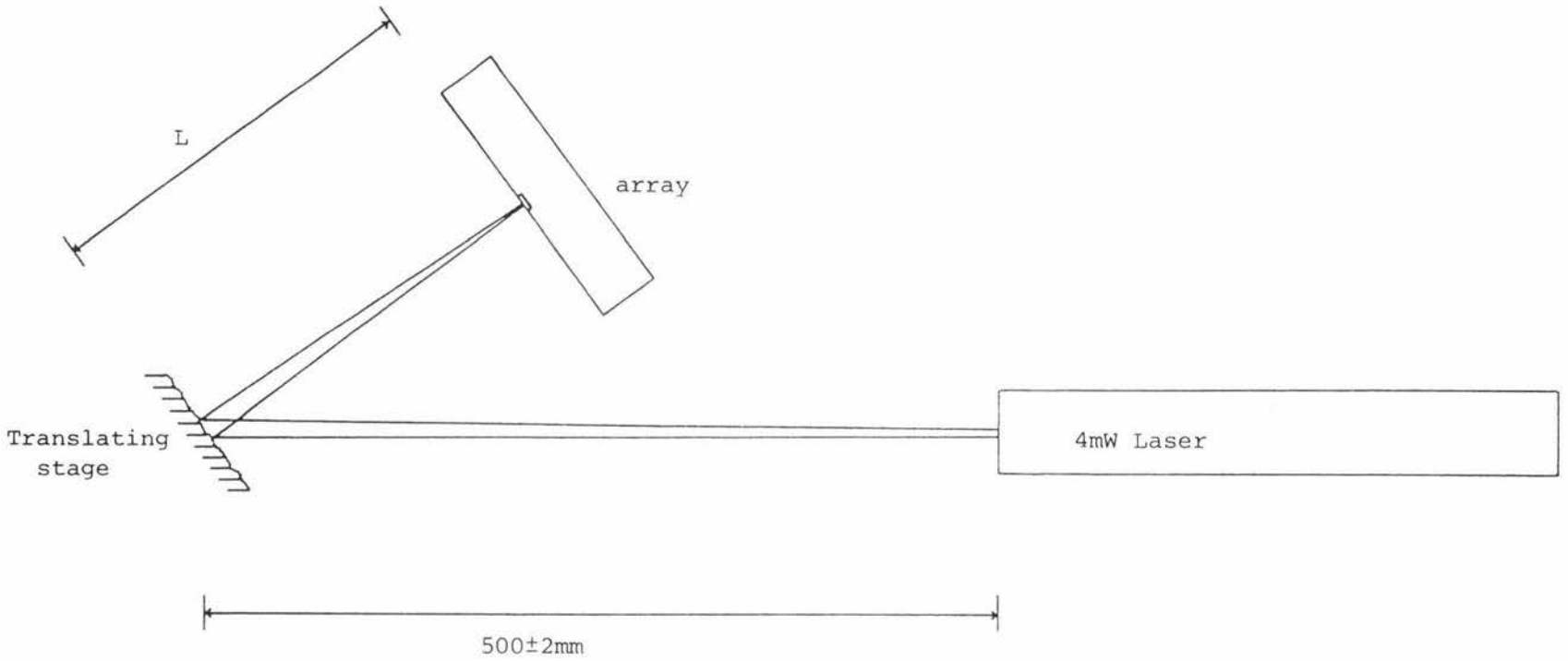

i) Effective light source-to-object distance;
$b = 500\pm2\text{mm} + 0.75/1.16\times10^{-3} = 1147\pm2\text{mm}$,
where 1.16×10^{-3} is the divergence of the laser beam in radians, and 0.75 is the beam diameter at the laser in millimetres.

ii) Object-array distance (L) ; from the results in table 6.9.

iii) $D = M = 150\mu m$.

With these figures it is now possible, using equation 6.9, to determine the relationship between speckle movement (Δx) and micrometer displacement (M).

$$\Delta x = M\times(1+\frac{L}{1147\pm2})$$

$$= (150\pm5)\times(1+\frac{L}{1147\pm2})$$

$$= (0.131\pm0.004)\times L+(150\pm5)\mu m. \qquad (6.19)$$

This result can be compared with equation 6.8 which was obtained experimentally i.e.

$$\Delta x = (0.30\pm0.02)\times L+(150\pm30)\mu m, \qquad (6.20)$$

where L is measured in millimetres.

Similar curious results were obtained when the rotary stage was used. Observation of the speckle pattern showed that it actually rotated as the micrometer was adjusted, despite the fact that all points within the illuminated area were moved in the same direction. Because of this rotation there were regions in the speckle pattern which experienced large positive displacements and others which underwent small negative shifts. Sections of the speckle pattern in the specular direction tended to simply decorrelate as the

object was moved. The following results using the arrangement in figure 6.34 were obtained by positioning the array in a region of large positive displacement.

Table 6.11 Measurement of speckle displacement using the rotary stage

Micrometer Displacement (μm)	Mean Lag	Experimental Δx (μm)	Expected Δx (μm)
0	0	0	0
50	4.0±0.0	128±0	60
100	7.8±0.5	249±16	120
150	11.5±0.6	368±19	180
200	15.8±0.5	506±16	240
250	19.8±0.5	634±16	300

The mean lag has been calculated from five separate measurements while the expected speckle displacement has been obtained from the data in figure 6.34 and equation 6.9.

Here the experimental best fit has the form (see figure 6.35)

$$\Delta x = M\times(2.53\pm0.03)+(-1.5\pm9.7)\,\mu m, \qquad (6.21)$$

while the theoretical result is quite different with

$$\Delta x = M\times(1.2\pm0.1)\,\mu m. \qquad (6.22)$$

No reasonable explanations have been found for these anomalous results although it seems likely that the small range of displacements which occurred in the illuminated area of the rotary stage contributed to the observed phenomenon in the second case.

More comprehensive tests, including measurement of surface displacement as a function of scattering and incidence angles, as well as a more reliable translating stage, could be useful in providing a solution to these problems.

Figure 6.34 Surface displacement measurement using the rotary stage

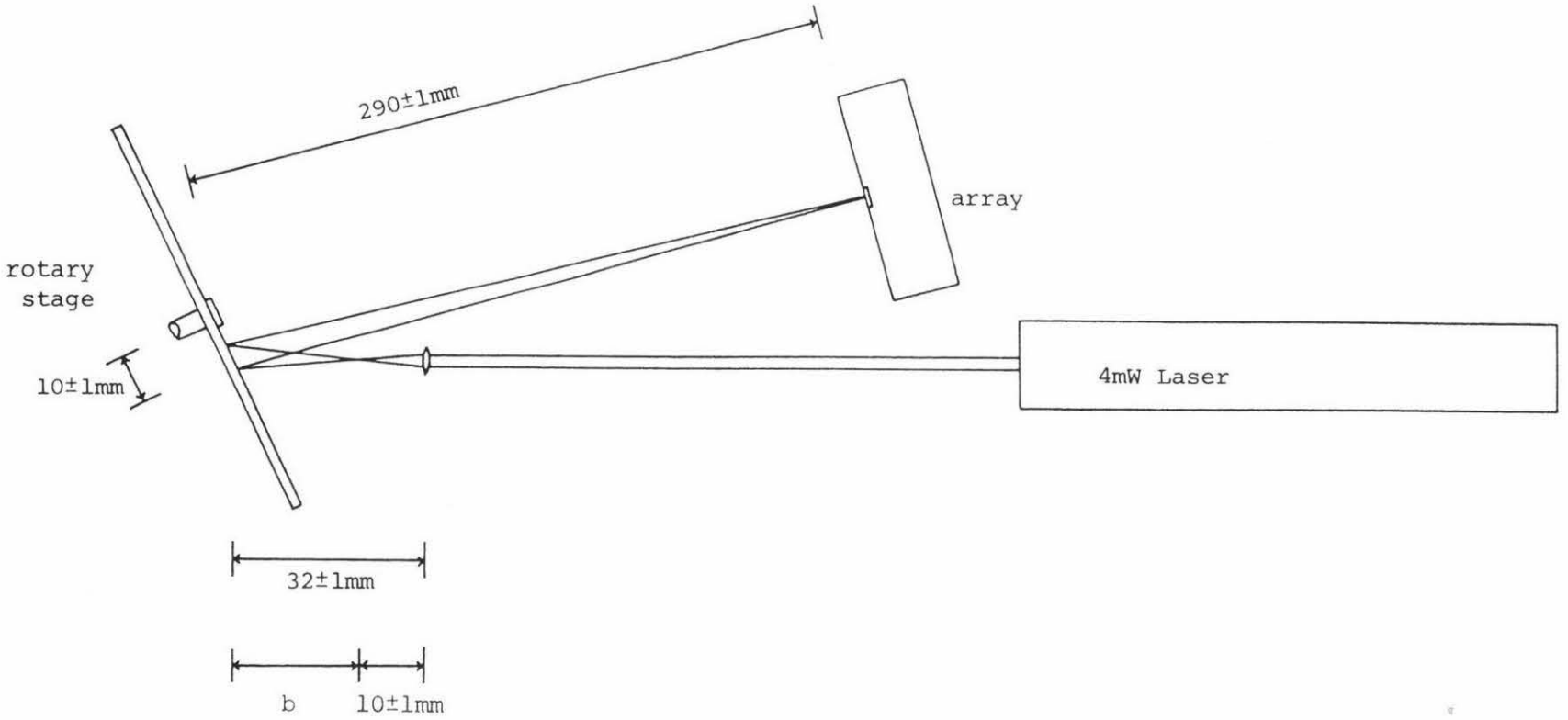

Figure 6.35 Speckle displacement vs. micrometer displacement

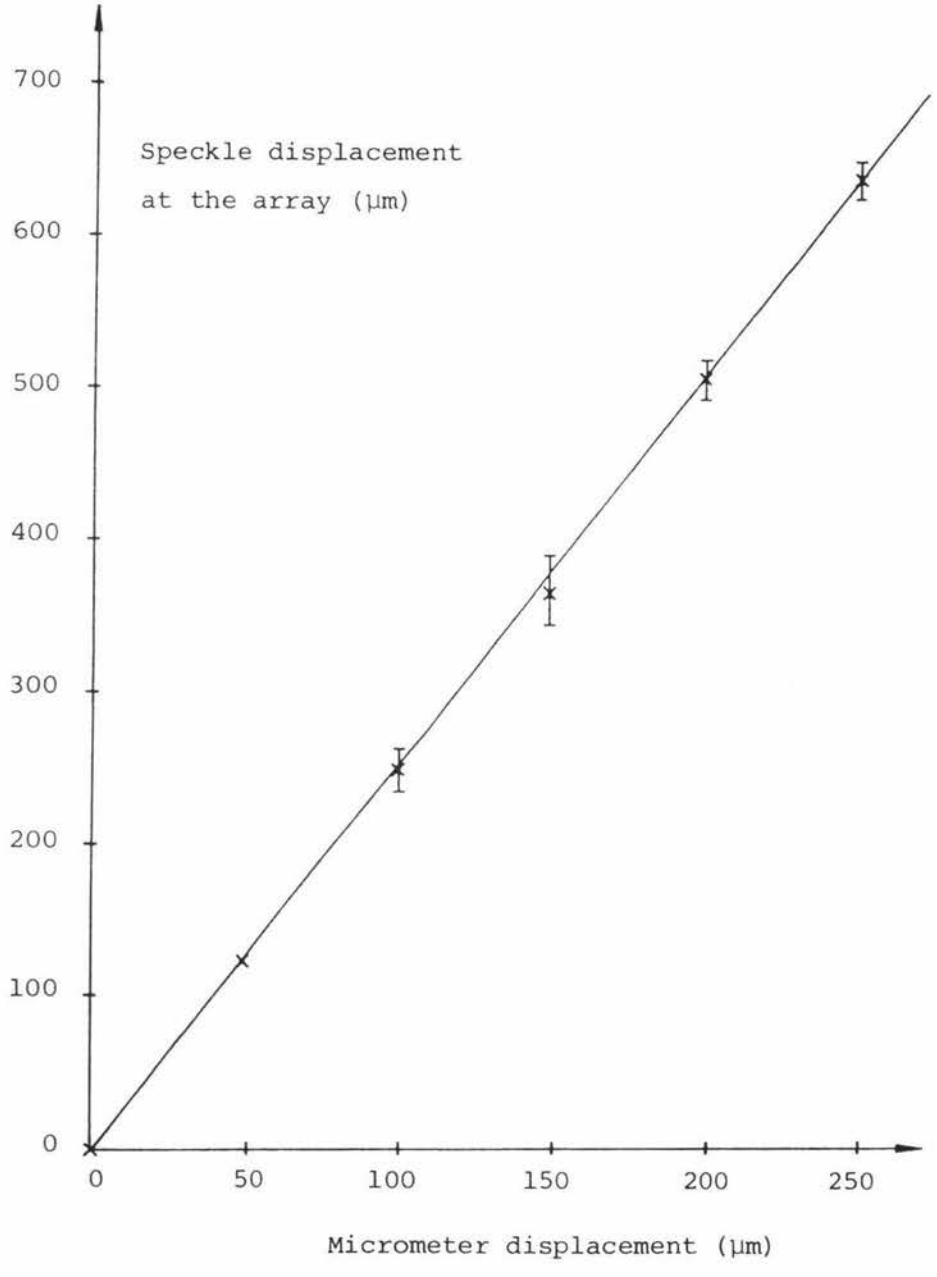

Despite these difficulties, which are purely theoretical, the array does appear to be well suited to making in-plane displacement measurements over a reasonably wide range. From table 6.11, we saw that a surface displacement of 1μm will produce a lag of 1. Even smaller displacements could be detected by reducing the value of b. As mentioned in section 6.9 improvements in the measurement range could also be brought about by increasing the number of pixels and their resolution. (The present unit has pixels spaced on 32μm centres while the non-malfunctioning device has responsive pixels every 16μm.) Large displacements (>0.5mm) are somewhat more difficult to measure because of the speckle decorrelation which occurs when the object is moved too far. Illuminating large areas on the surface could solve this problem but because of the decrease in speckle diameter which would result, some form of limiting aperture would have to be introduced to optimize the pixel-to-speckle size ratio. For large spot sizes (>1cm) a high powered laser would also be required to offset the attenuating effect of the aperture.

To investigate the array's usefulness in the monitoring of real (non-test) object displacement, the laser was shone directly onto the leaf of a plant. Over most of the leaf the resultant speckle pattern was observed to slowly decorrelate with time, indicating movement of the surface in a direction which was not parallel with the array. Light scattered from the stem, which was oriented parallel to the array's aperture, produced a speckle pattern which moved slowly across the array with little decorrelation.

It can be envisaged, that with little change to the existing displacement program and apparatus, that the movement of any suitable plant could be monitored by recording the speckle pattern at discrete time intervals. From this data the rate of plant growth at that point could then be determined.

6.11 Measurement of Speckle Size

The average size of laser speckle was first considered in section 2.7 where it was found that the objective speckle should have a mean width from adjacent minimum to minimum of

$$2\delta = \frac{2.44\lambda L}{n'd}. \qquad (6.23)$$

To check on the validity of this formula, and the model which produced it, speckle size was measured experimentally using a simple visual inspection of the array output and an autocorrelation program. The speckle intensity profile pictured in figure 6.9 was used as the test scan.

By simply determining the width of each speckle in this figure and then averaging, the following result was obtained.

$$2\delta = 13\pm3 \text{ pixel widths} = 416\pm96\mu m.$$

This process tended to be fairly tedious and so a program was written which would do this automatically by determining the autocorrelation function for the speckle pattern. The lag at which the function drops to its first mimimum corresponds to half the average width of the speckles.

The autocorrelation program used was designed along similar lines to the cross-correlation program discussed in the last section, except that only one scan was considered. Once loaded this data was then multiplied by itself at various lags to produce 40 autocorrelation coefficients from lag -20 to lag +20. The data was not clipped as speed was not essential in this experiment. The autocorrelation coefficients for the data in figure 6.9 have been calculated and normalized to lag zero. The results are pictured in figure 6.36.

From this figure we see that the width of the central maximum is 14±1 lags if we take 1 lag as being the uncertainty

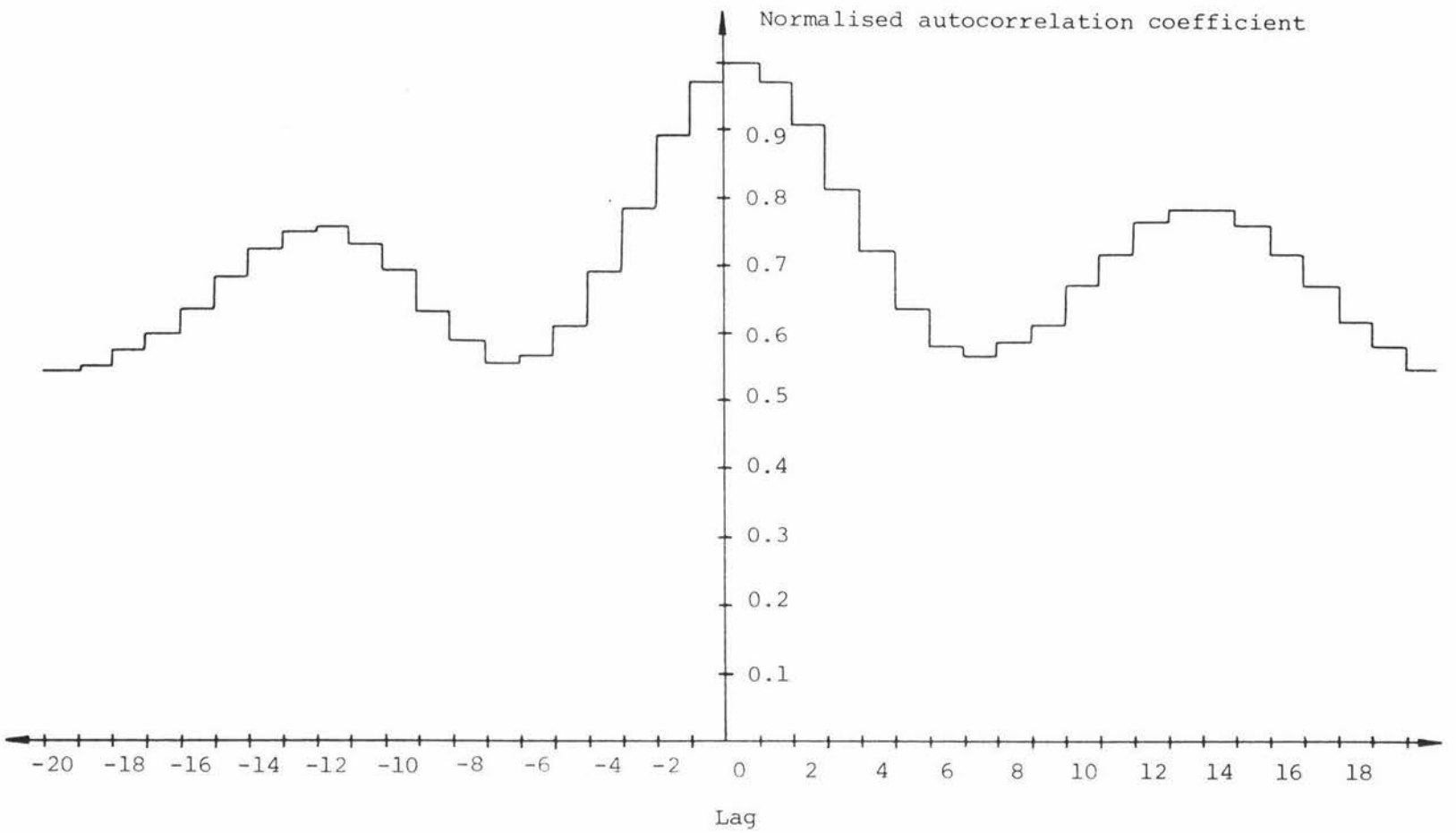

Figure 6.36 Autocorrelation function for determining speckle size

in the result. This corresponds to an average speckle size of

$$2\delta = 14\pm1 \text{ lags} = 448\pm32\mu m,$$

a result which compares well with the value obtained above. To check these two results against the formula in equation 6.23 we note that when this data was recorded, the apparatus pictured in figure 3.10 was used with an object-to-array distance (L) of 110±1mm and a spot size (as measured by a micrometer) of 0.40±0.01mm. With λ = 632.8nm this gives a speckle size of

$$2\delta = 425\pm11\mu m,$$

in good agreement with the values obtained previously, despite the fact that only 10 speckles were considered.

7. Project Summary and Conclusions

The major aim of this project, to investigate the usefulness of the charge-coupled array in the measurement of certain speckle statistics, has been largely met. To summarize and draw conclusions from this work the following five sections have been written covering each major piece of apparatus, and experiment.

7.1 The Linear, Charge-Coupled, Photodiode Array

A 256 element photodiode array was obtained along with driver boards and was used to collect intensity data from speckle patterns. Despite the fact that only 128 pixels were active the array was found to have adequate resolution, linearity, and sensitivity for the present task.

Problems arose in analysing the speckle data because of the need to preprocess the array output. The device showed significant amounts of thermal drift, zero-offset and pixel non-uniformity which had to be minimized before statistical analysis of the speckle data could take place. To achieve this two scans of the array were made, one in the dark and one exposed to the speckle pattern. By subtracting the dark signal, zero-offset and dark signal non-uniformity were removed. As pixel sensitivity proved to vary by as much as 10% across the array a compensation program was written which multiplied each pixel output by a correction factor. This procedure proved to be quite effective, reducing pixel non-uniformity markedly. Thermal drift remained a major difficulty as it limited the output range of the A/D converter, because $V_{max} - V_{min}$ (see figure 5.2) had to be increased to allow for signal drift. A properly functioning array with symmetrical video outputs would probably reduce thermal drift significantly.

For some of the experiments (displacement measurements in particular) the limited number of pixels reduced efficiency, but larger arrays (up to 1024 pixels) could be plugged into the unit, with only minor circuit changes, to alleviate this problem.

Once these factors had been taken into account the resultant processed output proved to be a reasonably accurate picture of the speckle intensity profile.

7.2 The Microcomputer

The computer used to control and analyse the output from the array was based on an 1802 Cosmac microprocessor. Video data was digitised by an 8 bit analogue-to-digital converter and then stored in the computer memory to await statistical analysis. The data was first corrected, in the manner described in section 7.1 and then manipulated by a number of specialised routines (described below) to obtain the desired parameters.

Considerable improvements could have been made to this device, but with the current availability of relatively cheap, sophisticated microcomputers this was not thought practical. Future research in this field will no doubt make use of one of these machines, allowing complex data analysis to be performed and presented, with far less effort on the part of the experimenter.

7.3 Optical Components

The optical components used in this project were generally fairly simple. Most of them could have been improved on immensely if more time and skilled labour had been available. The translating mount in particular caused many headaches, although an adjustable microscope stage, as used by Briers and Angus {ref 7.1}, would probably have provided a suitable solution.

Many of the difficulties encountered in this thesis were caused by the lack of a low powered polarized laser. The laser used, produced only partially developed speckle patterns which had statistics that were difficult to predict theoretically.

7.4 Surface Roughness Measurement

Light from the laser was shone obliquely onto a rough surface and the resultant speckle pattern was observed in the specular direction. As the incidence angle was adjusted the speckle contrast in this direction was found to vary. The ways in which it varied could, from theoretical considerations, be related to surface roughness and surface coherence length.

The results obtained were not considered particularly accurate for the following reasons.

i) The partially polarized laser tended to reduce contrast as $\theta \rightarrow 0$.

ii) Scattering and non-uniform spot illumination caused an increase in contrast at glancing incidence angles.

Improved optical componentry and a polarized laser would have solved these problems.

Unfortunately no standard surfaces with known roughness parameters were available. If these experiments were to be repeated it would be worthwhile obtaining a standard set so that the results could be checked for accuracy. Such a set is discussed by Reason {ref 6.1 p 627}.

7.5 Surface Displacement Measurement

Light from the laser was shone through a glass slide which had one side roughened. The resultant speckle pattern was monitored with the array oriented parallel to the object. As the object was moved the speckle pattern also moved, and once the divergence of the illuminating beam was known the displacement of the object could be determined. The measurement accuracy was limited by the number of pixels and their spacing. Both of these factors could be improved with larger arrays.

By adjusting various apparatus parameters, measurements from 1μm to 0.5mm were made. A larger range could have been obtained by using different optical components (lenses in particular).

When the rotary stage was used accuracy was found to be very good, a 2.5% uncertainty being observed at the maximum measurable displacement. Agreement with theoretical displacements was also found to be excellent. As noted in section 7.3 the translating stage caused many difficulties producing results which were far from consistent.

When measurements were made with reflection speckle patterns the resultant speckle displacements were found to disagree with the theoretically predicted results. More work on the theory of speckle displacement would appear necessary in this case to explain this curious phenomenon.

All in all the results produced using the speckle displacement technique were very pleasing and it is in this field that the array would appear to have the greater potential.

7.6 Uses of the Array made by Other Workers in Speckle

The theory and experiments described in this thesis are based on the work of some of the earliest researchers who

studied speckle. The variety of possible laser speckle applications is continuously growing; improved methods of measuring surface roughness, displacement, and strain using speckle interferometry are already well developed, offering a wide variety of new situations to which the array could be applied. For detailed discussions on some of these techniques the interested reader is referred to the work of Francon {ref 7.2}.

To the author's knowledge only a handful of speckle experiments have been performed using a photodiode array. Costa et al. {ref 7.3} used a 64 element diode array in an interferometric experiment to measure thermal expansion of optically rough objects while Yamaguchi {ref 7.4} used a 1024 element array to measure surface strains. Both authors produced results which would seem to indicate the photodiode array has a promising future in this field.

APPENDIX A

Derivation of the Probability Density and Contrast for the Sum of Two Fully Developed Speckle Patterns

As mentioned in section 2.5 we may consider the partially polarized speckle pattern to be made of two overlapping fully developed patterns each of which will have an amplitude probability density given by equation 2.62 i.e.

$$p(A_i) = \frac{2A}{na_i^2} \cdot \exp\left(\frac{-A_i^2}{na_i^2}\right), \tag{A.1}$$

where the subscript i refers to either the x or y field components, (not to be confused with the real and imaginary components of each individual field).

If we assume that the two speckle patterns are uncorrelated and independent we can write

$$p(A_x,A_y) = p(A_x)p(A_y)$$

$$= \frac{4A_xA_y}{\langle I_x\rangle\langle I_y\rangle} \cdot \exp\left(\frac{-A_x^2}{\langle I_x\rangle} - \frac{A_y^2}{\langle I_y\rangle}\right), \tag{A.2}$$

since from equation 2.65

$$\langle I_i\rangle = 2\sigma_i^2 = na_i^2, \tag{A.3}$$

for a fully developed speckle pattern.

From figure 2.9 we saw that $A_x = A_T \cos\beta$ and $A_y = A_T \sin\beta$, so by changing the random variables to A_T and β we have, using the coordinate transformation

$$dA_xdA_y = A_TdA_Td\beta, \tag{A.4}$$

the result

$$p(A_T,\beta) = \frac{4A_T^3\cos\beta\sin\beta}{\langle I_x\rangle\langle I_y\rangle}\exp\left(-A_T^2\left(\frac{\cos^2\beta}{\langle I_x\rangle}+\frac{\sin^2\beta}{\langle I_y\rangle}\right)\right), \qquad (A.5)$$

and

$$p(A_T) = \int_0^{\pi/2} p(A_T,\beta)\,d\beta. \qquad (A.6)$$

If we let

$$W = \frac{\cos^2\beta}{\langle I_x\rangle}+\frac{\sin^2\beta}{\langle I_y\rangle}, \qquad (A.7)$$

then

$$dW = 2\cos\beta\sin\beta\left(\frac{1}{\langle I_y\rangle}-\frac{1}{\langle I_x\rangle}\right)d\beta$$

$$= 2\cos\beta\sin\beta\left(\frac{\langle I_x\rangle-\langle I_y\rangle}{\langle I_x\rangle\langle I_y\rangle}\right)d\beta, \qquad (A.8)$$

with these substitutions we have

$$p(A_T,\beta)\,d\beta = \frac{2A_T^3\,dW}{\langle I_x\rangle-\langle I_y\rangle}\cdot\exp(-A_T^2W), \qquad (A.9)$$

and therefore

$$p(A_T) = \frac{2A_T^3}{\langle I_x\rangle-\langle I_y\rangle}\int \exp(-A_T^2W)\,dW, \qquad (A.10)$$

where the limits of integration are from $\langle I_x\rangle^{-1}$ to $\langle I_y\rangle^{-1}$.

Upon integration, (A.10) simplifies to give

$$p(A_T) = \frac{2A_T}{\langle I_x\rangle-\langle I_y\rangle}\left(\exp\left(\frac{-A_T^2}{\langle I_x\rangle}\right)-\exp\left(\frac{-A_T^2}{\langle I_y\rangle}\right)\right), \qquad (A.11)$$

Finally, since $p(I_T)=\frac{p(A_T)}{2A_T}$ (from equation 2.64), we have the result

$$p(I_T) = \frac{1}{\langle I_x\rangle-\langle I_y\rangle}\left(\exp\left(\frac{-I_T}{\langle I_x\rangle}\right)-\exp\left(\frac{-I_T}{\langle I_y\rangle}\right)\right). \qquad (A.12)$$

This function is plotted in figure 2.10 as a function of

the ratio $I_x : I_y$.

Note that this solution does not produce intelligible results for $\langle I_x \rangle = \langle I_y \rangle = \langle I_T \rangle$.

In this case (A.5) becomes

$$p(A_T,\beta) = \frac{4A_T^3 \cos\beta \sin\beta}{\langle I_T \rangle^2} \exp\left(\frac{-A_T^2}{\langle I_T \rangle}\right), \qquad (A.13)$$

equation A.6 therefore has the solution

$$p(A_T) = \frac{2A_T^3}{\langle I_T \rangle^2} \exp\left(\frac{-A_T^2}{\langle I_T \rangle}\right), \qquad (A.14)$$

so that $p(I_T)$ is just

$$p(I_T) = \frac{I_T}{\langle I_T \rangle^2} \exp\left(\frac{-I_T}{\langle I_T \rangle}\right). \qquad (A.15)$$

Both (A.12) and (A.15) are identical to the results obtained by Goodman {ref 2.2 p 24} who used a somewhat different method in his derivation.

Now $\langle I_T^n \rangle$ will from (A.12) be

$$\langle I_T^n \rangle = \int_0^\infty p(I_T) I_T^n dI$$

$$= \frac{1}{a-b}\left(\int_0^\infty \exp\left(\frac{-I_T}{a}\right) I_T^n dI - \int_0^\infty \exp\left(\frac{-I_T}{b}\right) I_T^n dI\right), \qquad (A.16)$$

where $a = \langle I_x \rangle$ and $b = \langle I_y \rangle$.

These are standard integrals which give the solution

$$\langle I_T^n \rangle = n! \cdot \frac{a^{n+1} - b^{n+1}}{a-b}. \qquad (A.17)$$

Now since contrast is just

$$C = \frac{\sigma_I}{\langle I \rangle} = \frac{(\langle I^2 \rangle - \langle I \rangle^2)^{\frac{1}{2}}}{\langle I \rangle} = \left(\frac{\langle I^2 \rangle}{\langle I \rangle^2} - 1\right)^{\frac{1}{2}}, \qquad (A.18)$$

if we set $\langle I_T \rangle = \langle I_x \rangle + \langle I_y \rangle = a+b = 1$ we obtain the following result for n = 2

$$\langle I_T^2 \rangle = 2 \cdot \frac{a^3-b^3}{a-b} = 2 \cdot \frac{1-3b+3b^2-2b^3}{1-2b} \quad . \tag{A.19}$$

So that, after some long division, we obtain the expression

$$\frac{\langle I_T^2 \rangle}{\langle I_T \rangle^2} = \langle I_T^2 \rangle = 2(b^2-b+1), \tag{A.20}$$

which gives

$$C = (2b^2-2b+1)^{\frac{1}{2}} = (2\langle I_y \rangle^2 - 2\langle I_y \rangle + 1)^{\frac{1}{2}}. \tag{A.21}$$

An identical result may be obtained in terms of $\langle I_x \rangle$.
This particular function is plotted in figure 2.11.

APPENDIX B

Computer Memory Map

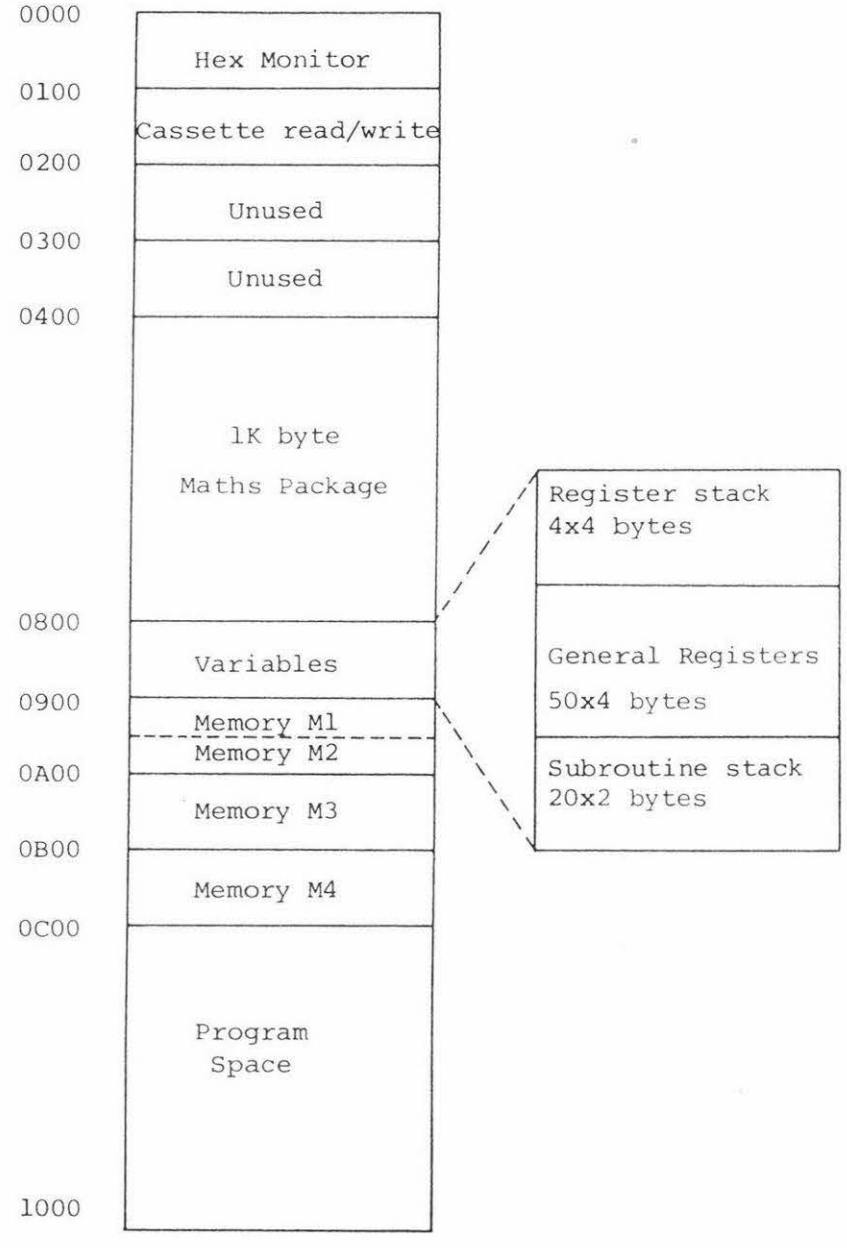

Memory Key

M1 = 128 bytes to accommodate the zero correction data produced by the dark scan.

M2 = 128 bytes to accommodate pixel intensity data, before and after correction.

M3 = 256 bytes of non-uniformity correction data (loaded from cassette).

M4 = 256 bytes to accommodate intensity distribution, and cross-correlation data.

APPENDIX C

Computer Simulations

Many of the experiments considered in this thesis involved factors which often obscured the ideal results. Computer simulation gives an experimenter the opportunity to test various theories without introducing these problems.

During the course of this project the author obtained a Commodore Pet microcomputer, based on the 6502 microprocessor. This computer was used to perform all complex calculations in this thesis which the 1802 microcomputer could not handle. A number of simulation programs† were also written for the Pet computer to investigate the various problems which arose in the theoretical and experimental parts of this thesis. These programs and their results will now be considered in more detail.

C.1 Simulation of a Fully Developed Speckle Pattern Intensity Distribution

Using the random walk model described in section 2.1 a program was written which produced a number of randomly oriented amplitude vectors which were added together, and then squared to produce a resultant intensity. This intensity level was noted and then the above process was repeated. After a predefined number of intensities had been produced and recorded the program calculated the mean, standard deviation, and contrast for the (pseudo) speckle pattern which could have produced this data. The intensity distribution was then displayed as a bar graph on the video monitor. Figure C.1 is an example of such a run which was made from 40000 intensity points each of which was derived from 50 randomly oriented vectors. (This particular program took 14 hours to run!) The statistics calculated from this data, using the techniques discussed in section 6.5, are listed on page 158.

† A complete listing of these programs is given in Appendix H.

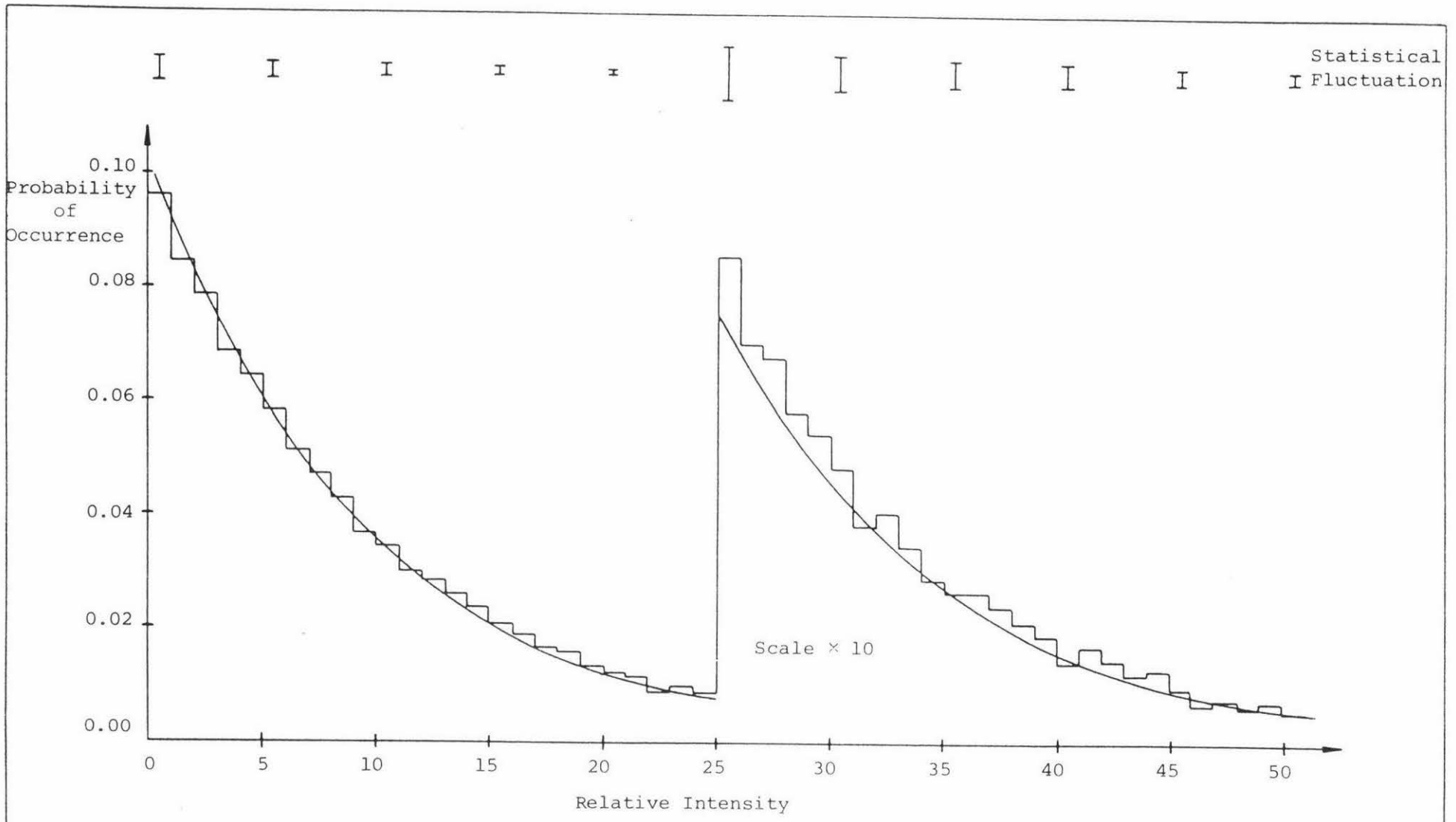

Figure C.1 Simulated probability distribution

Mean = 9.46
Standard Deviation = 9.89
Contrast = 1.05

As expected the contrast is close to unity. (A number of such simulations produced contrasts which ranged from 0.93 to 1.08).

Using the formula given in equation 6.7 the expected probability distribution was calculated. (Note that the limits a and b in this equation now become I-1 and I+1 respectively).

The reasonably close match between this result (represented by the smooth curve in figure C.1) and the simulated data indicates that equation 6.7 correctly describes the random walk intensity distribution.

C.2 Simulation of a Partially Developed Speckle Pattern Intensity Distribution

In situations where the speckle pattern is not fully developed (i.e. where $\sigma_\phi < \pi$) the equation which describes the probability density of speckle amplitude (equation 2.57) is very complex, and difficult to solve. However as pointed out by Beckmann {ref 2.1 p.12} such a speckle pattern may be formed by the vector sum of a random phasor and a constant amplitude vector r_c (see figure C.2). This has the effect of increasing the speckle's mean intensity but leaving the standard deviation unchanged. In other words the contrast is reduced, an effect which is observed experimentally.
To obtain some idea of the resultant intensity distribution a number of computer simulations were performed using just such a technique. Figures C.3 to C.9 show the results of these simulations for various values of r_c. These distributions, which have their statistics listed on page 167, show a close resemblance to those obtained experimentally in section 6.7.

Figure C.2 Random walk with constant amplitude phasor added

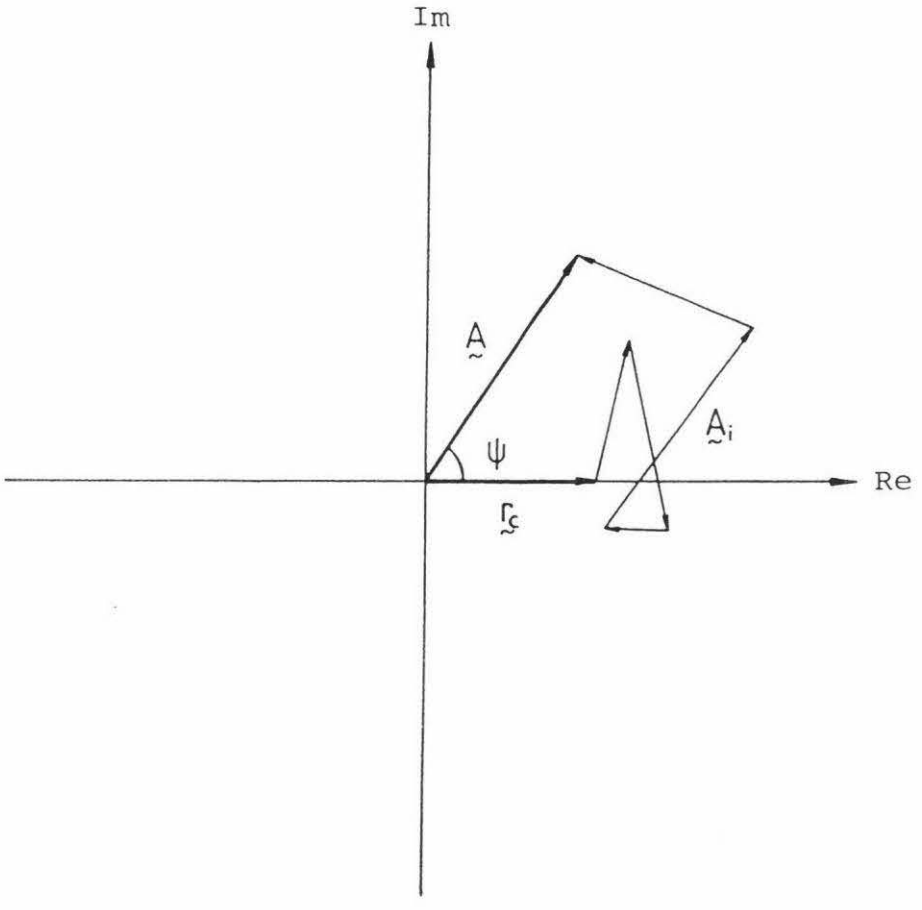

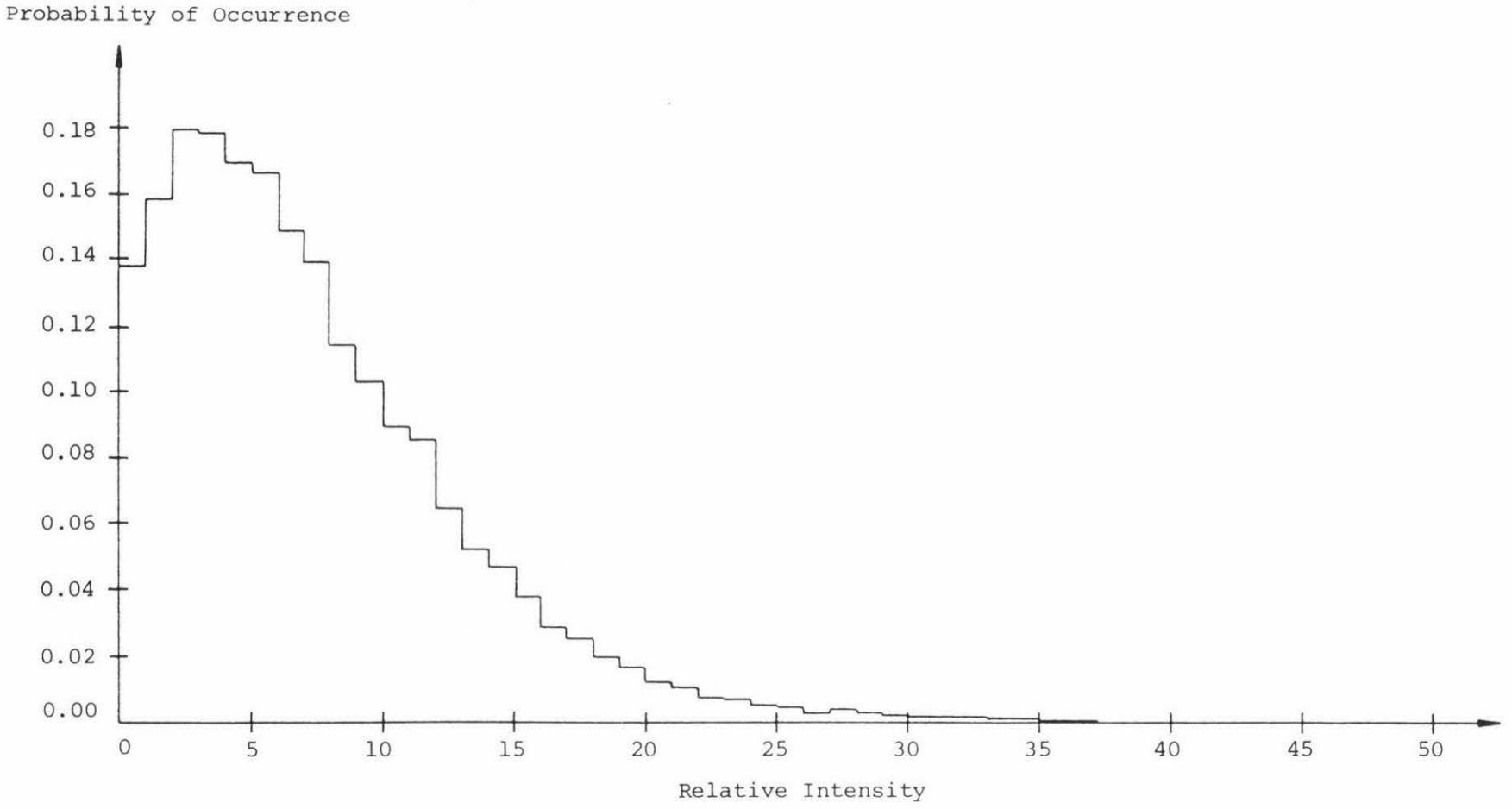

Figure C.3 Simulated probability distribution : C = 0.80

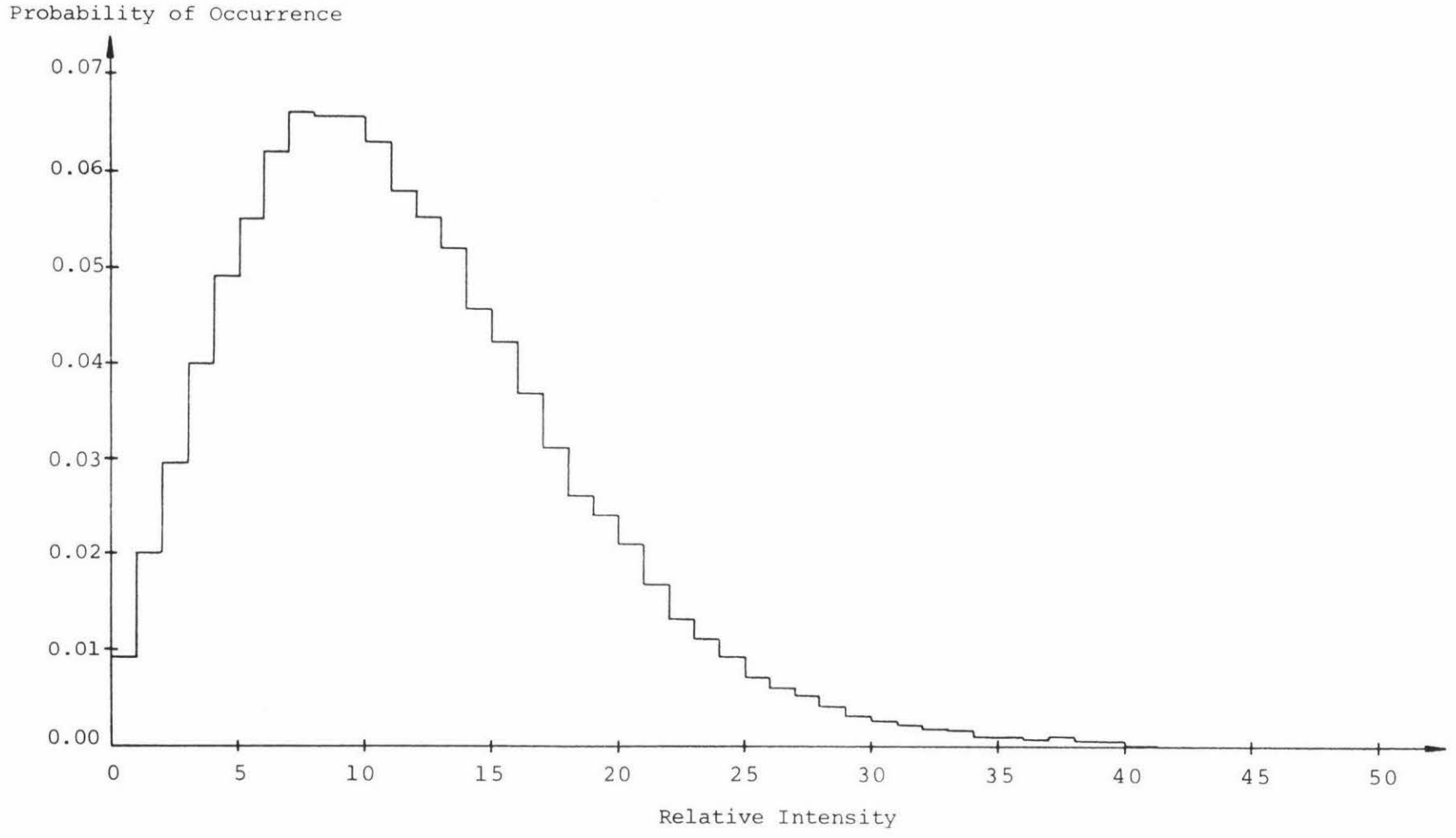

Figure C.4 Simulated probability distribution : C = 0.58

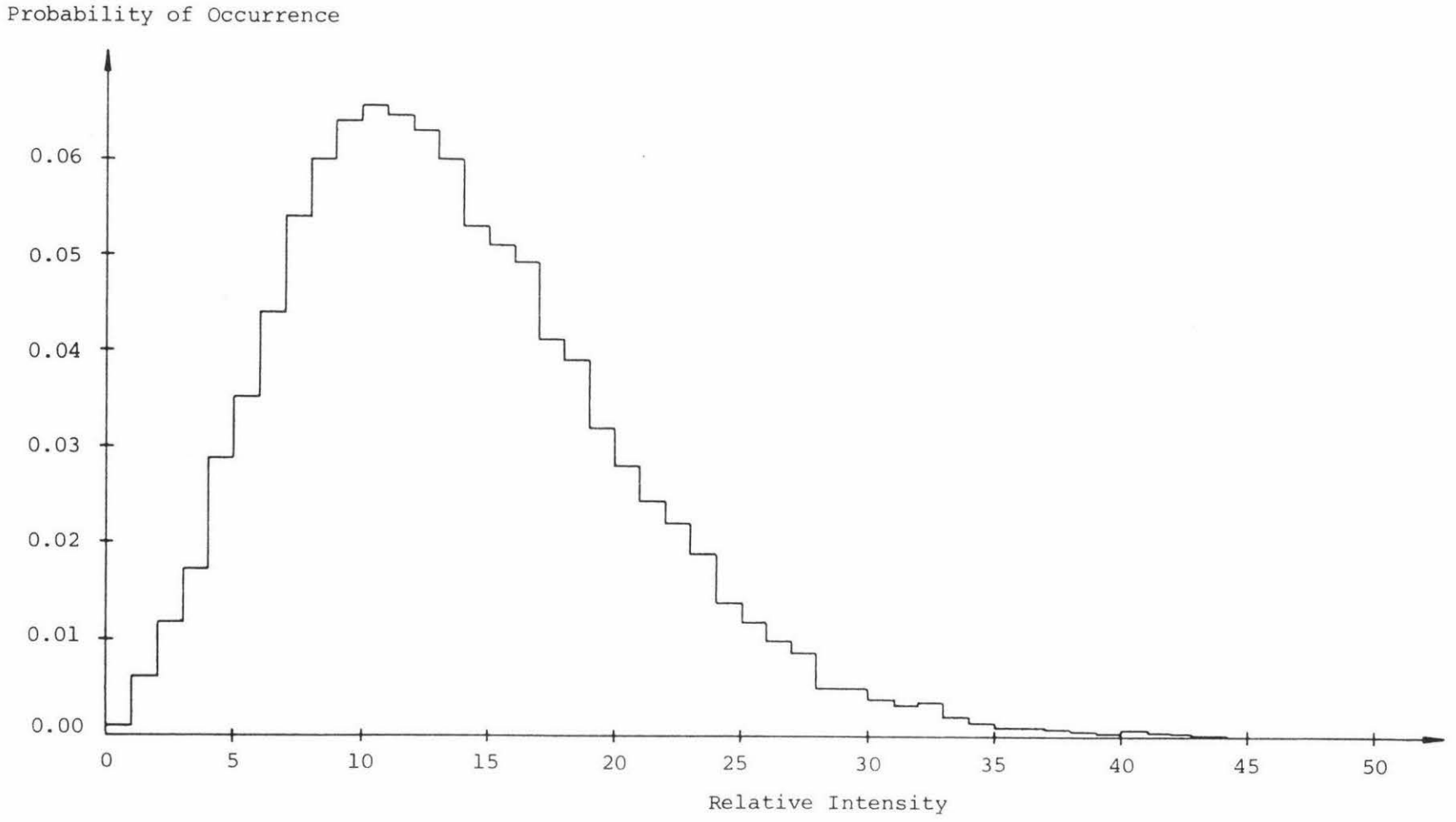

Figure C.5 Simulated probability distribution : C = 0.49

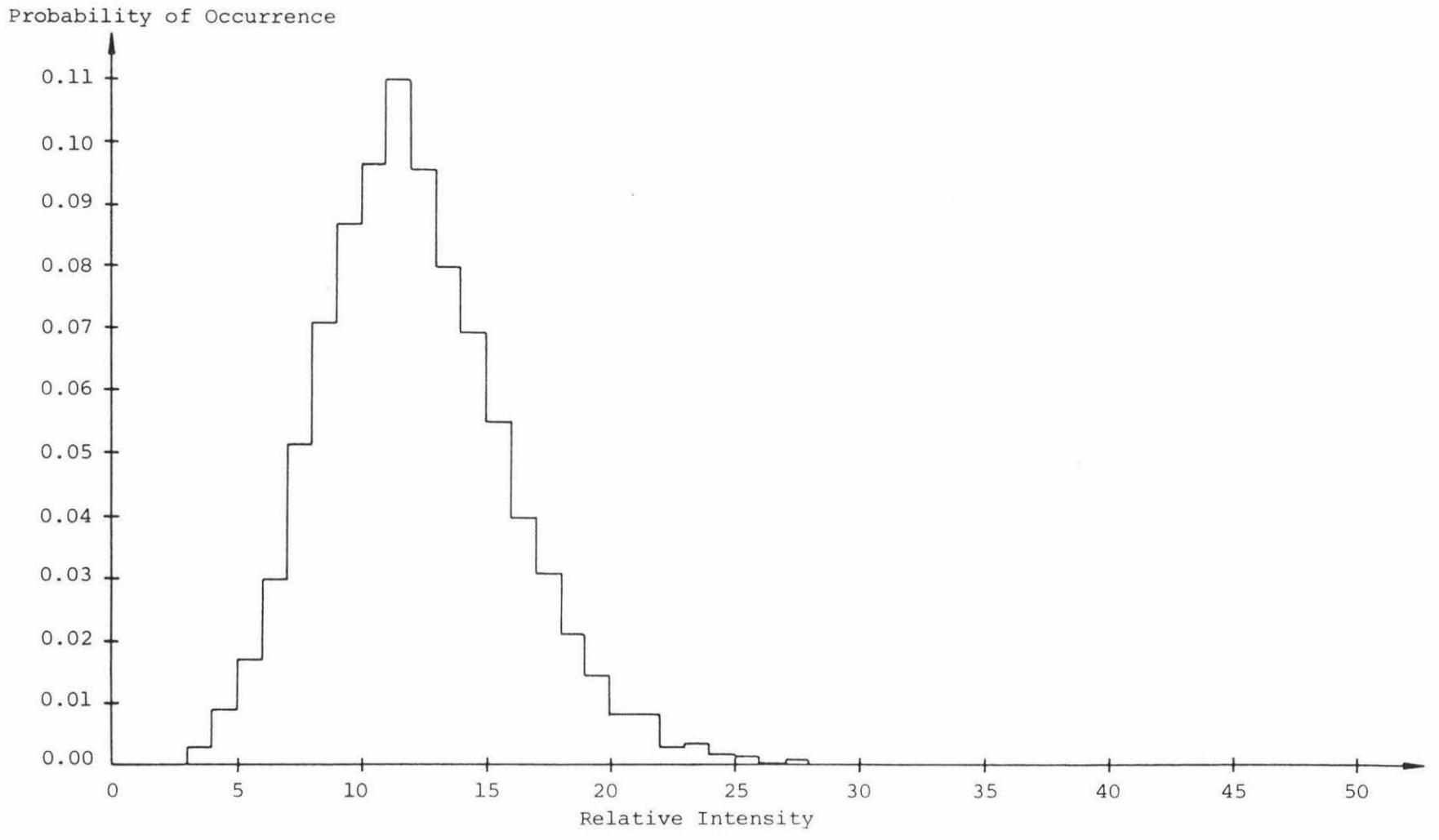

Figure C.6 Simulated probability distribution : C = 0.36

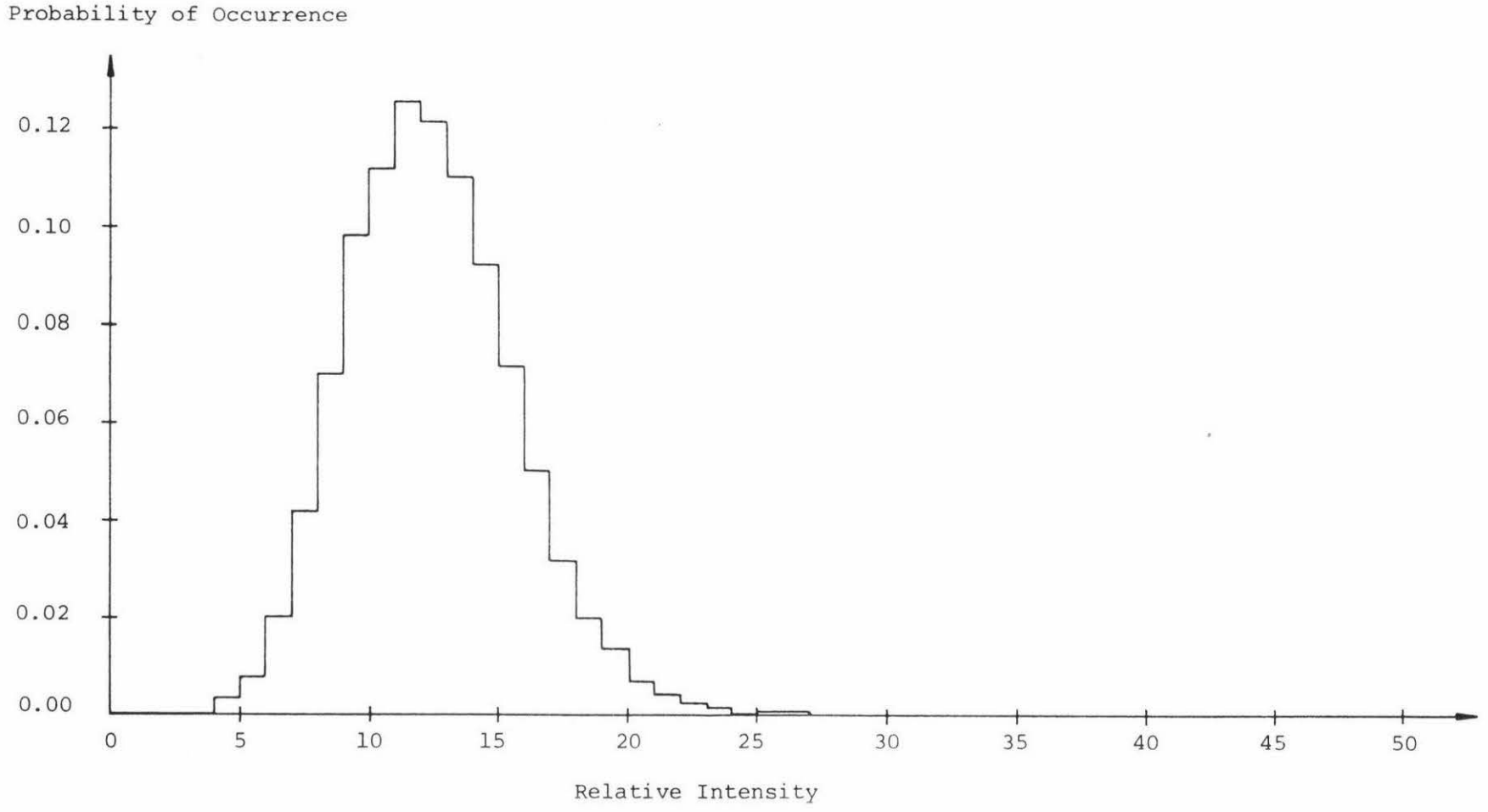

Figure C.7 Simulated probability distribution : C = 0.27

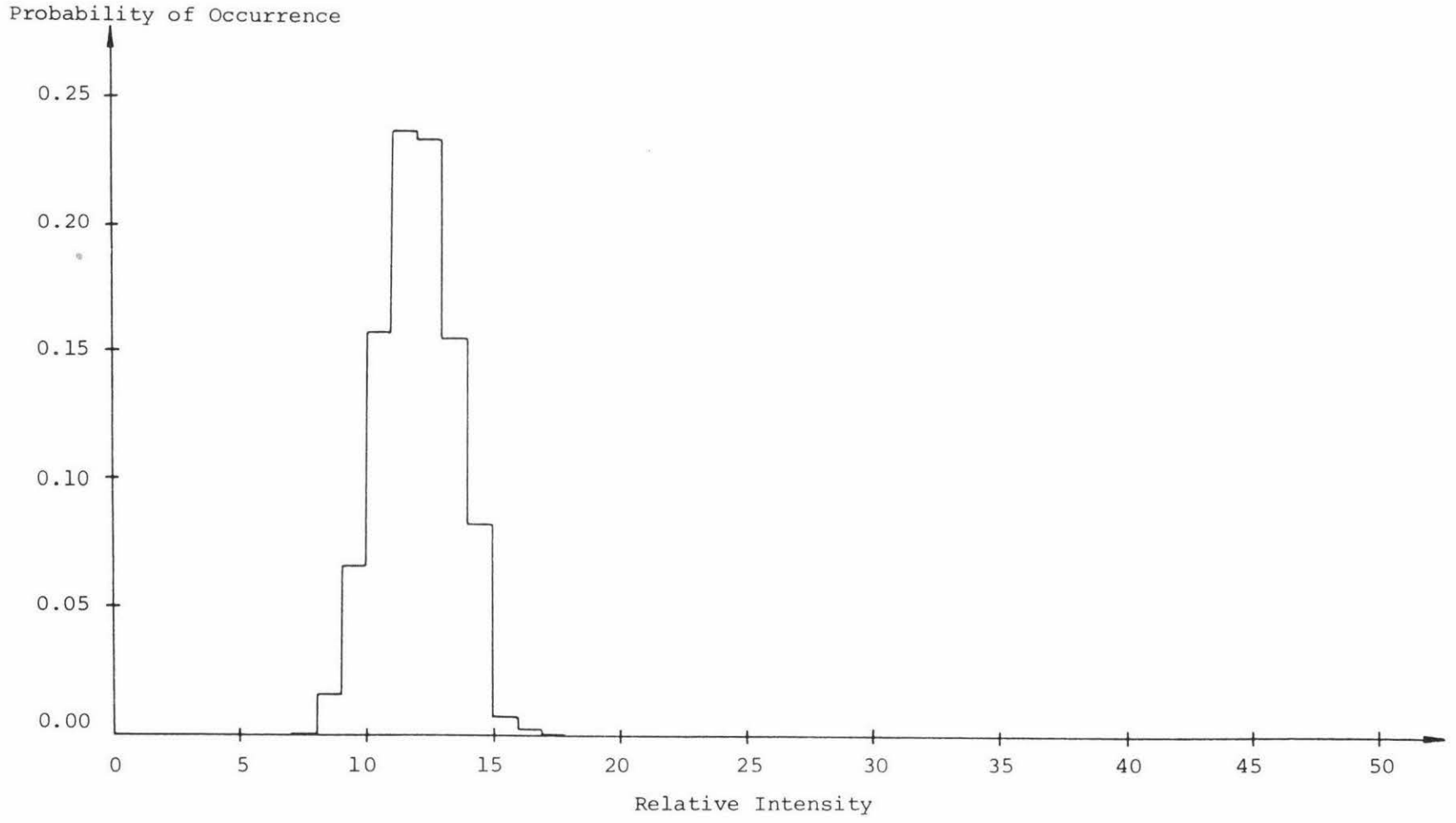

Figure C.8 Simulated probability distribution : C = 0.14

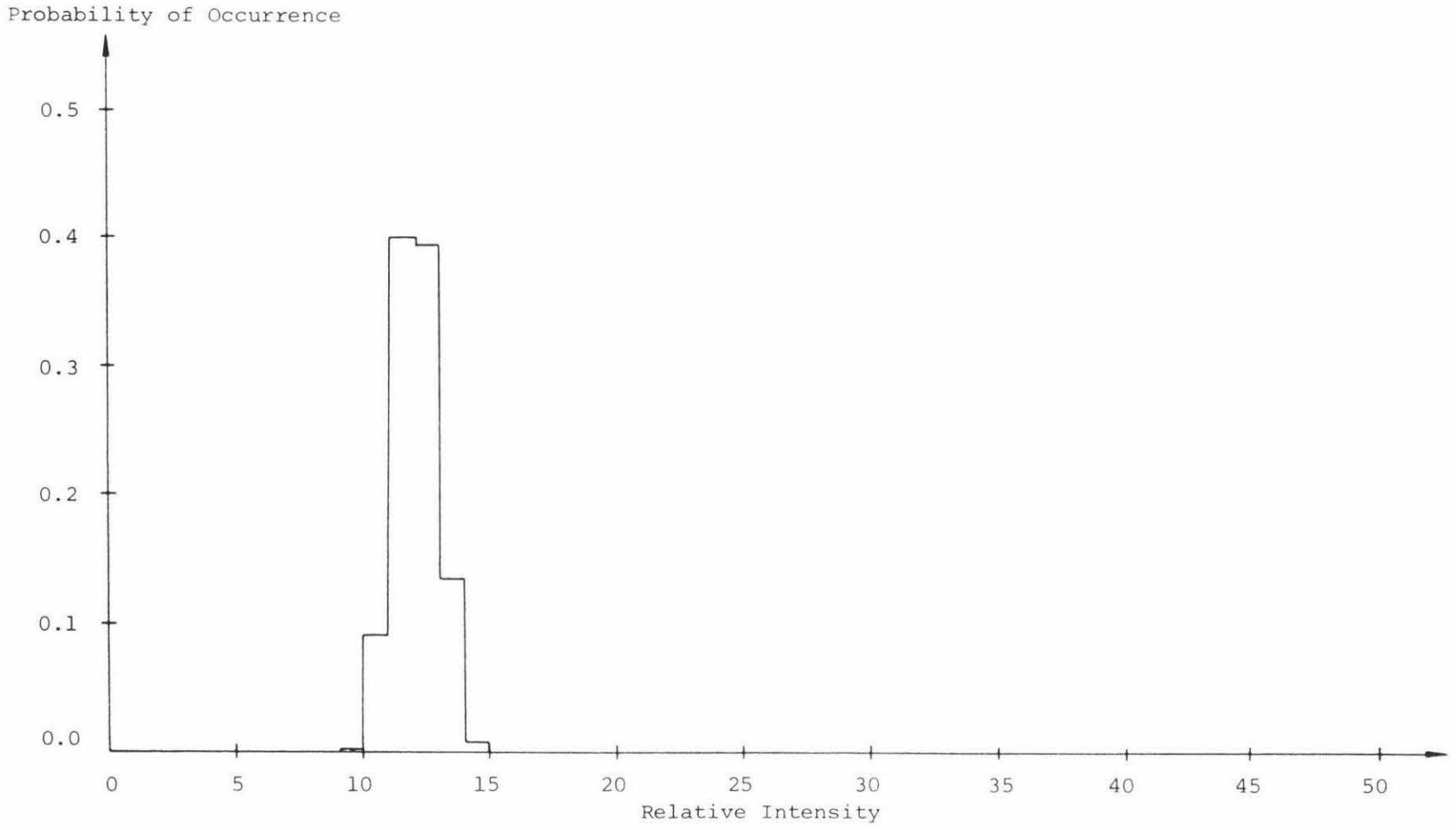

Figure C.9 Simulated probability distribution : C = 0.07

Table C.1 Probability distribution statistics

Figure	r_c	x_m	$\langle I \rangle$	σ_I	Contrast
C.3	40	10	6.74	5.43	0.80
C.4	42	9	11.03	6.43	0.58
C.5	40	8	13.12	6.45	0.49
C.6	36	5	9.78	3.51	0.36
C.7	40	4	11.87	3.18	0.27
C.8	40	2	11.58	1.59	0.14
C.9	40	1	11.53	0.83	0.07

Notes

1. x_m is the maximum value of the real or imaginary components of each phasor A_i.

2. The above results were obtained from 10000 intensity samples each made up of 20 elementary phasors.

APPENDIX D

An Experiment to Test the Effectiveness of the Probability Distribution Program

To test the effectiveness of the probability distribution program, a test waveform was fed into the computer so that the resultant output could be compared with the expected distribution.

The test waveform used was a 50 Hz sine wave with a 4V peak-to-peak amplitude and a + 1.7V offset. This gave an output from the A/D converter which ranged from 10 to 255. The probability distribution program was altered so that the sine wave was sampled automatically at ½ second intervals. Because the computer and generator output were not in step, each sample (which contained $\sim 3\frac{1}{4}$ cycles) was different. When a sufficiently accurate amplitude distribution had been built up, the program was stopped and the relevant probabilities were calculated. Figure D.1 is a typical example, produced by summimg over every five consecutive amplitude levels to reduce statistical fluctuations, and simplify plotting. The smooth curve represents the expected result which was calculated in the following fashion.

The probability density for a sine wave is just

$$p(x) = \frac{1}{\pi\sqrt{X^2-x^2}} , \qquad (D.1)$$

where X is the peak amplitude and $x \leq |X|$.

The probability that x will be between two predefined levels a and b is just

$$P(a,b) = \int_a^b p(x)\,dx = \frac{1}{\pi}\left(\arcsin\left(\frac{b}{X}\right) - \arcsin\left(\frac{a}{X}\right)\right). \qquad (D.2)$$

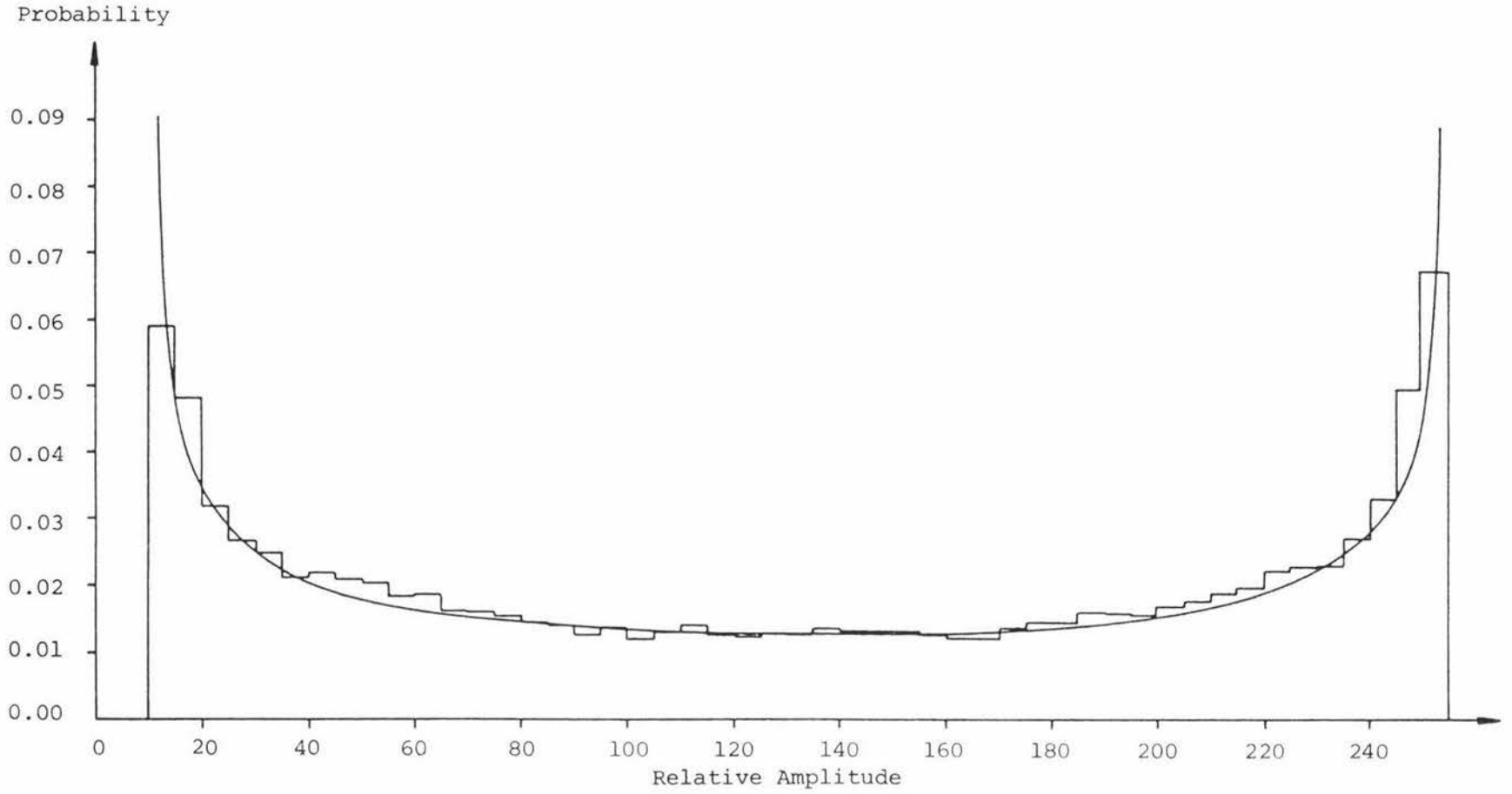

Figure D.1 Probability distribution for a sine wave input

Consideration of the amplitude distribution indicates that the peak value X is approximately 122.5 units. When this value is substituted into equation D.2 the results pictured in figure D.1 are obtained. Although these results are strictly descrete probabilities they have, for ease of comparison, been represented here by a smooth curve.

The small differences between these two results can be traced back to a distortion in the sine wave which was found to be slightly peaked at its maximum and minimum values. This effect is quite commonly observed in the output of waveform generators which create a sine wave from a triangular waveform.

APPENDIX E

Discussion on the Possible Causes of the Probability Decrease Observed in Probability Distributions as Measured by the Array

As mentioned in section 6.5 the decrease in probability which occurs for the fully developed speckle pattern (and presumably partially developed ones as well) at low intensities is most likely to have been caused by one or more of the following effects.

i) Electronic noise

ii) Light scatter

iii) Depolarization of the scattered light

iv) Charge transfer inefficiency

Electronic noise has been discussed in sections 6.3 and 6.8 where it was found that it adds an intensity of one unit to approximately 5% of all sample points. If we take figure 6.13 as being a representative curve for a fully developed speckle pattern we have from table 6.3 (run 6) and equation 6.7 that 2.4% of all samples should have zero intensities. This means that electronic noise will promote 5% of 2.4%, or 0.12% of these samples to an intensity level of one. Since this reduction in the zero level is not significant it would appear that electronic noise is not the chief culprit.

Since inserting a sheet of polaroid into the scattered beam was not found to have any significant effect on the probability distribution, depolarization of the light by the surface also seems an unlikely cause.

Charge transfer inefficiency was initially thought to be the most likely contender as its effect is to even out all intensities by a small factor. As discussed in detail by

Tanaka {ref E.1} this phenomenon is caused by an inherent inefficiency in the charge-coupled shift register which tends to leave behind a small percentage of its charge on each shift. An example of this is pictured in figure E.1 for a singly illuminated pixel. To see if this effect was significant the following experiments were performed.

Half the array was covered by a piece of black insulation tape so that a step output voltage would result when the array was illuminated. Since data is shifted out of the registers in one direction only, transfer inefficiency effects should be more noticeable with tape on one end of the array than on the other.

The results were not convincing as light scatter and diffraction swamped any noticeable differences. To reduce scatter to a minimum a converging beam of light was shone onto the array and its position was adjusted so that it covered as small an area as possible. Unfortunately it was not possible to determine the exact size of the spot other than by using the diffraction limiting formula (equation 2.72) which gave a value of 54μm when the 72mm lens was used. 5 or 6 pixels were observed to respond although this value increased dramatically for large intensities. As before there was no obvious difference between opposite sides of the intensity maximum indicating that scatter and diffraction effects were still more significant.

It would therefore appear as if light scatter is the most probable cause as it tends to uniformly increase the intensity across the array, which leads to a decrease in the probability of low intensities. Since scatter from surrounding objects was kept to a minimum it seems likely that most of the scatter occurred within the array cavity itself between the aperture window and the gold plated substrate. Apart from removing this window the only solution to this

Figure E.1 Charge transfer inefficiency within the array

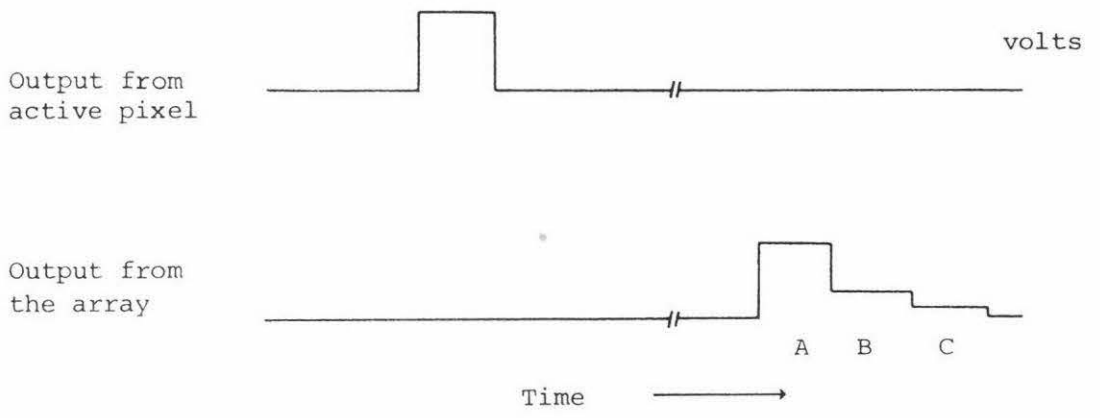

Key

A - Original pulse minus the charge left behind.

B - Charge left behind after first shift register clock cycle minus the charge left behind in the second cycle.

C - Charge left behind in the second shift register clock cycle.

problem would seem to be a compensation program which calculates the likely scatter from the mean intensity and subtracts this from all pixel outputs.

APPENDIX F

Phase Shift Calculation for Light Scattered from a Rough Surface

To calculate phase difference for the generalised situation depicted in figure 2.2 would be difficult. However, in most practical situations the distance to the light source and observation (i.e. speckle) plane is such, that rays A and B are almost parallel. (Typical areas of illumination have diameters of 2mm or less). This being the case, we can calculate the resultant phase difference ϕ quite simply with the aid of figure F.1. From simple trigonometric considerations we see that the path difference between rays A and B is just

$$\text{p.d.} = r\cos\theta + r\cos\omega, \tag{F.1}$$

so the phase difference is

$$\phi = \frac{2\pi r}{\lambda}\,(\cos\theta+\cos\omega). \tag{F.2}$$

In chapter 6, where measurements of surface roughness are made, the apparatus is arranged so that $\omega \simeq \theta$. In this situation equation F.2 simplifies to give

$$\phi = \frac{4\pi r}{\lambda}\cos\theta. \tag{F.3}$$

The introduction of a lens to image the speckle does not change the validity of these formulae as the speckle intensity in the image plane is still determined by a random sum of scattered phasors, although the area on the surface from which these are derived is now much smaller.

Figure F.1 Geometry of light scatter from a rough surface

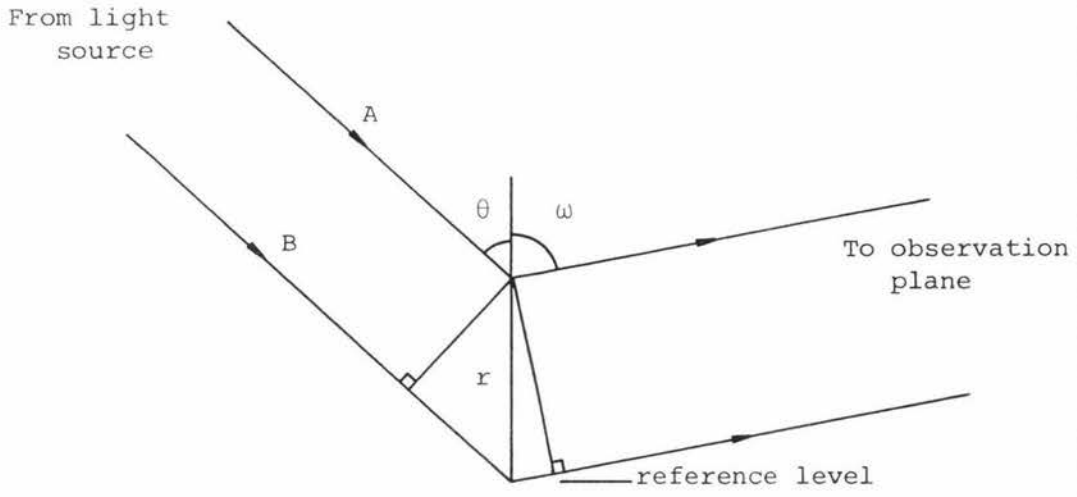

APPENDIX G

An Alternative Derivation of Equation 2.24

During the final preparation of this thesis an alternative derivation of equation 2.24 was suggested which made the calculation of $\langle x^2y^2 \rangle$ unnecessary. Rather than rewrite the relevant section, it was decided to present this alternative procedure as an appendix in the following manner:

From equation 2.11 we saw that

$$\langle I^2 \rangle = \langle (x^2+y^2)^2 \rangle = \langle x^4 \rangle + 2\langle x^2y^2 \rangle + \langle y^4 \rangle . \qquad (G.1)$$

Using a similar approach

$$\langle I \rangle^2 = \langle (x^2+y^2) \rangle^2 = (\langle x^2 \rangle + \langle y^2 \rangle)^2$$

$$= \langle x^2 \rangle^2 + 2\langle x^2 \rangle \langle y^2 \rangle + \langle y^2 \rangle^2 . \qquad (G.2)$$

Now $\langle x^2y^2 \rangle = \langle x^2 \rangle \langle y^2 \rangle$ as x and y are independent. Therefore,

$$\sigma_I = (\langle I^2 \rangle - \langle I \rangle^2)^{\frac{1}{2}}$$

$$= (\langle x^4 \rangle + \langle y^4 \rangle - \langle x^2 \rangle^2 - \langle y^2 \rangle^2)^{\frac{1}{2}} . \qquad (G.3)$$

From equations 2.17 and 2.18 we obtained

$$\langle x^4 \rangle = 3\sigma_x^4 + 6\langle x \rangle^2 \sigma_x^2 + \langle x \rangle^4 , \qquad (G.4)$$

and

$$\langle y^4 \rangle = 3\sigma_y^4 . \qquad (G.5)$$

Equation 2.8 may be manipulated to give

$$\langle x^2 \rangle^2 = (\sigma_x^2 + \langle x \rangle^2)^2$$

$$= \sigma_x^4 + 2\langle x \rangle^2 \sigma_x^2 + \langle x \rangle^4 , \qquad (G.6)$$

and

$$\langle y^2 \rangle^2 = (\sigma_y^2)^2 = \sigma_y^4, \tag{G.7}$$

where $\langle y \rangle = 0$ as previously assumed.

Substituting these results into equation G.3 gives

$$\sigma_I = (2\sigma_x^4 + 2\sigma_y^4 + 4\langle x \rangle^2 \sigma_x^2)^{\frac{1}{2}}. \tag{G.8}$$

With equations 2.5 and 2.9 we can then obtain the result

$$C = \frac{\sigma_I}{\langle I \rangle} = \frac{(2(\sigma_x^4 + \sigma_y^4) + 4\langle x \rangle^2 \sigma_x^2)^{\frac{1}{2}}}{\sigma_x^2 + \sigma_y^2 + \langle x \rangle^2}, \tag{G.9}$$

which is just equation 2.24.

APPENDIX H

Computer Listing of Speckle Simulation Program

```
 10 Rem Speckle simulation program, written in BASIC for
    Commodore Pet.
 20 Rem Read graphics data.
 30 For I=0 to 7:Read A$(I):Next
 40 Rem Dimension frequency array.
 50 Dim f(255)
 60 Input"{Clear} Number of samples per speckle =";G
 70 Input"{1 down} Number of speckles =";U
 80 V=1/G:XM=20
 90 Print"{Clear}"
100 Rem Generate U random intensities.
110 For K=1 to U
120 Rem Generate random seed.
130 Z=Rnd(-Ti)
140 X=0:Y=0
150 Rem Generate random intensity components.
160 For I=1 to G
170 X=X+(Rnd(1)-0.5)*XM
180 Y=Y+(Rnd(1)-0.5)*XM
190 Next I
200 Rem Determine intensity.
210 M=Int((X*X+Y*Y)*V*0.15)
220 If M>255 then 140
230 Rem Increment relevant element in frequency array.
240 f(M)=f(M)+1
250 Next K
260 Rem Display frequencies on screen.
270 For P=0 to 255
280 Print P;f(P),:P=P+1:Print P;f(P)
290 Next P
300 Sum=0:N=0:SD=0
310 Rem Calculate ΣIf(I) & Σf(I)
320 For I=0 to 255
330 Sum=Sum+I*f(I)
340 N=N+f(I)
350 Next I
```

```
360 Rem Calculate mean intensity.
370 Mean=Sum/N
380 Rem Calculate Σ(I-<I>)^2 f(I)
390 For I=0 to 255
400 Q=Q+f(I)*(I-Mean)↑2
410 Next I
420 Rem Calculate standard deviation of intensity.
430 SD=Sqr(Q/(N-1))
440 Print"{1 down}{Reverse} Press key for statistics"
450 Get A$:If A$="" then 450
460 Print"{Clear}{8 down}"
470 Print"Mean =";Mean
480 Print"{1 down} Standard deviation =";SD
490 Print"{1 down} Contrast=";SD/Mean
500 Print"{1 down}{Reverse} Press key for intensity distribution"
510 Get A$:If A$="" then 510
520 Print"{Clear}"
530 Rem Draw graph axes.
540 For I=1 to 24
550 Print"▌ "
560 Next I
570 Print "└";
580 For I=0 to 37
590 Print"─";
600 Next I
610 Rem Determine maximum frequency.
620 For I=0 to 39
630 If f(I)>S then S=f(I)
640 Next I
650 Rem Reposition cursor
660 For I=0 to 38
670 Print"{2 left}";
680 Next I
690 Print"{1 left}{1 down}";
700 Rem Draw bar graph.
710 For I=0 to 38
720 Rem Scale frequency distribution to monitor.
730 T=Int(f(I)*24/S)
```

```
740 If T=0 then 780
750 For J=0 to T-1
760 Print"{Reverse} {Reverse off}{1 left}{1 up}";
770 Next J
780 J=f(I)*24/S-Int(f(I)*24/S)
790 J=Int(J*8)
800 Print A$(J);:If T=0 then 840
810 For J=0 to T-1
820 Print"{1 down}";
830 Next J
840 Next I
850 Go to 850
860 Data" ","▁","▂","▃","▄","{Reverse}▀{Reverse off}","{Reverse}▔
    {Reverse off}","{Reverse}¯{Reverse off}"
870 End
```

Note. Statements within curly brackets are special cursor control characters.

For large values of U, this program will produce an intensity distribution like that in figure C.1 With the addition of the following statement:

```
195 X=X+RC
```

and the appropriate values of RC and XM, (see page 167) the distributions in figures C.3 to C.9 may be reproduced.

REFERENCES

Chapter 2

2.1 BECKMANN, P. and A. Spizzichino
The scattering of electromagnetic waves from rough surfaces. (International series of monographs on electromagnetic waves, Vol.4). Oxford, London, New York, Paris, Pergamon Press, 1963. 505p.

2.2 GOODMAN, J.W.
Statistical properties of laser speckle patterns. p 9-74 in Laser speckle and related phenomenon. (Topics in applied physics, Vol.9).Ed. J.C.Dainty, Berlin, Heidelberg, New York, Springer - Verlag, 1975.

2.3 GRADSHTEYN, I.S. and I.M.Ryzhik
Table of integrals, series, and products. 4th ed. New York and London, Academic Press, 1965.

2.4 ASAKURA, T.
Surface roughness measurement p11-49. In Speckle metrology. Ed. R.K.Erf, New York, San Francisco, London, Academic Press, 1978.

Chapter 3

3.1 HASS, E.S.
Polarization and lasers. Laser technical bulletin number 7. Spectra physics, 1975. 9p.

Chapter 4

4.1 STEPHENS, O.B. et.al.
An implementation of a charge-coupled photodiode linear image dissector in tissue microscopy application. p46-61. In Nelcon 80 Electronics for the eighties; proceedings of the 17th N.Z. national

electronics conference. Massey University, August 1980.

4.2 BARBE,D.F.
Imaging devices using the charge-coupled concept. Proceedings of the IEEE, Vol.63. No.1, January 1975, p 38-74.

4.3 RETICON
Charge-coupled photodiode arrays CCPD-256, CCPD-1024, CCPD-1728
Publication number 77098, Reticon Corporation, Sunnyvale, California. 1977. 6p.

4.4 RETICON
RC700A/RC702A CCPD Interface system operating instructions
Drawing number, 045-0042, 010-0275, 010-0274, Reticon Corporation, Sunnyvale, California. 1979. 20p.

Chapter 6

6.1 REASON,R.E.
The measurement of surface texture, p585-634. In Modern workshop technology Vol.2. Ed. H.W.Wright Baker. 3rd ed. London and Basingstoke, Macmillan & Co Ltd, 1970.

6.2 NAKAGAWA, K.and T.Asakura
Average contrast of white-light image speckle patterns. Optica Acta, Vol.26, No.8,1979, p 951-960.

Chapter 7

7.1 BRIERS, J.D. and I.G.Angus
Speckle photography applied to the measurement of displacements and rotations. Report No. 634, PEL, DSIR, N.Z., March 1979. 25p.

7.2 FRANCON,M.
Laser speckle and applications in optics. New York, San Francisco, London, Academic Press, 1979.

7.3 COSTA, G.A. et al.
Thermal expansion measurements by speckle interferometry. Applied Optics, Vol.19, No.7, April 1980. p 1032-1033.

7.4 YAMAGUCHI,I.
A laser-speckle strain gauge. J.Physic. E:Scientific Instruments Vol.14, 1981. p 1270-1273.

Appendix E

E.1 TANAKA, S.C.
Coping with charge transfer inefficiency affecting modulation transfer function (MTF) of charge-coupled devices (CCD). Optical Engineering, Vol.18, No.5, September-October 1979. p504-512.